Cosmological Applications of
STRONG GRAVITATIONAL LENSING

Scale and content of the Universe as inferred from multiply imaged quasars.

DANUTA PARAFICZ

Dissertation
Submitted for the Degree

PHILOSOPHIÆ DOCTOR

Dark Cosmology Centre
Niels Bohr Institutet
Det Naturvidenskabelige Fakultet
Københavns Universitet

Submission: *November 9th, 2009*
Defense: *January, 2010*

Supervisor: *Prof. Jens Hjorth*
Opponents: *Prof. Liliya Williams*
Prof. Chris Fassnacht

ACKNOWLEDGMENT

So sweet a thing it is not to be wise
that on the contrary men rather pray
against anything than that

Erasmus Rotherdamus

This Thesis would not have been completed without the help of a number of people. Most importantly I would like to thank to my supervisor. I thank him for the enormous scientific contribution to all of the publications and also for mental support and extraordinary faith in me. I thank also my two office-mates Daniele Malesani and Bo Milvang-Jensen for answering my constant questions, for helping me to get through difficult times and for contributing scientifically to all the research I have done. I thank also all the DARKers and NOT people for providing a stimulating, challenging, inspiring and friendly environment. I have a special appreciation for Árdís Elíasdóttir mostly for scientific and mental help and also for spending quality time with me and for introducing Mexi Bar to my PhD life. I thank my boyfriend for having interest in my research and simply for being there for me.

On a more personal note, I would like to dedicate this Thesis and express my appreciation to my boyfriend Nikolaos Apostolakos whose commitment, love and persistent confidence in me, has made this Thesis possible. Niemniejszym chciałabym również podziękować mojej mamie, która wykazała ogrom zainteresowania i cierpliwości, gdy ja pisałam pracę. Bez jej wsparcia, zrozumienia i inspiracji stworzenie tej pracy doktoranckiej było by niemożliwe.

Kto się waha z obawy, że mysl co w nim drzemie
Straci na swej piękności zstąpiwszy na ziemię
Przejść przez wszystkich walk ludzkich i zawodów stopnie
Ten zwiędnie w pożądaniach i niczego nie dopnie.

Adam Asnyk

CONTENTS

Acknowledgment **iii**

Contents **v**

Abstract **9**

1 A brief history of gravitational lenses **11**
1.1 Gravitational Lensing beginnings . . . 12
1.1.1 Philosophiae Naturalis Principia Mathematica . . . 12
1.1.2 Einstein's Theory and the Eclipse . . . 14
1.2 Origins of Strong Lensing . . . 16

2 Theoretical Introduction **18**
2.1 Gravitational Lensing . . . 19
2.1.1 Gravitational Lensing in General Relativity . . . 19
2.1.2 Basic lensing equations . . . 21
2.1.3 Lens potential . . . 23
2.1.4 Gravitational Lens Time Delay . . . 23
2.2 Cosmology . . . 24
2.2.1 Theory . . . 24
2.2.2 Observational cosmology . . . 26
2.3 Elliptical galaxies . . . 31
2.3.1 Elliptical galaxies basics . . . 31
2.3.2 X-rays mass estimation . . . 31
2.3.3 Properties of elliptical galaxies . . . 31

3 Lens modeling **37**
3.1 Parametric modeling . . . 38
3.1.1 Singular isothermal sphere (SIS) . . . 38
3.1.2 Singular isothermal ellipsoid (SIE) . . . 38
3.1.3 Parametric modeling implementation . . . 39
3.2 Degeneracies . . . 41
3.3 Non-parametric modeling . . . 44
3.3.1 Non-parametric modeling theory . . . 44
3.3.2 Non-parametric modeling implementation . . . 44

4 Observations & Image Deconvolution **48**
4.1 Observations . . . 49
4.1.1 NOT . . . 49
4.1.2 Monitoring . . . 50
4.2 Deconvolution . . . 52
4.2.1 Theoretical description . . . 52
4.2.2 Application . . . 54

5 Results of optical monitoring of 5 SDSS double QSOs with the Nordic Optical Telescope **56**
5.1 Introduction . . . 57
5.2 Observation . . . 58
5.3 Targets . . . 59
5.3.1 SDSS J0903+5028 . . . 59
5.3.2 SDSS J1001+5027 & SDSS J1206+4332 . . . 64
5.3.3 SDSS J1335+0118 . . . 64
5.3.4 SDSS J1353+1138 . . . 67
5.4 Photomery and image deconvolution . . . 67
5.4.1 Image deconvolution . . . 67
5.4.2 Photometry . . . 67
5.5 Light curves . . . 69
5.5.1 QSOs with little variability . . . 69
5.5.2 Quasars with variability . . . 73
5.6 Time delay of SDSS J1206+4332 . . . 76
5.7 Microlensing . . . 79
5.8 Modeling . . . 85
5.8.1 Analytical modeling . . . 85
5.8.2 Non-parametric modeling . . . 93
5.9 Simultanous modeling . . . 95
5.10 Discussion . . . 97

6 The Hubble Constant inferred from 18 time delay lenses **100**
6.1 Introduction . . . 101
6.2 Pixelated modeling . . . 102
6.3 Data set . . . 103
6.4 Full set results . . . 103
6.5 'Elliptical' sample . . . 110
6.6 Conclusions . . . 112

7 Gravitational lenses as cosmic rulers: $\Omega_{\rm m}$, Ω_Λ from time delays and velocity dispersions **114**
7.1 Introduction . . . 115
7.2 Lenses as standard rulers . . . 115
7.3 Monte Carlo Markov Chain simulations . . . 118
7.3.1 Comparison of methods . . . 120
7.3.2 One high-redshift lens . . . 120
7.3.3 Many lenses . . . 122
7.4 Discussion . . . 122

8 Conclusions and Outlook **124**
8.1 Conclusions . . . 124
8.1.1 Time delays . . . 124
8.1.2 Statistics . . . 125
8.1.3 Theory . . . 125
8.2 Future . . . 125

A Resolving the discrepancy between lensing and X-ray mass estimates of the complex galaxy cluster Abell 1689 **130**
A.1 Introduction . . . 131
A.2 X-rays . . . 132
A.2.1 X-ray observations . . . 132
A.2.2 X-ray analysis: Image and surface brightness . . . 132
A.2.3 X-ray analysis: Background . . . 135
A.2.4 X-ray analysis and results: Hardness ratio . . . 135
A.2.5 X-ray analysis and results: Temperature profile . . . 137
A.2.6 X-ray analysis and results: Mass profile . . . 139
A.2.7 X-ray analysis and results: NFW fit and projection . . . 141
A.2.8 X-ray analysis and results: The NE region . . . 141
A.2.9 Discussion of X-ray results . . . 142
A.3 Additional observations of Abell 1689 . . . 144
A.3.1 Strong and weak lensing analyses . . . 144
A.3.2 Lensing analysis: mass profiles . . . 148
A.3.3 Lensing results and discussion . . . 148
A.3.4 Redshift distribution of cluster galaxies . . . 152
A.4 Discussion . . . 152
A.5 Conclusions . . . 153

APPENDIX 129

Bibliography **156**

List of Figures **169**

List of Tables **171**

Acronyms **173**

ABSTRACT

One of the most intriguing recent results in physics is the growing evidence that an unknown energy field and an unknown kind of matter are the major components of the Universe (70% and 30%, respectively; see e.g. Riess et al. 1998, Spergel et al. 2007). Understanding and estimating the precise value of the energy density of the two above components, together with measuring the Hubble constant that determines the age of the Universe, is a major goal of modern astrophysics.

An interesting method for estimating these parameters is strong gravitational lensing of quasars (QSOs). As shown by Refsdal (1964), H_0, Ω_m and Ω_Λ can be measured based on the time delay (Δt) between multiply lensed images of QSOs, because Δt depends on H_0 and on the distances to lens and source, hence Ω_m and Ω_Λ. Determination of cosmological parameters using gravitational lensing suffers from some degeneracies, but it is based on well understood physics and unlike distance ladder methods there are no calibration issues. Moreover, it has an advantage over some of the leading methods (such as Type Ia SNe) in that it is a purely cosmological approach.

In this thesis, the property of strong gravitational lensing – time delay – is extensively explored. Strong gravitational lensing, and in particular time delays, are investigated here both theoretically and observationally. The focus is on the time delay as a cosmological and astrophysical tool to constrain H_0, Ω_m, Ω_Λ, and to measure the masses of lensing galaxies.

The first Chapter presents a historical background of gravitational lensing. It explains the process involved in creating the theory of gravitational lenses. It shows how Newton and then Einstein developed the concept and how Refsdal and others made it a cosmological tool. We present in more detail how gravitational lensing influenced the history of physics by being the first proof of Einstein's theory of gravity. The Chapter ends by discussing the first observational discovery of a strong gravitational lens.

The second Chapter is a theoretical introduction to the thesis divided in three Sections: gravitational lensing, cosmology and elliptical galaxies. In the first Section it is briefly presented how gravitational light deflection can be derived from General Relativity. We discuss the lens potential and introduce the the basic lensing equations necessary to understand the rest of the thesis. We also introduce the time delay effect, showing its origin and briefly describing its possible applications. In the second Section we present some basic concepts and discoveries in Cosmology, showing how gravitational lensing stands in this respect. The third Section is dedicated to a specific kind of lensing galaxies. Eighty percent of gravitational lenses are elliptical galaxies, hence this Section is a theoretical introduction to those galaxies and to their stellar dynamics.

The third Chapter is about lens modeling. All the parameters in the time-delay calculations can be measured directly or indirectly from observations, except for the mass surface density distribution of the lens. Therefore, some assumptions need to be introduced to model this parameter. Lens modeling is the most challenging part of the gravitational lensing analysis. In

this Chapter we present the two standard ways of handling lens models, parametric and non-parametric.

In the fourth Chapter we describe observations and image deconvolution. The Chapter consists of 2 Sections. In the first one we try to describe all the nuances and logistic problems arising in long-term, frequent-sampling, optical monitoring. In the second one we focus on image deconvolution of the obtained observations. Gravitationally lensed quasars are mostly systems with image separation smaller than the resolution of most present-day telescopes. Hence, in order to separate quasar images, mathematical methods are needed.

In the fifth Chapter we present optical R-band light curves of five SDSS doubly-lensed QSOs (SDSS J0903+5028, SDSS J1001+5027, SDSS J1206+4332, SDSS J1353+1138, SDSS J1335+0118) obtained from monitoring at the Nordic Optical Telescope (NOT) between 2005 September and 2077 September. We also present analytical and pixelated modeling of the observed systems. For SDSS J1206+4332, we measured the time delay to be $\Delta\tau = 116^{+4}_{-5}$ days, which, for a singular isothermal ellipsoid model, corresponds to a Hubble constant of 73^{+3}_{-4} km s^{-1} Mpc^{-1}. Simultaneous pixelated modeling of five other systems, for which a time delay has been previously measured at the NOT leads to $H_0 = 61.5^{+8}_{-4}$ km s^{-1} Mpc^{-1}. Finally, by comparing the light curves of the two images of each system, suitably shifted by the predicted or observed time delays, we found no evidence of microlensing variability over the course of the monitoring period.

In the sixth Chapter we present the simultaneous analysis of 18 galaxy lenses with time delay measurements. For each lens we derive mass maps using pixelated simultaneous modeling with shared Hubble constant. We estimate the Hubble constant to be $65.7^{+6.2}_{-3.7}$ km s^{-1}Mpc^{-1} (for a flat Universe with $\Omega_m = 0.3$, $\Omega_\Lambda = 0.7$). We have also selected a subsample of five relatively isolated early type galaxies, and by simultaneous modeling with an additional constraint on isothermality of their mass profiles we get $H_0 = 75.8^{+3.4}_{-3.3}$ km s^{-1}Mpc^{-1}.

In the seventh Chapter we show that a cosmic standard ruler can be constructed from the joint measurement of the time delay, $\Delta\tau$, between gravitationally lensed quasar images and the velocity dispersion, σ, of the lensing galaxy. Specifically, for a singular isothermal sphere lens, $D_{OL} \propto \Delta\tau/\sigma^2$, where D_{OL} is the angular diameter distance to the lens. Using MCMC simulations we illustrate the constraints set in the Ω_m–Ω_Λ plane from future observations.

The eight Chapter contains a summary of the achievements, and a discussion about the meaning of the obtained results and future studies.

1

A BRIEF HISTORY OF GRAVITATIONAL LENSES

ABSTRACT –

This Chapter presents a historical background of gravitational lensing. It explains the process involved in creating the theory of gravitational lenses. It shows how Newton and then Einstein developed the concept and how Refsdal and others made it a cosmological tool. We present in more detail how gravitational lensing influenced the history of physics by being the first proof of Einstein's theory of gravity. The Chapter ends by discussing the first observational discovery of a strong gravitational lens.

1.1 GRAVITATIONAL LENSING BEGINNINGS

1.1.1 PHILOSOPHIAE NATURALIS PRINCIPIA MATHEMATICA

The history of gravitational lensing starts with the *Philosophiae Naturalis Principia Mathematica* of Sir Isaac Newton. The *Principia*, a foundation of modern science, were published in 1687 and they are a very first theory of gravity were mathematics is used to explain all kinds of motion in the Universe, from apples falling from trees to planets orbiting around the Sun. Newton, undoubtedly a revolutionist in science, as a first discovered the power of abstract mathematics to explain the physical systems that we see in experiments and observations. He understood that by testing mathematical constructions, based on observed systems, one can draw conclusions about the physical world. This simple but great concept had been never applied before.

Newton described in the *Principia* the famous three laws of motion, the law of gravitation, various ideas on hydrostatics, sound waves, and, what is most important for this Thesis, gravitational lensing.

Newton's idea was that if light consists of particles that possess mass, then it should be attracted by gravitational force. According to that, when a light ray is passing at a distance b from an object with a mass M then its path is bended by the gravitation (see Fig. 1.1). The bending angle α can be easily derived from Newton's law of gravitation, and is given by the formula

$$\alpha = \frac{2MG}{bc^2}. \tag{1.1}$$

For over 200 years, scientists saw physics through Newton's eyes. His ideas dominated science, until Albert Einstein challenged them.

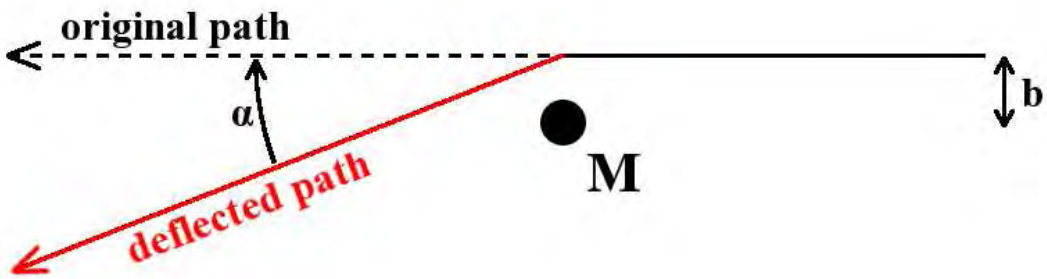

Figure 1.1: *Light deflection diagram*

1.1.2 EINSTEIN'S THEORY AND THE ECLIPSE

In 1916, Einstein changed the view of physics by publishing the theory of General Relativity (GR). GR describes a completely new Universe where gravity is changing the shape of the space-time. This theory brought new light also on gravitational lensing, since the bending of light paths in a gravitational potential became not just a possibility but a requirement in the theory. In the GR point of view, light does not have to possess mass for the gravity to act on it, but simply moves on geodesic lines, which are curved in the gravitational field. Despite that newtonian and relativistic concepts of gravitational lensing are very different, the bending angle of the light in GR is only factor of two bigger than in Newton's theory.

Sir Arthur Stanley Eddington, a British astrophysicist, realized that Einstein's theory could be tested by observing the gravitational lensing effect next to the Sun. One needs to measure whether the bending angle of the light due to gravitational lensing is as predicted by Newton or twice bigger, as predicted by Einstein.

When the Sun is passing in the field of view of stars, their apparent positions should be slightly changed due to gravitational potential of the Sun, but we can not see that, simply because the Sun is too bright, the only possibility to observe this effect is during a Sun eclipse. Sun eclipses allow us to see stars in the sky, even those close to eclipsed Sun. So, to check whether Einstein was right, one has to measure the positions of stars close to Sun, and compare those to where they are seen in the night sky at another time of the year when the Sun is far away from them.

The next upcoming Sun eclipse was predicted to be in 1919 and nicely enough the Sun during that eclipse was in front of a group of very bright stars, the Hyades. The major problem was that the observation needed to be extremely accurate. The deflection angle predicted by Einstein was small, $1\farcs75$.

The 1919 eclipse was visible from northern Brazil, across the Atlantic Ocean to West Africa. Two expeditions were organized by Eddington, to prevent unexpected circumstances and assure that the experiment will be performed. One was led by Eddington to the island of Principe, and the other led by Andrew Crommelin from the Royal Observatory at Greenwich to Sobral, in Brazil. Both expeditions encountered problems. On the day of the eclipse, 29 May 1919, Eddington had bad weather but he managed to take some data, while Crommelin on the other hand had good weather but made focusing errors of his main telescope.

After the eclipse, Eddington measured the positions of the stars that were near the eclipsed Sun (see Fig. 1.2), and compared them with reference positions taken previously when the Hyades were visible in the night sky. The measurements had to be incredibly accurate, not only because the expected deflections were small but also because the images of the stars were blurred, due to problems with the telescopes and disturbance from the solar corona.

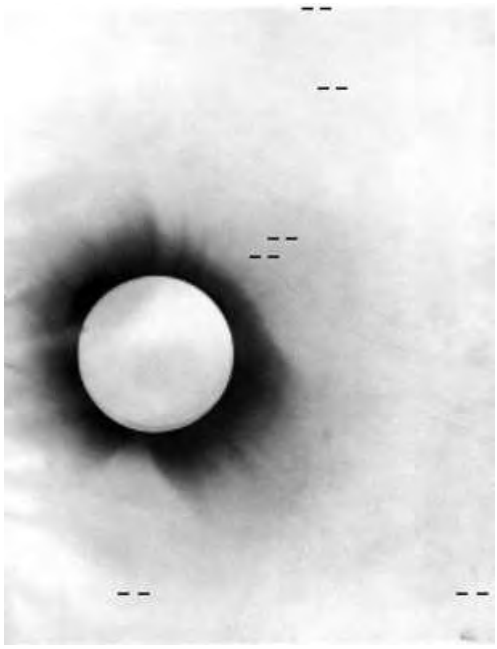

Figure 1.2: *Principe Island, 29 May 1919. Marked on a negative photo of the 1919 solar eclipse are the positions of stars examined in the historic test of Einstein's theory of gravity.*

Many contemporaneous physicists were skeptical about that measurements. According to them, because of all the problems encountered during observations, the measurements were not accurate enough and the measurement errors were big enough to allow for the twice smaller newtonian result. Despite that, Eddington announced that the measurements agreed with the predictions of Einstein's new theory and did not support Newton's one. Einstein became famous. However, a convincing proof of his theory came much later, after half century, when the theory was already well known and developed.

The precision tests of various predictions of general relativity started in 1959, remarkably succeeding in 1974 by Hulse & Taylor (1974). Hulse & Taylor (1974) using the behaviour of binary pulsars tested predictions of general relativity and showed that GR is with a great agreement with the observations.

1.2 ORIGINS OF STRONG LENSING

Currently gravitational lensing is divided into three major research subclasses, which differ between them just with the scale. There are micro, strong and weak lensing. We call microlensing the type of lensing where the lens is a compact object, a star or a planet; strong and weak lensing, on the other hand, are kinds of lensing where the lens is a galaxy or a cluster of galaxies. In the regime of strong lensing, the lensed object is seen as multiple image, while in weak lensing the source objects are just magnified or demagnified. This Thesis is mostly dedicated to strong lensing.

The concept of strong lensing comes from Zwicky (1937). He first pointed out that galaxies are massive enough to bend the light from background sources so strong that they can be seen as multiple images. The most acknowledged pioneer of strong lensing was Sjur Refsdal, a Norwegian scientist, who published a remarkable series of theoretical papers discussing all kinds of aspects of strong gravitational lensing. Refsdal (1964) as first pointed out that multiple images of strongly lensed quasars can measure precisely the mass of the inner regions of galaxy and they can be used to constrain the Hubble constant.

He was one of the first to describe and explore the phenomenon of the so-called time delay, which this Thesis is focused on. This effect is based on the fact that the travel times for the light from various images of the lensing system are unequal and if the source has some intrinsic variability it can be observed at different times in the images. Refsdal (1964) noticed that the time delay allow measuring the Hubble constant, because the time delay is inversely proportional to H_0.

The theory of strong lensing was studied for many decades but scientists had to wait until 1979 for observational evidence. In that year the first strongly lensed quasar, QSO 0957+561, was discovered by Walsh et al. (1979). Today we know around 200 multiply-imaged quasars and the list is still growing. Meanwhile gravitational lensing became one of the leading tools in astrophysics and cosmology. GL provides one of the most accurate mass determinations of distant objects and due to the statistics of gravitational lenses and the properties of the systems like image separation or time delays it is a competitive way of constraining cosmological parameters.

2

THEORETICAL INTRODUCTION

ABSTRACT –

This Chapter is a theoretical introduction to the thesis divided in three Sections: gravitational lensing, cosmology and elliptical galaxies. In the first Section it is briefly presented how gravitational light deflection can be derived from General Relativity. We discuss the lens potential and introduce the the basic lensing equations necessary to understand the rest of the thesis. We also introduce the time delay effect, showing its origin and briefly describing its possible applications. In the second Section we present some basic concepts and discoveries in Cosmology, showing how gravitational lensing stands in this respect. The third Section is dedicated to a specific kind of lensing galaxies. Eighty percent of gravitational lenses are elliptical galaxies, hence this Section is a theoretical introduction to those galaxies and to their stellar dynamics.

2.1 GRAVITATIONAL LENSING

2.1.1 GRAVITATIONAL LENSING IN GENERAL RELATIVITY [1]

The best description of gravitational lensing we have up to now is through Einstein's General Relativity. According Einstein's concept of gravitation, the presence of mass changes the shape of the space-time. Gravitational lensing effects can be derived from Einstein's field equations (EFEs):

$$R_{\mu\nu} - \frac{1}{2} g_{\mu\nu} R + g_{\mu\nu}\Lambda = \frac{8\pi G}{c^4} T_{\mu\nu}, \tag{2.1}$$

where $T_{\mu\nu}$ is the stress-energy tensor, $R_{\mu\nu}$ is the Ricci curvature tensor, R is the scalar curvature, $g_{\mu\nu}$ is the metric tensor, Λ is the cosmological constant and G is the gravitational constant. The cosmological term $g_{\mu\nu}\Lambda$ was introduced later by Einstein to allow for a static Universe.

The EFEs describe the gravitation in terms of curvature of the space-time. The equations determine the space-time geometry depending on the presence of mass. The solutions of these equations are the components of the metric tensor, which can be used to calculate the trajectories of particles or light, the geodesics lines, in the resulting geometry.

An interesting solution of Einstein's equations for gravitational lensing is in the time dependent spherically symmetric metric, this metric is the most convenient to describe the propagation of light in the vicinity of the massive object. If we consider the case where space is empty, except for a mass M situated at $r = 0$, then the solution of Einstein's field equations is:

$$0 = \left(1 - \frac{2MG}{rc^2}\right) c^2 dt^2 - \frac{dr^2}{1 - 2MG/rc^2} - r^2(d\theta^2 + \sin^2\theta d\alpha^2). \tag{2.2}$$

This is the so-called Schwarzschild solution where θ, α and r are the three spherical coordinates, and t is the time.

To calculate the bending angle we need to find the function $\alpha(r)$. Using the approximation that light comes from infinity, passes next to a mass M at a distance ξ, and then goes into infinity, we find that the bending angle is:

$$\alpha = \frac{4MG}{c^2\xi}. \tag{2.3}$$

Einstein's equations can be reduced to Newton's law of gravity by using both the weak-field approximation and the slow-motion approximation.

[1] The material presented in this Section is in part based on Olesen & Ambjørn (2003).

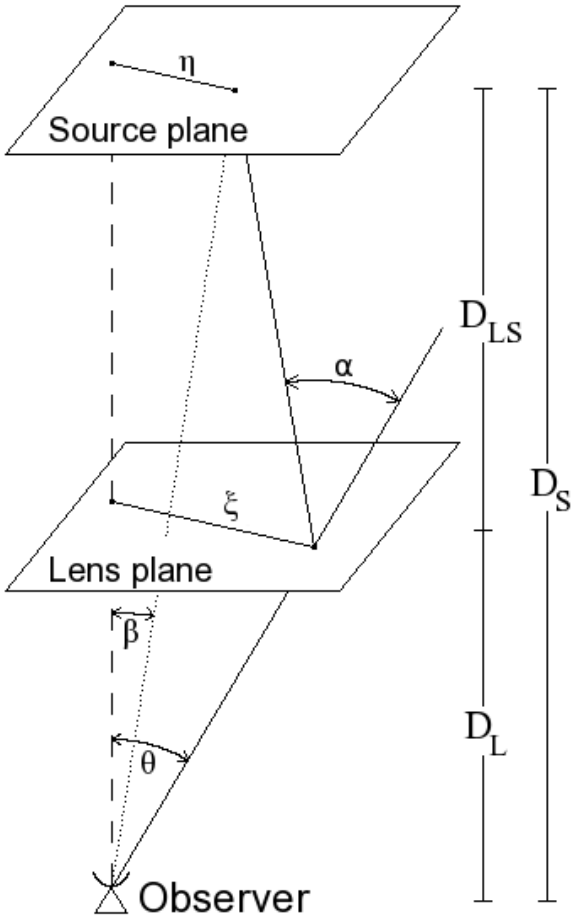

Figure 2.1: *Schematic view of a lensed quasar.*

2.1.2 BASIC LENSING EQUATIONS [2]

Form the previous Section we know that the deflection angle is given by Eq. (2.3). From the geometry of a gravitational lens system, presented in Fig. 2.1, still assuming that the lens is a point and by applying the rule of sines and in the approximation of small angles, we can write the lens equation:

$$\vec{\beta} = \vec{\theta} - (D_{LS}/D_S)\vec{\alpha}(\vec{\theta}). \tag{2.4}$$

As illustrated in Fig. 2.1, $\vec{\theta}$ gives the angular position of the images, $\vec{\beta}$ is the angular position of the source, $\vec{\alpha}$ is the deflection angle and D_S and D_{LS} are the angular diameter distances from the observer to the source and from the lens to the source, respectively.

If we put Eq. (2.4) into Eq. (2.3) and use the geometrical relation: $\xi = D_L\theta$, where D_L is the angular diameter distance from the observer to the lens, we obtain:

$$\beta(\theta) = \theta - \frac{D_{LS}}{D_L D_S}\frac{4GM}{c^2\theta}. \tag{2.5}$$

This equation is showing the relation between source and images position. For the special case where a point source is directly behind a point lens ($\beta = 0$), due to symmetry, the image of a source seen by an observer is a ring which angular radius given by:

$$\theta_{\rm E} = \sqrt{\frac{D_{\rm LS}}{D_{\rm S}D_{\rm L}}\frac{4MG}{c^2}}. \tag{2.6}$$

From the lens equation (2.4) we see that in the non-symmetric case of point like lens there are always two images. The positions of the images are given by:

$$\theta_{\pm} = \frac{1}{2}\left(\beta \pm \sqrt{\beta^2 + 4\theta_{\rm E}^2}\right). \tag{2.7}$$

We see that the point lens produces two images, which are on the two sides of the source, one inside the Einstein ring, the other outside.

The last relation also implies that at least one image will be magnified. Gravitational light deflection preserves surface brightness (Liouville's theorem), but gravitational lensing also changes the apparent solid angle of a source. The total flux received from a gravitationally lensed image of a source is therefore changed in proportion to the ratio between the solid angle of the image and the source (see Fig. 2.2). In other words, the lens is focusing the light. Magnification of the lensed images can be described by equation:

$$\mu = |\frac{\theta}{\beta}\frac{\delta\theta}{\delta\beta}|. \tag{2.8}$$

Using Eq. (2.7) we can obtain the magnification of the two images focused by a point mass lens:

$$\mu_{\pm} = \left[1 - \left(\frac{\theta_E}{\theta_{\pm}}\right)^4\right]^{-1}. \tag{2.9}$$

[2]The material presented in this Section is in part based on the following sources: Schneider (2003), Meylan et al. (2006), Wambsganss (1998).

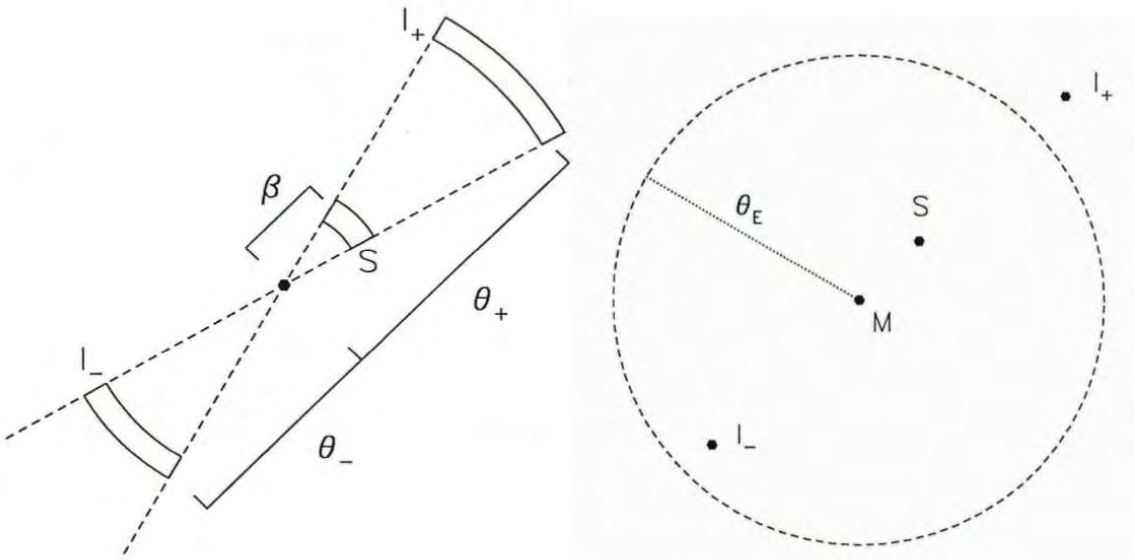

Figure 2.2: *Schematic view of a lensed quasar magnification.*

2.1.3 LENS POTENTIAL[3]

In case of strong lensing, the lens is a galaxy or a group of galaxies, hence it has a three dimensional distributions of matter. Even in the case of lensing by galaxy clusters, the physical size of the lens is much smaller than the distances between observer, lens and source. The deflection therefore is only on a very short part of the light path. This is why we use the 2D plane approximation, and assume that the lens is on the so-called, lens plane. Within this approximation, the lensing matter distribution is described by its surface density, $\Sigma(\vec{\xi})$:

$$\Sigma(\vec{\xi}) = \int \rho(\vec{\xi}, z) dz, \tag{2.10}$$

where $\vec{\xi}$ is a two-dimensional vector on the lens plane and ρ is the three-dimensional density. We can then calculate the dimensionless surface density or convergence:

$$\kappa(\vec{\xi}) = \Sigma(\vec{\xi})/\Sigma_{\rm cr}, \tag{2.11}$$

where the critical surface density is

$$\Sigma_{\rm cr} = \frac{c^2}{4\pi G} \frac{D_S}{D_L D_{LS}}. \tag{2.12}$$

A useful quantity is also the effective lensing potential which is the projected potential of the lens, that can be written in terms of the convergence as:

$$\Psi(\vec{\xi}) = \frac{1}{\pi} \int d^2\xi' \kappa(\vec{\xi'}) \frac{\vec{\xi} - \vec{\xi'}}{|\vec{\xi} - \vec{\xi'}|}. \tag{2.13}$$

Using the 2D approximation one can express the deflection angle, as in Eq. (2.3), at a distance ξ from the center of the lens, by summing the contribution of all the mass elements $\Sigma(\vec{\xi}) d^2\xi$:

$$\vec{\alpha}(\vec{\xi}) = \frac{4G}{c^2} \int \frac{(\vec{\xi} - \vec{\xi'})\Sigma(\vec{\xi'})}{|\vec{\xi} - \vec{\xi'}^2|} d^2\xi'. \tag{2.14}$$

2.1.4 GRAVITATIONAL LENS TIME DELAY[4]

If the source behind a gravitational lens is variable, then those variations will be visible in the images. However, the images will not necessarily vary at the same time, there will be a time delay between the two events. There are two reasons why the images do not vary at the same time.

- Geometrical component of the time delay.

  The distance to each image of the source is different. One can derive the equation of the geometrical time delay from basic trigonometry.

- Gravitational component of the time delay.

  This component of the time delay is due to the fact that the light paths of the images are passing through different parts of lens gravitational potential. It is the so-called Shapiro

[3]The material presented in this Section is in part based on the following sources: Schneider (2003), Meylan et al. (2006), Wambsganss (1998).

[4]The material presented in this Section is in part based on the following sources: Meylan et al. (2006), Wambsganss (1998).

time delay. The gravitational part of the time-delay depends on the 2D mass density profile in the lens, which is the main source of uncertainty on the gravitational part of the time-delay.

The total time delay can be written as:

$$\delta t = \frac{(1+z_L)}{c}\frac{D_S D_L}{D_{LS}}\left[\frac{1}{2}(\vec{\theta}-\vec{\beta})^2 - \Psi(\vec{\theta})\right]. \tag{2.15}$$

It is important to notice that the distances D_L, D_S, and D_{LS} are complicated functions of z, H_0, Ω_M and Ω_Λ (see Eq. 2.22). Moreover lenses are not point sources, in the simplest case lenses are elliptical galaxies, but these galaxies are located inside clusters. So real lenses include the effects of both the galaxy and the cluster.

Time-delays can be measured from photometric monitoring of lensing images. If the source is variable then the variability is visible in the light curves of both images at different times. The time delay can be found from the cross correlation of the two light curves.

In principle it is also possible to compute the time-delay using parameters measured from observations (see Eq. 2.15), although obtaining value of some parameters is often problematic. The easiest to obtain are the positions of the lensed images $\vec{\theta}$. Both the redshifts of the source and of the lens are also needed in the calculation of the time-delay. The lens redshift comes explicitly into the equation in the factor $(1+z_L)$ and the source redshift is implicitly in D_S, the angular diameter distance to the source. Given the small separation between the lensed images and the high luminosity contrast between the source and lens, measuring a redshift of the lens is often observationally challenging. But, the most problematic aspect in calculating the time delay is the lens potential (see a more detailed discussion in the Chapter 3). Finally, also the cosmological parameters Ω_Λ, Ω_M and H_0 enter in the calculation of the time-delay, through the angular diameter distances (see Eq. 2.22).

2.2 COSMOLOGY[5]

Cosmological parameters introduced in the previous Section are basic parameters describing physical properties of the Universe, e.g. shape, mass, age and evolution. Modern cosmology is manly focused on deriving their values. Knowledge of main cosmological concepts and observational facts presented in this Chapter are needed to understand their importance.

2.2.1 THEORY

- **Friedmann equation.**
  All basic equations used in modern cosmology can be derived form Einstein's Field Equations (see Eq. 2.1). Assuming that energy in the Universe is homogenous, perfect fluid with density $\rho(t)$ and pressure $p(t)$, then from EFEs we can derive the equation describing an expansion rate, known as Friedmann equation:

$$H^2 = \left(\frac{\dot{a}}{a}\right)^2 = \frac{8\pi G}{3c^2}\rho - \frac{kc^2}{R_0^2 a^2}, \tag{2.16}$$

  where H is the expansion rate of the Universe, a is a scale factor, R_0 the radius of curvature, k is a constant which takes the values: +1, 0, -1, depending on whether the Universe

[5]The material presented in this Section is in part based on the following source: Olesen & Ambjørn (2003).

is closed, flat or open, respectively and ρ is energy density with three components, density of matter ρ_m, density of Λ and density of radiation ρ_r. Hence ρ can be written as:

$$\rho = \rho_m + \rho_\Lambda + \rho_r. \tag{2.17}$$

The expansion rate of the Universe includes Λ. We notice that Einstein's Field Equations originally did not have the Λ component. EFEs initially were describing contracting Universe, but Einstein's preferred point of view was dynamically stable Universe, thus he added Λ component just to allow for a stationary Universe. With present knowledge, base on observational evidence, we know that Λ might have physical meaning. Λ can be interpreted as a vacuum-energy with the equation of state:

$$p = -\rho\, c^2, \tag{2.18}$$

where p is the negative pressure and ρ is the density. Because of the negative pressure, Λ, acts as an accelerator. Hence, Λ contributes to the expansion rate of the Universe as shown in Friedmann equation (see Eq. 2.16). If we take second derivative of the scale factor we see also that Λ accelerates the expansion:

$$\dot{H} + H^2 = \frac{\ddot{a}}{a} = -\frac{4\pi G}{3c^2}\left(\rho + 3p\right). \tag{2.19}$$

- **The shape of the Universe.**
  Other important parameter describing the Universe is curvature. The curvature of the Universe is conventionally described by the dimensionless density parameter, given by:

$$\Omega = \frac{\rho}{\rho_{\rm crit}}, \tag{2.20}$$

where ρ is the density of the Universe and $\rho_{\rm crit}$ is the critical density given by:

$$\rho_{\rm crit} = \frac{3\,H^2}{8\pi G}. \tag{2.21}$$

This way of describing the Universe curvature gives three possibilities. Positive curvature, $\Omega > 1$, corresponds to a closed Universe, negative curvature $\Omega < 1$, corresponds to an open Universe and $\Omega = 1$ corresponds to a flat Universe where density of a Universe is equal to the critical density given by Eq. 2.21.

As we see from Eq. 2.20 Ω is not only describing curvature but also density. This density similarly like ρ from Eq. 2.17 has three components, the density of matter Ω_M, the density of radiation Ω_r and density of mentioned before vacuum-energy Ω_Λ, known also as dark energy. According to the modern knowledge, dark energy also contributes to the total Universe density.

A present value of H is H_0 and it is a present expansion rate of the Universe called Hubble constant. All distances in the Universe scale with $1/H_0$, thus the Hubble constant at present time is a measure for the size of the Universe. In this thesis all distances are calculated as angular diameter distances, defined in terms of the object actual size. The angular diameter distance is given in terms of Universe geometry Ω_M, Ω_Λ and H_0 by the following equation:

$$D = \frac{c}{H_0\sqrt{|1-\Omega_M-\Omega_\Lambda|}}\,\mathrm{sinn}\int_{z_i}^{z_j} E(z)dz, \tag{2.22}$$

$$E(z) = \frac{\sqrt{|1 - \Omega_M - \Omega_\Lambda|}}{\sqrt{(1+z)^2(1+\Omega_M z) - z(2+z)\Omega_\Lambda}} dz, \tag{2.23}$$

where $\mathrm{sinn}(x)$ is defined as $\sinh(x)$ for open, x for flat and $\sin(x)$ for closed Universe.

The Universe's age is calculated using the expansion rate, and it is corrected based on whether the Universe is accelerating or decelerating. A rapid expansion rate indicates the Universe did not require as much time to reach its present size, and so it is younger than if it were expanding more slowly. If the Universe is flat and composed mostly of matter, then the age of the Universe is $2/3H_0$ and if the Universe is flat with accelerating expansion, then the inferred age is larger than $1/H_0$.

2.2.2 OBSERVATIONAL COSMOLOGY

The simplest known model that is in general agreement with all until now observed phenomena is Λ-cold dark matter (ΛCDM) model. Nowadays, this is the most popular model of the Universe. This model is supported by the following observational facts:

- Universe is expanding – as inferred from spectral observations of galaxies by Hubble in 1929.
- The Universe is approximately flat $\Omega = 1$ – as inferred from cosmic microwave background (CMB) observations by Komatsu et al. (2009).
- The Universe is (most probably) accelerating – as inferred from spectral observations of Type Ia SNe by Riess et al. (1998) and Perlmutter et al. (1999).

As we have learnt from Section 2.2.1 the three quantities Ω_M, Ω_Λ and H_0 are essential for the description of the Universe. Here is a brief summary of recent observations setting constraints on present values of those parameters (see also Fig. 2.3):

- The density of matter is $\Omega_M = 0.3 \pm 0.1$ – as inferred from large scale structure (LSS) studies by (Peacock et al. 2001).
- The density of dark energy is $\Omega_\Lambda \approx 0.7$ – as measured from Type Ia SNe by Riess et al. (1998).
- The Hubble constant is $H_0 = 72 \pm 8$ km s^{-1} Mpc^{-1} – as measured using Cepheids by Freedman et al. (2001).

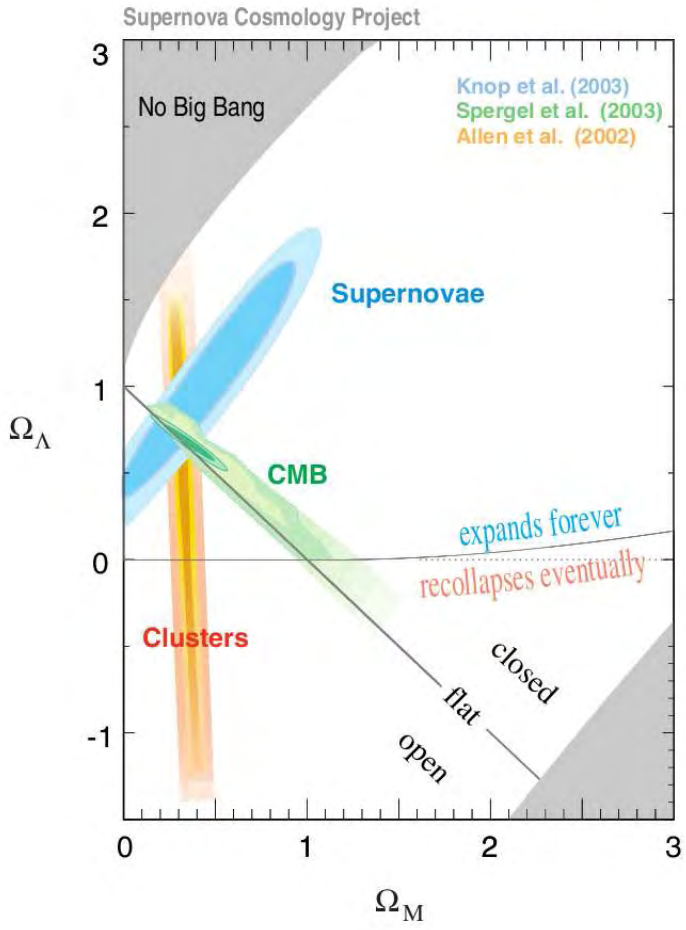

Figure 2.3: *Constraints on Ω_M, Ω_Λ from other major cosmological surveys: the cosmic microwave background (WMAP), supernova Ia and cluster surveys. Credit: the Supernova Cosmology Project (http://supernova.lbl.gov/).*

Those three cosmological parameters can be also derived from GL studies because, both lenses and sources in strong lensing systems are in cosmological distances. Various studies of gravitationally lensed multiple imaged quasars have used the measured time delay between the arrival times of the different images to estimate the Hubble constant H_0 (e.g. Burud et al. 2000, Hjorth et al. 2002, Jakobsson et al. 2005*a*) in it our paper Paraficz et al. (2009) included in this thesis as Chapter 5. In that paper we have used the doubly lensed quasar SDSS J1206+4332. We measured its time delay to be $\Delta\tau = 116^{+4}_{-5}$ days, which, for a singular isothermal ellipsoid model, corresponds to a Hubble constant of 73^{+3}_{-4} km s^{-1} Mpc^{-1}.

Due to degeneracy of H_0 with the mass of the lens the H_0 derived from a lensed system is not reliable. Hence, there have been also attempts to measure H_0 using ensembles of time delay lenses (e.g. Kochanek & Schechter 2004, Oguri 2007, Schechter 2005, Magain 2005, Saha et al. 2006, Coles 2008), again including our paper Paraficz & Hjorth (2009*b*) enclosed in the thesis in Chapter 6. In that paper we present a simultaneous analysis of 18 galaxy lenses with time delay measurements. For each lens we derive mass maps using pixelated simultaneous modeling with shared Hubble constant. We estimate the Hubble constant to be $65.7^{+6.2}_{-3.7}$ km s^{-1} Mpc^{-1} (for a flat Universe with $\Omega_M = 0.3$, $\Omega_\Lambda = 0.7$).

The total matter density, Ω_M, and dark energy content, Ω_Λ, may also be determined using gravitational lensed quasars (see Fig. 2.4 and Fig. 2.5). The number statistics of lenses, as the redshift distribution of the lensed sources, were used by Wambsganss et al. (2004) to constrain cosmology. Simultaneous fitting for both the cosmology and the mass distribution in the lens equation has been used by Golse & Kneib (2002). Moreover Dobke et al. (2009) showed that using parameters (time delay and image separation) measured from future surveys will constrain tightly Ω_M and Ω_Λ. Figure 2.4 presents how time delays can constrain the parameter space Ω_M, Ω_Λ using the MCMC simulations of 125 lensing systems.

Finally, in our paper (Paraficz & Hjorth 2009*a*), included in this thesis in Chapter 7, we show how to efficiently constrain cosmology using strong lenses. In the paper we show that a cosmic standard ruler can be constructed from the joint measurement of the time delay, $\Delta\tau$, between gravitationally lensed quasar images and the velocity dispersion, σ, of the lensing galaxy. Figure 2.5 presents how combination of time delays and velocity dispersions can constrain the parameter space Ω_M, Ω_Λ and H_0 using the MCMC simulations of 20 lensing systems.

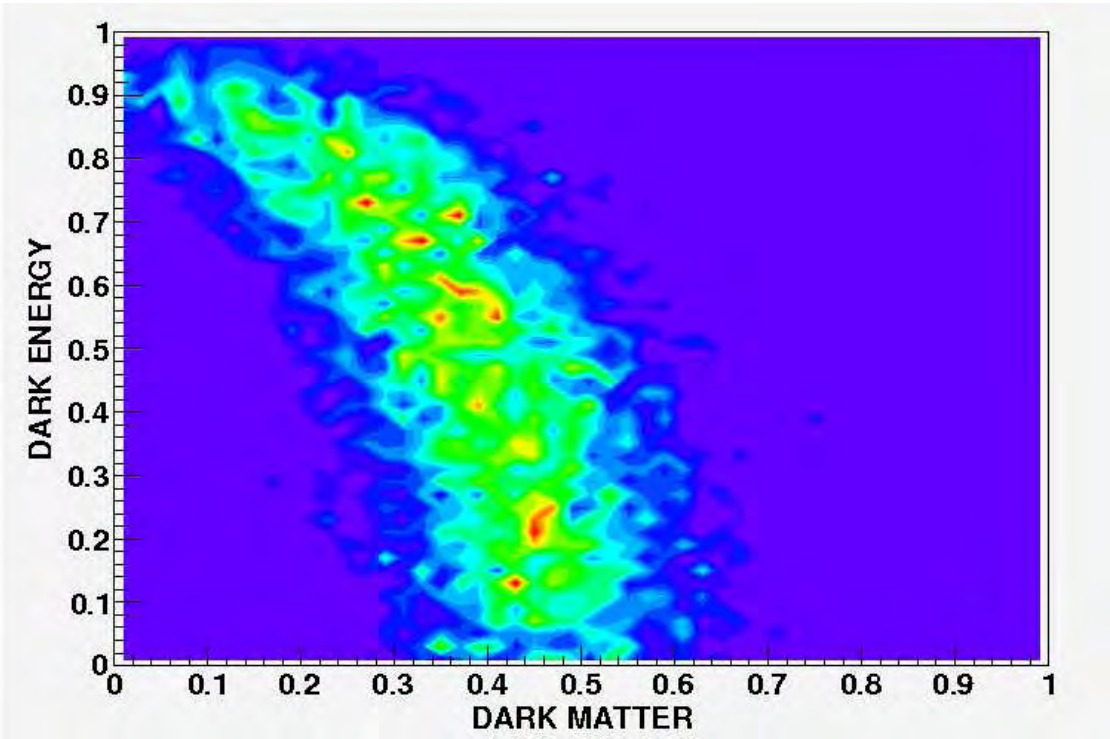

Figure 2.4: *MCMC simulations showing constraints on Ω_M, Ω_Λ set by time delays of multiply lensed quasars.*

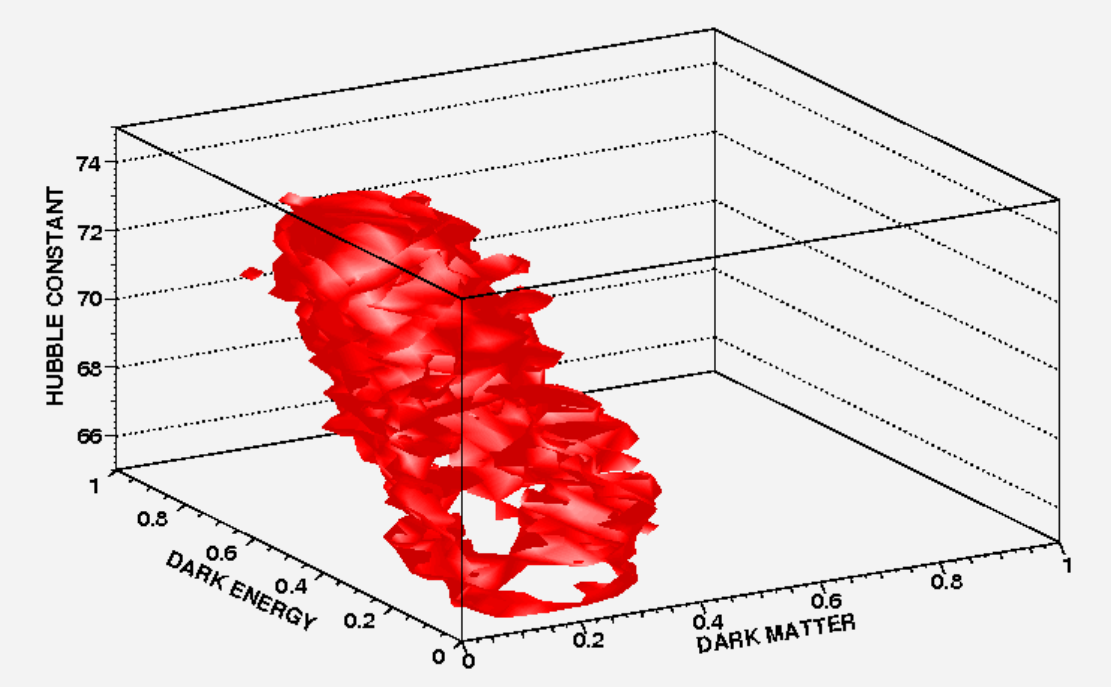

Figure 2.5: *MCMC simulations showing how combination of time delay and velocity dispersion constrain* Ω_M, Ω_Λ *and* H_0.

2.3 ELLIPTICAL GALAXIES[6]

2.3.1 ELLIPTICAL GALAXIES BASICS

Elliptical galaxies are smooth, featureless galaxies with an ellipsoidal shape. Most of them are composed of older, low-mass stars, with little interstellar medium and minimal star formation activity. For long time it was believed that elliptical galaxies have their flattened shape due to rotation. This theory was revised by Davies et al. (1983), who noticed that elliptical galaxies rotate far too slowly given their apparent shapes, hence the shape must be due to anisotropy in the velocity distribution of the stars.

Moreover, a significant fraction of ellipticals show kinematic peculiarities which point to a violent formation process and all elliptical galaxies seem to contain a supermassive black hole. Elliptical galaxies most likely form through the merger of smaller spiral or elliptical galaxies (Toomre 1977). When galaxies collide, dynamical friction combined with tidal forces allowing the galaxies to merge into an amorphous, triaxial system, an elliptical galaxy (Barnes 1988). N-body simulations (see Fig. 2.6) of galaxy pair mergers show that merger remnants have light profiles and kinematics similar to observed ellipticals, although the match is not perfect.

Elliptical galaxies only make up about 10% of all galaxies, but they are much more abundant in regions of high galaxy density, especially in the centers of galaxy clusters where they make up most of the galaxy population (Dressler 1980).

2.3.2 X-RAYS MASS ESTIMATION

The elliptical galaxies mass (but also every other galaxies and galaxies cluster mass) can be extracted from X-ray observation Humphrey & Buote (2009). Considering that a hot intra-galaxy (or intra-cluster) gas supported against gravitation by pressure is described by the hydrostatic equilibrium and combining this assumptions with the fact that gas at high temperatures and low densities follows the ideal gas law then we can get the total mass inside a given radius. Comparison between X-ray observations, simulations and GL mass estimation shows that X-rays gives a good first order description of the average mass distribution.

The comparison between mass estimated for X-ray observations and gravitational lensing has been done in the paper included in this Thesis in Apendix A. We have been investigating possible discrepancy between galaxy cluster masses determined from X-ray and gravitational lensing observations using Abell 1689. The work was based on *Chandra* X-ray observations and a new weak and strong gravitational study based on a Hubble Space Telescope. Comparing X-ray and lensing mass profiles of the regular main part only, shows no significant discrepancy between the two methods and the obtained mass profiles are consistent over the full range where the mass can be reconstructed from X-rays (out to $\approx$ 1Mpc).

2.3.3 PROPERTIES OF ELLIPTICAL GALAXIES

It is possible to determine the mass profiles of ellipticals using a variety of methods, with the analysis of stellar kinematics, from the equilibrium of their X-ray halos, and using statistics of gravitational lenses. The results agree (within relatively large errors) and indicate that ellipticals are surrounded by dark matter halos.

Essential for lensing is that elliptical galaxies seem to be very uniform class of galaxies that follow strictly relations between their physical quantities. We have selected five the most inter-

[6]The material presented in this Section is in part based on Dubinski (1998).

esting for this thesis properties.

- **Isothermality.**

  Several studies have shown that elliptical galaxies may be considered as approximately isothermal (see Fig 2.7) $\rho \propto r^{-2}$ (Koopmans et al. 2006*a*, Oguri 2007, Koopmans et al. 2009, Gerhard et al. 2001). This property of elliptical galaxies is probably the most important property for this thesis. As it is explained in Chapter 3, the strongest degeneracy in lens modeling is degeneracy between time delays and the steepness of the mass profile. This degeneracy causes that without change in the images position, we can change the steepness of the mass profile, hence, the resulting H_0. Thus, if the $\Delta\tau$ and steepness are known (as it is in case of elliptical galaxies $\rho \propto r^{-2}$), H_0 is well constrained. Although the time delays are also influenced by other more complicated degeneracies involving details of the shape of the lens but these effects are secondary (Saha & Williams 2006).

- **De Vaucouleurs law.**

  The stellar density profiles of elliptical galaxies follow the de Vaucouleurs profile, which is the most common empirical profile describing surface brightness of elliptical galaxies. It is given by:

  $$\ln I(R) = \ln I(0) - kR^{1/4}, \tag{2.24}$$

  where R is the distance from the galaxy center and I is the surface brightness.

- **Faber-Jackson relation.**

  The luminosities of elliptical galaxies are highly correlated with their velocity dispersions. The Faber-Jackson relation is generally expressed as a power law:

  $$L \sim \sigma^n, \tag{2.25}$$

  where L is the galaxy luminosity, σ is the central line-of-sight velocity dispersion, and the index n is measured to be ~ 4, but shows significant variations.

- **Hansen-Moore relation.**

  This is a universal relation between the radial density slope $\alpha(r)$ defined as:

  $$\alpha(r) = \frac{d\ln\rho}{d\ln r}, \tag{2.26}$$

  and the velocity anisotropy $\beta(r)$ given by:

  $$\beta(r) = 1 - \frac{\sigma_t^2}{\sigma_r^2}, \tag{2.27}$$

  where $\rho(r)$ is the density, and σ_t^2 and σ_r^2 are the one dimensional tangential and radial velocity dispersions.

  This relation holds for a variety of simulated systems, including elliptical galaxies.

- **The fundamental plane of elliptical galaxies.**

  The fundamental plane (FP) was discovered independently and simultaneously by Djorgovski & Davis (1987) and Dressler et al. (1987).

  They found the plane to be given by:

$$\log r_{\rm e} = 1.325 \log \sigma - 0.825 \log \langle I \rangle_{\rm e} + \text{constant}. \tag{2.28}$$

Since $L = 2\pi \langle I \rangle_{\rm e} {r_{\rm e}}^2$, the FP can also be expressed as a relation between L, σ, and $\langle I \rangle_{\rm e}$, or between $r_{\rm e}$, σ, and L.

This plane is well defined with low dispersion perpendicular to the plane, and a small but significant tilt (implying small changes in the structure of ellipticals as a function of their luminosity or mass). Djorgovski & Davis (1987) found that the thickness of the FP is given by the size of measurement errors, and that the intrinsic scatter has therefore to be very small. The fundamental plane is an important distance indicator for elliptical galaxies, like the Tully-Fisher relation for spirals.

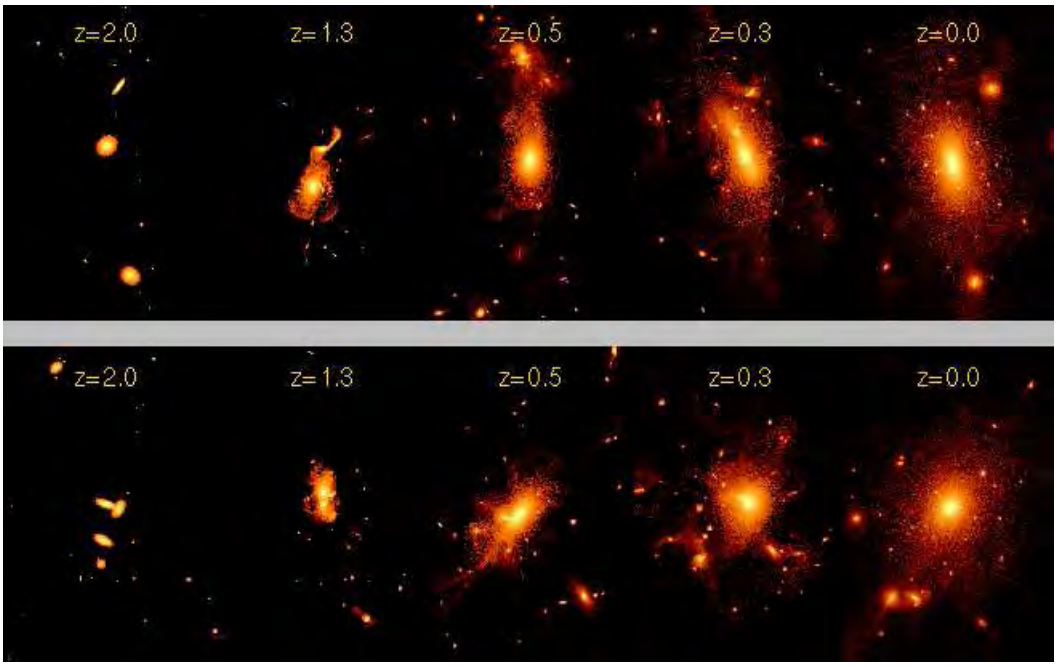

Figure 2.6: *Snapshots of the evolution of the cluster and of the bright central galaxy (BCG). Each tile is 1 Mpc wide. The top strip shows the view perpendicular to the chain of 3 galaxies, which fall together to make the BCG. The bottom strip shows the view looking approximately down the filament. The figure illustrate the evolution and structure of the forming giant elliptical galaxy Dubinski (1998).*

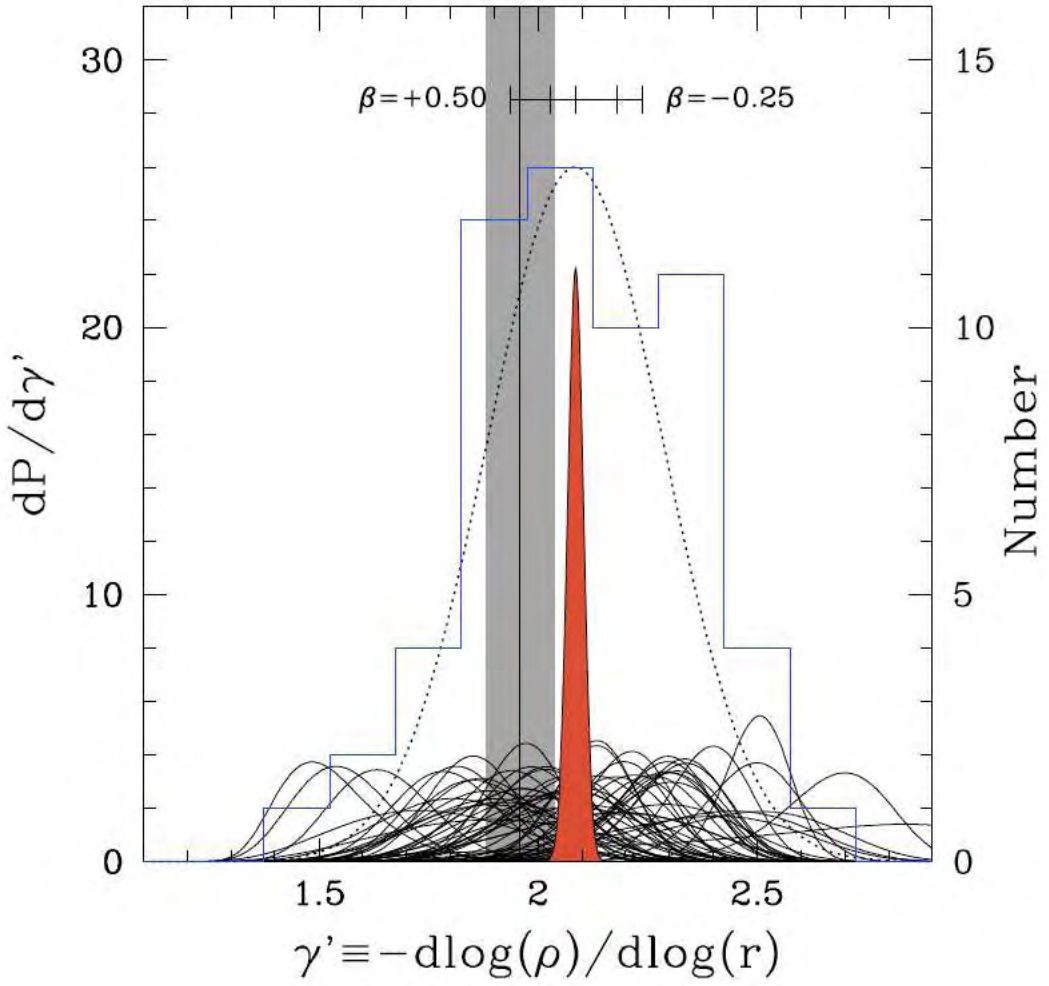

Figure 2.7: *The logarithmic density slopes of 58 SLACS early-type galaxies (thin solid curves). The filled red curve is the joint likelihood of the ensemble average density slope (Koopmans et al. 2009).*

3

LENS MODELING

ABSTRACT –

All the parameters in the time-delay calculations can be measured directly or indirectly from observations, except for the mass surface density distribution $\Sigma(\vec{\theta})$ of the lens. Therefore, some assumptions need to be introduced to model this parameter. Lens modeling is the most challenging part of the gravitational lensing analysis. In this Chapter we present the two standard ways of handling lens models, parametric and non-parametric.

3.1 PARAMETRIC MODELING[1]

The idea of parametric modeling is to create a model with a set of parameters which values are fitted in a way to reproduce all available observables. In principle, the lens model can be constrained from the analysis of galaxy morphology. However, lenses are mostly faint, high-redshift galaxies that are merely, if at all, visible in observations. Hence, modeling lenses needs to rely on indirect measurements.

Since the lenses potential bends the light path of the source, the most basic (and often the only) observables constraining the lens model are the positions of the source images. In some cases we may also know the time delay, and also the positions and properties (steepness of the potential, ellipticity, position angle, velocity dispersion) of one or more lensing galaxies. Those parameters, due to the above mentioned problem, have often the biggest uncertainties. The flux ratios of the lensed images can in principle also constrain the lens model but they are often affected by systematic uncertainties due to extinction within the lens galaxy, microlensing and the effects of substructure. Flux ratios may therefore vary with time and wavelength, and should therefore not be added as a constraint to the model.

Below, we present the two lens models that have been used in this thesis, namely singular isothermal sphere (SIS) and ellipse (SIE). We have used in our work singular isothermal profiles, firstly because these models have simple analytical solutions and secondly because many lenses are actually isothermal. 80% of lenses are massive ellipticals, which have isothermal profiles. Isothermality of elliptical galaxies has been proven by: lens statistics, stellar dynamics, and X-ray galaxies (e.g. Fabbiano et al. 1989, Maoz & Rix 1993, Koopmans et al. 2006*a*, Oguri 2007, Koopmans et al. 2009, Gerhard et al. 2001).

3.1.1 SINGULAR ISOTHERMAL SPHERE (SIS)

The simplest model for galaxy lenses is the singular isothermal sphere, which have the surface mass density given by $\frac{\sigma_v^2}{2G\xi}$,where σ_v is the one-dimensional velocity dispersion and ξ is the distance from the sphere center.

3.1.2 SINGULAR ISOTHERMAL ELLIPSOID (SIE)

A circularly symmetric lens model is too much idealized to describe the properties of real lenses like galaxies or galaxy clusters. Less unrealistic model (SIE) can be obtained by adding two more parameters: the ellipticity and the position angle describing the orientation of the lens.

[1]The material presented in this section is in part based on the following sources: Meylan et al. (2006), Jullo et al. (2007).

3.1.3 PARAMETRIC MODELING IMPLEMENTATION

In this thesis we have used parametric modeling in the implementation of LENSTOOL created by Jullo et al. (2007)[2]. LENSTOOL is software created for modeling strong lensing systems with parametric methods which chooses models using Bayesian evidence. As an example of how parametric modeling works we model the lensing system SDSS J1001+5027 with LENSTOOL.

In Figure 3.1 a deconvolved image (see Section 4.2) of the SDSS J1001+5027 system and the two different models that fit to the observables are presented. We have used three observables to constrain our models: the positions of the images and lens that are visible on the deconvolved image, and the position angle of the lens. The position angle can also be roughly estimated from analysis of the deconvolved image, as the mass profile of a lens tends to align to its visible component (Keeton et al. 1998). We allow this constraint to vary within 45°. We have not used flux ratios because of the discussed above issue.

As free parameters in our modeling we have: the lens velocity dispersion, σ_0 and the ellipticity, ϵ defined as $\epsilon = (a^2 - b^2)/(a^2 + b^2)$, where a and b are the major and minor axis.

#	Type	x (arcsec)	y (arcsec)	σ_0 ($\mathrm{km\ s^{-1}}$)	ϵ	θ_ϵ	$\Delta\tau$ (days)
G1	SIE	1.749	0.861	258	0.23	11°	52
G1	SIS	1.749	0.861	223	0	$\cdots$	34
G2	SIS	1.629	-0.588	159	0	$\cdots$	34

Table 3.1: *Lens model of SDSS J1001+5027. The parameters are galaxy position, x, y, lens velocity dispersion, σ_0, ellipticity, ϵ, position angle, θ_ϵ and time delay, $\Delta\tau$.*

We have created two possible models of the lens environment of SDSS J1001+5027, both models can reproduce the observables. In the first one, the system has only one galaxy with elongated SIE mass profile. From Figure 3.1 we also see that the position angle, P.A., of the model is consistent with the light distribution of the main galaxy but it is also in the direction of the other galaxy. This leads to the conclusion that the quadruple moment might come from the second galaxy rather then from the elongation of the main one.

In the second version of the lens model we set the main lens to be a SIS, and we add as a constraint the position of second lens with SIS mass profile. This model also reproduces the position of the quasar images. The results from both models are presented in Figure 3.1 and summarized in Table 3.1. The predicted time delay of the system is 34 days based on the SIE model and 52 days based on the double SIS model.

[2]http://www.oamp.fr/cosmology/lenstool.

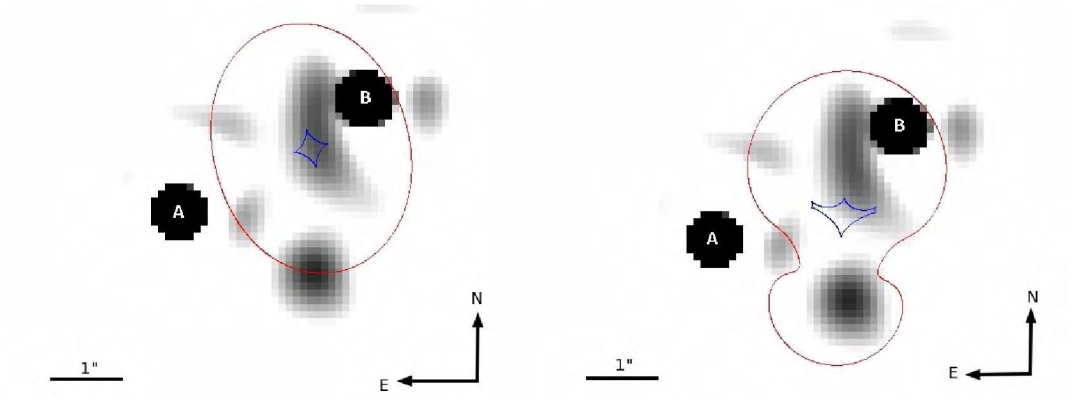

Figure 3.1: *Lens model of SDSS J1001+5027. The figure shows an image of the system with over-plotted results of lens modeling. Blue and red lines represent critical and caustic lines, respectively. The left plot present the single SIE lens model and the right plot presents the double SIS lens model.*

3.2 DEGENERACIES

A good lens model should perfectly reproduce the observables with as little free parameters as possible. When modeling the gravitational potential of the lensing galaxy, as constraints one has usually only two to four quasar images and as we have shown in the previous Section, this is obviously not enough to find a unique solution. In other words, lens models are degenerate.

Degeneracies in lens modeling have been studied in details by Saha (2000), Wucknitz (2002). No matter the precision of the measured astrometry, photometry and time-delays, several mass models will ray-trace the same observables. One must use techniques to break the degeneracies.

The strongest degeneracy is the so-called mass-sheet degeneracy (Gorenstein et al. 1988, Saha 2000, Falco et al. 1985). The projected surface mass density κ can be determined only up to a degeneracy transformation $\kappa \rightarrow \kappa = \lambda\kappa' + (1 - \lambda)$, where λ is an arbitrary constant.

This means that constant mass density added to the lens model does not have to change the position of the images because one can re-scale it and locally change its slope at the position of the images. The observable, which is affected, is the time-delay between images, hence the mass-sheet degeneracy is a serious problem for the determination of the Hubble constant.

Moreover we never know whether the additional constant mass density is due to ellipticity of the lens itself or to intervening objects along the line of sight. Figure 3.2 illustrates this problem. The shear can be produced by ellipticity of the main lensing galaxy, or by the nearby galaxy cluster, however in both cases the image configuration remains unchanged. The logical solution for this problem would be to use only isolated lenses, unluckily most lensing systems are influenced by other galaxies. This comes from the fact that lenses are manly in the dense regions of the cluster (see Chapter 2). A good example of that is our sample of five lensing systems from Chapter 5, three of those systems are strongly affected by clusters (see Fig 3.3). Due to the mass-sheet degeneracy it is important to always include in the modeling all the possible shear coming from intervening objects (Keeton et al. 2000).

The mass-sheet degeneracies can be broken in two ways. First, by measuring the mass profile of the main lens, and the total mass of any intervening cluster along the line of sight. This work can be done with detailed imaging, spectroscopy of all objects along the line of sight, and/or by choosing lenses with known profile e.g. elliptical galaxies are known to be isothermal (see Chapter 2). The second method to break the mass-sheet degeneracy is to find systems where more than one source is at different redshifts behind the lens.

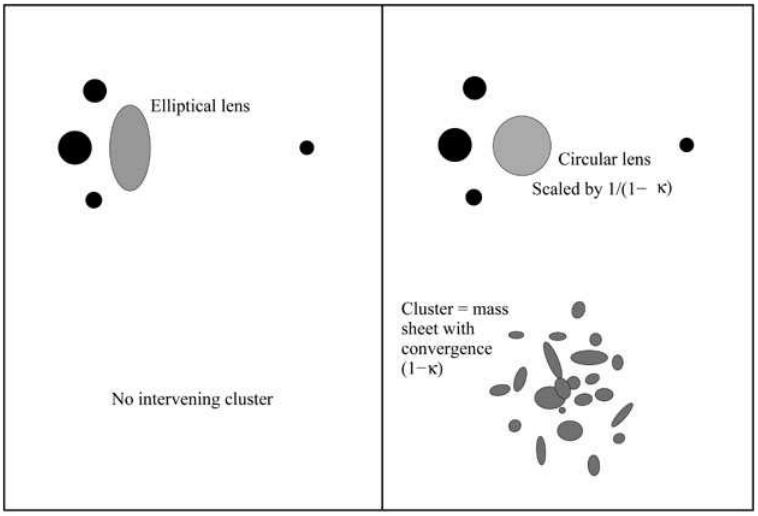

Figure 3.2: *Two ways of obtaining a given image configuration. The left panel displays a system with four images, with an elliptical lens that introduces convergence and shear at the position of the images. On the right panel, is shown the same image geometry and flux ratios, but the lens is now circular. The mass density of the cluster is represented through its convergence κ. The mass of the main lens is scaled with $1/(1-\kappa)$ so that the image configuration remains the same as in the left panel: the masses in the main lens and in the cluster are degenerate. Figure taken from Courbin (2003).*

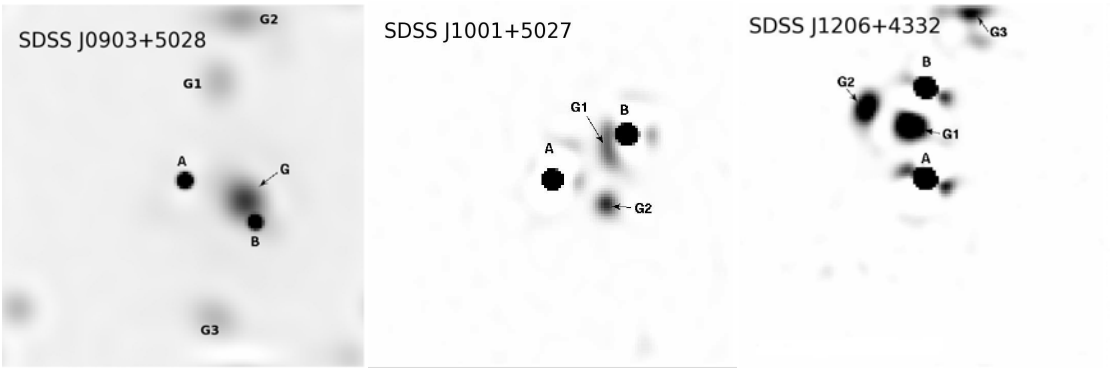

Figure 3.3: *The deconvolved images of the three systems, from left to right, B1608+656, SDSS J1004+4112 and RX J1131-1231. These examples show lenses belonging to rich clusters.*

3.3 NON-PARAMETRIC MODELING[3]

3.3.1 NON-PARAMETRIC MODELING THEORY

The idea behind non-parametric modeling is that the effective lens potential and the deflection equations are linear functions of the surface density. The surface density can be split into any form in which the surface density is represented as a linear combination of density functionals multiplied by unknown coefficients e.g. into multipoles (e.g. Trotter et al. 2000) or pixels (Saha & Williams 2004).

The big advantage of non-parametric modeling is that it does not have all the restrictions of parametric models. This method can find a broad range of different models all reproducing the observables (see Fig. 3.4), thus it can evaluate systematic uncertainties of the mass reconstruction and as a consequence also the systematics in estimating the Hubble constant. Parametric models or sets of parametric models could not provide this to such extent.

The problem is, that good model should reproduce observables with the minimum number of parameters. Unluckily, non-parametric modeling does not always satisfy this requirement. It is often difficult to see whether non-parametric models have a physical interpretation. Also, it can happen that non-parametric models create extra images not seen in the observations. Despite those concerns, pixelated modeling has been successfully used to model lenses also in this thesis.

3.3.2 NON-PARAMETRIC MODELING IMPLEMENTATION

We have modeled various of lensing galaxies in Chapters 5 and 7 using PixeLens, created by Saha & Williams (2004). PixeLens generates large ensembles of models which solves non-uniqueness problem of the parametric modeling and it is designed to model several lenses simultaneously, enforcing consistency of H_0 across different time-delay lenses.

PixeLens has three main observational constraints: image positions, time-delay and images parities. It also imposes secondary constraints based on general knowledge of galaxy mass profiles, here are some of them:

- $\kappa > 0$ (see Eq. 2.11);
- if the galaxy does not appear very asymmetric, the mass profile is required to have inversion symmetry;
- the density gradient anywhere must point within 45° of the lens center;
- the radial mass profile must be steeper than $\rho \propto r^{-0.5}$.

In Chapter 5, we apply PixeLens to all observed systems and compare the results to the parametric modeling obtained with LENSTOOL. Part of such a comparison is presented in the Fig. 3.5. We see that the potentials of the PixeLens correspond quite well to the analytical models giving very similar, not enforced, position angle and ellipticity of modeled lenses.

[3]The material presented in this section is in part based on the following sources: Meylan et al. (2006), Saha & Williams (2004).

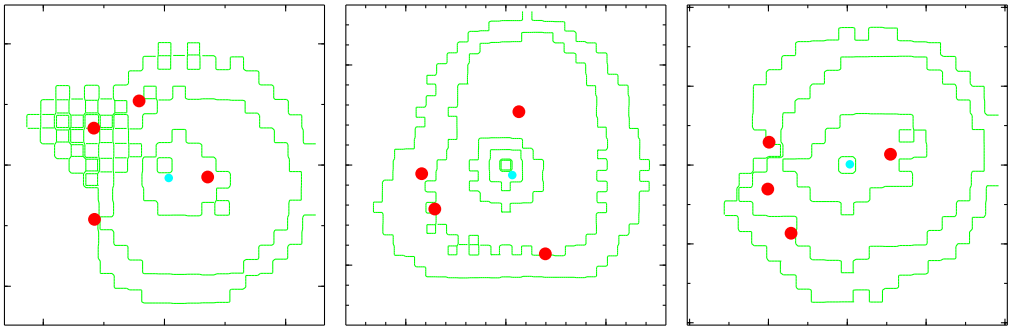

Figure 3.4: *Pixelated mass models of three particularly complicated lensing systems: B1608+656, SDSS J1004+4112 and RX J1131-1231.*

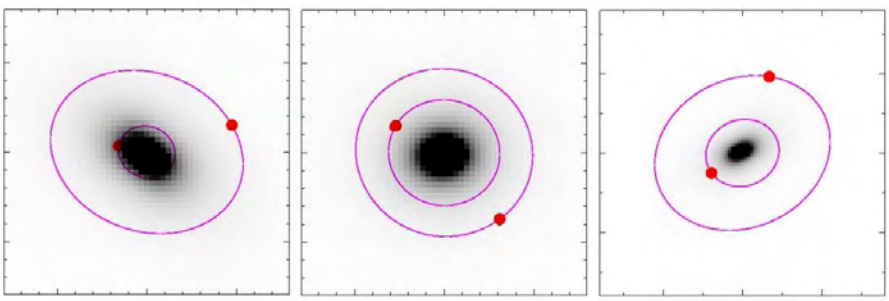

Figure 3.5: *The modeling results of the three lensed quasars. Potential contours modeled by PixeLens which are overplotted on the mass map created in analytical modeling. We see that the potentials of the PixeLens correspond quite well to the analytical models. Form left to right we have: SDSS J1353+1138, SDSS J0903+5028 and SDSSS J1335+0118.*

4

OBSERVATIONS & IMAGE DECONVOLUTION

ABSTRACT –

In this Chapter we describe observations and image deconvolution. The Chapter consists of 2 Sections. In the first one we try to describe all the nuances and logistic problems arising in long-term, frequent-sampling, optical monitoring. In the second one we focus on image deconvolution of the obtained observations. Gravitationally lensed quasars are mostly systems with image separation smaller than the resolution of most present-day telescopes. Hence, in order to separate quasar images, mathematical methods are needed.

4.1 OBSERVATIONS

Our main goal in the first publication of this thesis (see Chapter 5) was to estimate the time delay for 5 lensed quasars. To do that we have carried out a series of monitoring programs, targeting the systems listed in Table 4.1.

Name	Exposure time	R.A	Dec.	Separation ($''$)
SDSS J1001+5027	4 min	10:01:28.61	+50:27:56.9	2.86
SDSS J1206+433	5 min	12:06:29.65	+43:32:17.6	2.9
SDSS J0903+502	10 min	09:03:34.19	+50:28:19.20	2.8
SDSS J1335+0118	5 min	13:35:34.79	+01:18:05.05	1.6
SDSS J1353+1138	3 min	13:53:06.33	+11:38:03.4	1.4

Table 4.1: *Targets properties*

The targets have been selected from the SDSS catalog, we have followed three criteria for selecting the sample: at least half year visibility on the NOT night sky, image separation over $1''.0$ and known redshifts of both the source and the lens.

4.1.1 NOT

The observations for the paper presented in Chapter 5 were gathered from three monitoring programs carried out at the Nordic Optical Telescope (NOT) during two years of my work as a support astronomer.

The NOT is a 2.5-m optical telescope located at the Roque de los Muchachos in La Palma, Spain. Five major observational techniques can be used at the NOT with 9 available instruments:

- optical imaging (ALFOSC, MOSCA, StanCam and LuckyCam);
- near-IR imaging (NOTCam);
- optical and near-IR low-resolution spectroscopy (ALFOSC, NOTCam);
- high-resolution optical spectroscopy (SOFIN, FIES);
- optical polarimetry (ALFOSC, PolCor, and TurPol).

For the monitoring programs optical imaging in R-band with ALFOSC and StanCam was chosen.

From a monitoring point of view, the important advantage of the NOT is its flexibility. Thanks to the flexible scheduling, such a long and frequent monitoring program is possible, however it did not make it easy. NOT has all sorts of possible observing modes: apart from the standard observations, there are also service mode, technical nights, shared nights (between two or more observers), Spanish and International guaranteed time, schools, and frequently interruptions for target of opportunity (ToO) observations. Such a big set of observing possibilities makes the telescope very attractive but also monitoring difficult to execute. Reminding observers to execute the program, deciding when and who will execute the script, and finally monitoring the quality and correctness of the images is in these conditions quite challenging. We have run monitoring program with all the modes listed above, except for the Spanish and International guaranteed time.

4.1.2 MONITORING

Since a monitoring program, compared to usual observations, lasts longer and needs to be consistent and uniform throughout the monitoring period, it meets substantially more difficulties.

- Consistent and uniform sample.
  When choosing targets and instruments for a long period and frequent sampling monitoring one needs to plan the target visibility and availability of the instruments. Especially for our targets, the constant usage of one (maximum two) instruments is a requirement. As it is explained in the next Section, the time delay measurements require deconvolution of the quasar images. For the best efficiency of the presented deconvolution algorithm the uniform and long series of data is needed. Choosing a camera with a bigger field of view (such as MOSCA) in principle would be better for this monitoring (more PSF and reference stars) unfortunately, ALFOSC is chosen more frequently by the observers, hence we used ALFOSC as the primary instrument for this program.

- Frequent sampling.
  Another difficulty with gravitationally lensed quasar observations is microlensing by stars in the lensing galaxy. Microlensing can change the results by about $0.5 - 1.0$ magnitudes and it is completely unpredictable. The disturbing effects of microlensing on sparsely sampled light curves might interfere with the underlying long-term variations and falsify the true time delay. Our programs were designed so that they cope with this issue by sampling the light curves every night. Unluckily nightly sampling was not possible in the end, and we have obtained at most a ~ 2 times per week sampling. The reason for the lost time was $\sim$65% bad weather, $\sim$35% Spanish and International guaranteed time and $\sim$5% technical problems or observer mistakes.

- Good S/N vs short exposure time.
  In three out of five studied quasars we did not detect any variability, this might be due to actual lack of variability, however it could be also due to poor S/N ratio (min $\sim$10 S/N of the fainter component). A compromise had to be set between achieving a good S/N and coping with the time limits set by the NOT Observing Programmes Committee (OPC). Including overheads, the execution time for the monitoring was 15 min. A short exposure time may be also one of the factors why no microlensing was detected in any of the systems.

- Long-term monitoring.
  One of the major challenges in monitoring gravitationally lensed quasars is the lack of prior knowledge of the time delay. Because the time delay is not known, one has to calculate a theoretical time delay before planning the observations. Assuming that the theoretical prediction of the time delay for a given system is a good approximation (which is not always the case) there is still a question as to whether the quasar will vary during the period of monitoring and what will be the timescale and amplitude of the variations. Quasar brightness might vary from a day up to years independently of the mass of the black hole (Wold et al. 2007). We know that the rapid variability implies a light source at very small distance from the black hole (Webb & Malkan 2000), while variations on long time-scales are related to morphological changes of the jets on parsec scales or to accretion-disk instabilities (de Vries et al. 2006). However, it is impossible to predict whether a quasar will vary or not within a given period and timescale, which is why the success of

each quasar monitoring is uncertain. Concluding, time-delay measurements require well-sampled light curves with accurate photometry over a period of time substantially longer than the predicted time delay.

The monitoring programs were built upon previous successful time delay programs (1998-2001) which led to 5 time delays measured at the NOT.

The monitoring programs were run in three periods. During the first period (September 2005 – March 2006) the principal investigator (PI) was Andreas Jaunsen and during periods 2 (October 2006 – March 2007) and 3 (April–September 2007) I was the PI. The detectors used in the monitoring were chosen in order to obtain the most frequent sampling and the best image quality. Thus, we used ALFOSC (the Andalucia Faint Object Spectrograph and Camera; pixel scale $0\farcs189$) whenever it was mounted on the telescope and StanCam (the Stand-by CCD Camera, which is permanently mounted at the NOT; pixel scale $0\farcs176$), otherwise. The seeing varied from $0\farcs4$ to $3\farcs0$ with $1\farcs0$ being the most frequent value.

- The first monitoring program in Period 33 (September 2005 – March 2006), the pilot phase, involved monitoring of the gravitationally lensed system SDSS J0903+5028 at $z = 3.6$ (Johnston et al. 2003) for 10 minutes every night. This system contains two quasar images separated by $2\farcs8$ and aligned on opposite sides of the lensing galaxy at the redshift $z = 0.388$ (Johnston et al. 2003).

- The second program in Period 34 (October 2006 – March 2007) involved monitoring the three selected QSOs with NOT for 15 minutes every night. SDSS J1001+5027 and SDSS J1206+4332 together in one night for 5 minutes each, and SDSS J0903+5028 every second night for 10 minutes.

- After the first two observing seasons we decided to observe four lensed systems alternately. The third observing season Period 35 (April–September 2007), was again divided in two groups. We continued observing SDSS J1001+5027 and SDSS J1206+4332 for 5 minutes each every second night, alternately with two new targets, SDSS J1335+0118 (5 min) and SDSS J1353+1138 (3 min).

4.2 DECONVOLUTION

4.2.1 THEORETICAL DESCRIPTION

The finite size of a point source observed through a telescope has two basic origins. First, the size of an observed image is inversely proportional to the diameter of the primary mirror of a telescope. Second, each observed image from ground is blurred by the turbulent motion of the Earth's atmosphere. There is a way for improving the resolution of an image without increasing the size of the telescope or sending it to space, namely image processing (Magain et al. 1998).

Mathematically speaking, the observed image d_i is the convolution of the real light distribution f_j with the so-called total blurring function or point spread function (PSF), t_{ij}. Thus, the image equation has the form:

$$d_i = \sum_{j=1}^{N} t_{ij} f_j + n_i, \tag{4.1}$$

where N is number of pixels on the CCD camera and n is the noise, i.e. the measured error affecting the data.

The goal of the deconvolution is to obtain the original light f_j using an image, d_i, and a PSF, t_{ij}. Deconvolution is an inverse problem with noise, which means that it does not have a unique solution, it is degenerate. By finding a minimum in the difference between the real image and the mathematical model, one can choose the most probable solution. This method can be additionally improved by putting constraints on the result, e.g. the positivity of the signal, so that solutions with negative intensities can be rejected.

The described general deconvolution theory can have few realizations, and most of them suffer from two basic problems: they produce artifacts in the vicinity of the objects and the ratios of star intensities are not constant.

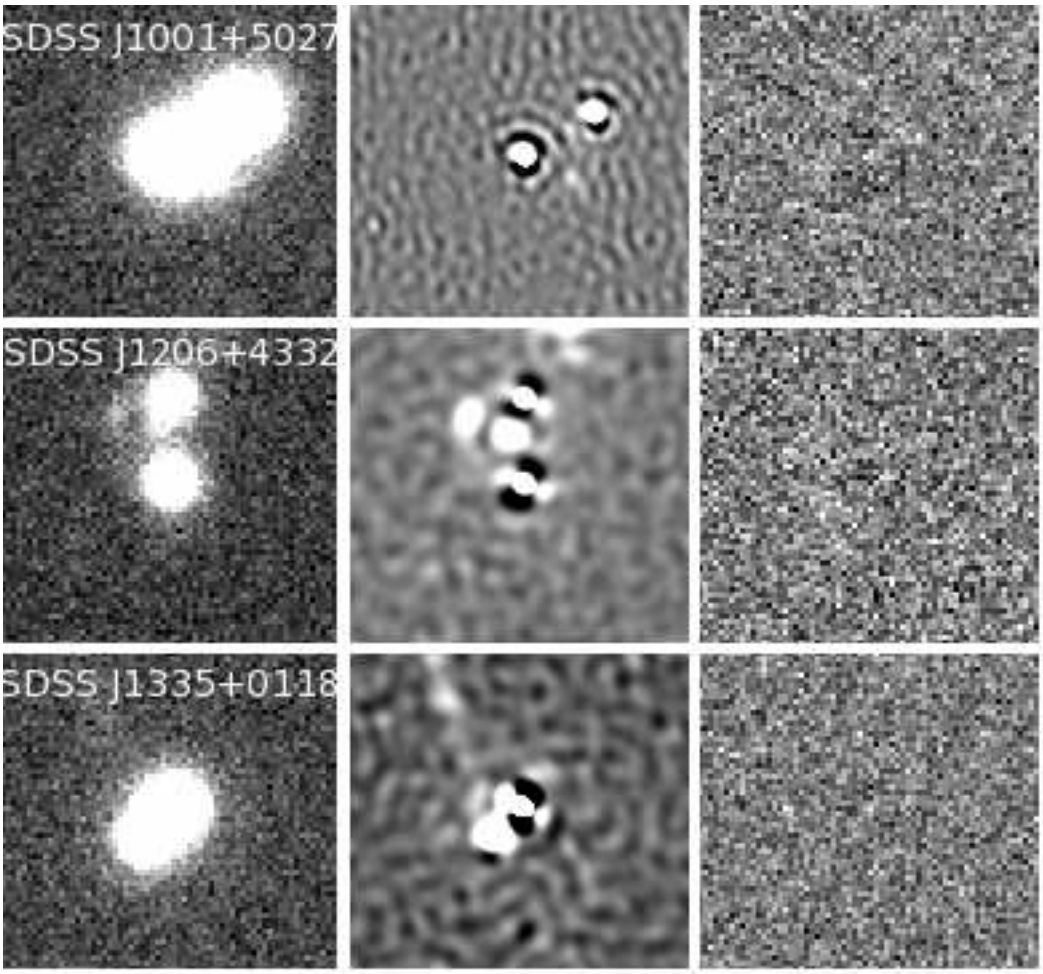

Figure 4.1: *Deconvolution results of the images of three systems.* **Left:** *data image;* **middle:** *mathematical model (deconvolved image);* **right:** *residual image, showing the difference between the real image and the mathematical model.*

4.2.2 APPLICATION

All astronomical images obtained for this thesis (see Chapter 5) were deconvolved by use of the "PSF controlled deconvolution" software created by Magain et al. (1998). The analysis used in the software is based on the theory explained in the previous Section.

This algorithm optimally combines numerous data frames and produces high resolution images. The photometry and astrometry of the point sources in the field are direct by-products of deconvolution. Simultaneous deconvolution of several data frames with the same target keeps point sources at the same positions but permits intensities to vary freely from one image to another. This feature allows constructing precise light curves of strongly blurred, variable and convolved point sources that are superimposed on a bright and complicated background, such as lensed images.

In order to successfully deconvolve an image, a correct PFS has to be derived. The PSF describes the shape of a star in the image, i.e. the two-dimensional profile of the intensity of a star image. The object that is used for extracting PSF has to satisfy the following criteria: it has to be a single point source not far from the target and must have a comparable brightness.

To check whether the final result of the deconvolution is correct one needs to inspect the residuals. Residuals are created from subtraction of the model from the data. They visually show the correctness of the deconvolution process, so that smaller residuals mean a better deconvolution. In practice the resulting residual image should be flat and on average equal to 0. The results from the deconvolution are presented in Fig. 4.1.

5

RESULTS OF OPTICAL MONITORING OF 5 SDSS DOUBLE QSOS WITH THE NORDIC OPTICAL TELESCOPE

Danuta Paraficz, Jens Hjorth and Árdís Elíasdóttir
2009, A&A, 499, 395

ABSTRACT –

We present optical R-band light curves of five SDSS double QSOs (SDSS J0903+5028, SDSS J1001+5027, SDSS J1206+4332, SDSS J1353+1138, SDSS J1335+0118) obtained from monitoring at the Nordic Optical Telescope (NOT) between September 2005 and September 2007. We also present analytical and pixelated modeling of the observed systems. For SDSS J1206+4332, we measured the time delay to be $\Delta\tau = 116^{+4}_{-5}$ *days, which, for a singular isothermal ellipsoid model, corresponds to a Hubble constant of* $73^{+3}_{-4}\ \mathrm{km\ s^{-1}\ Mpc^{-1}}$*. Simultaneous pixelated modeling of five other systems for which a time delay has now been previously measured at the NOT leads to* $H_0 = 61.5^{+8}_{-4}\ \mathrm{km\ s^{-1}\ Mpc^{-1}}$*. Finally, by comparing light curves of the two images of each system, suitably shifted by the predicted or observed time-delays, we found no evidence of microlensing variability over the course of the monitoring period.*

5.1 INTRODUCTION

A gravitationally lensed quasar is a quasar (QSO) that is lensed by a massive foreground object such as a galaxy or a group of galaxies. If the lens is close enough to the line of sight then the quasar is strongly lensed and will be multiply imaged. Due to the different travel times for each light path, any intrinsic variation in the quasar is observed in the images at different times. This time difference, referred to as the time delay, can be measured by comparing the light curves of the images. As first shown by Refsdal (1964), the Hubble constant can be determined from the time delay provided that the mass distribution is known. Conversely, for a fixed Hubble constant, the mass distribution of the lensing galaxy can be constrained.

Determining the Hubble constant from the time delays between light variations in multiple images of gravitationally lensed QSOs is a classical application of lensing in cosmology, but despite 25 years of effort, results remain inconclusive. This partly stems from incomplete knowledge of the mass distribution along the light path to the QSO and partly from the perturbing effects of microlensing on sparsely sampled light curves of the underlying long-term variations.

To address these issues, we have conducted a monitoring program at the Nordic Optical Telescope (NOT) with the aim of obtaining densely sampled light curves of five lensing systems (SDSS J0903+5028, SDSS J1001+5027, SDSS J1206+4332, SDSS J1353+1138, SDSS J1335+0118). Dense sampling is required to quantify the effects of microlensing (Paczynski 1986, Schild 1996, Paraficz et al. 2006) and to maximize chances of determining a time delay from a relatively short monitoring campaign.

Estimating the Hubble constant using time delay measurements is strongly dependent on the underlying mass distribution and hence the choice of lens model (Oguri 2007). Two different approaches to modeling lenses are commonly used. The first one, the non-parametric method (Saha & Williams 1997), generates many models that perfectly fit the data, each of them giving a different time delay which can be then averaged. For the second method, the analytical method(Keeton 2001), one assumes physical properties of the mass distribution of the lens. Comparison of the two approaches gives a useful indication of the systematic errors in e.g. the Hubble constant determined this way.

Luckily, it seems that simple lens models are very good first approximations of the real mass distributions of lenses (Koopmans et al. 2006*a*). Therefore we chose to use the singular isothermal potential to analytically model all the lenses we observe.

In this paper we present the results of a monitoring campaign at the NOT of 5 doubly lensed quasars. We measured the time delay of one of the lensing systems, SDSS J1206+4332, by analyzing light curves of the two quasar images obtained from six months of monitoring, thereby demonstrating the feasibility of short-term monitoring for time-delay measurement. Based on our measurement of the time delay and 5 other time-delay measurements previously obtained

at the NOT, we estimated the Hubble constant.

Section 2 describes the details of our monitoring campaign and Sect. 3 introduces the observed targets. The photometric technique based on image deconvolution is described in Sect. 4 and the light curves of all 5 targets are presented in Sect. 5. In Sect. 6 the time delay of SDSS J1206+4332 is determined. In Sect. 7 we perform a microlensing search in the 5 quasar light curves and estimate upper limits to the microlensing signal. In Sect. 8 we perform analytical and pixeleted modeling. Section 9 is devoted to simultaneous modeling of 5 NOT-determined time delay systems with the aim of a joint Hubble constant estimate. In Sect. 10 we discuss the results.

In the paper we use a flat ΛCDM Universe, $\Omega_{\rm m} = 0.3$ and $\Omega_\Lambda = 0.7$.

5.2 OBSERVATION

The observations were gathered from monitoring programs carried out in the periods September–March 2005/2006, October–March 2006/2007 and April–September 2007 at the Nordic Optical Telescope (NOT); a 2.5-m telescope located at Roque de los Muchachos in La Palma, Spain. The advantage of this telescope is its fairly flexible scheduling, which made almost nightly monitoring possible. Our targets were observed every night under all three operative modes at the NOT: observer, service and technical. However there were severe obstacles preventing frequent sampling: bad weather, Guaranteed Time programs at the NOT and sensitivity of the deconvolution software to imperfectness of the data.

The detectors used in the monitoring were chosen in order to obtain the most frequent sampling and the best image quality. Thus, we used ALFOSC (The Andalucia Faint Object Spectrograph and Camera; pixel scale $0\farcs189$) whenever it was mounted on the telescope and StanCam (the Stand-by CCD Camera, which is permanently mounted at the NOT; pixel scale $0\farcs176$), otherwise. The seeing varied from $0\farcs4$ to $3\farcs0$ with $1\farcs0$ being the most frequent value.

We observed the objects in the R band, only. The pilot phase of the program involved monitoring of a gravitationally lensed system SDSS J0903+5028 at $z = 3.6$ (Johnston et al. 2003) for 10 minutes every night. This system contains two quasar images (see Table 5.3.1) separated by $2\farcs8$ and aligned on opposite sides of the lensing galaxy at the redshift $z = 0.388$ (Johnston et al. 2003).

After the first observing season we decided to observe three lensed systems alternately, SDSS J1001+5027 and SDSS J1206+4332 together in one night for 5 minutes each, and SDSS J0903+5028 every second night for 10 minutes. The third observing season was again divided in two groups. We continued observing SDSS J1001+5027 and SDSS J1206+4332 for 5 minutes each every second night, alternately with two new targets, SDSS J1335+0118 (5 min) and SDSS J1353+1138 (3 min). The exposure times were chosen so that the signal-to-noise ratio of the fainter component of each system would be above 10. Finding charts of all the targets are presented in Figures 5.1 to 5.5.

One of the major challenges in monitoring gravitationally lensed quasars is the lack of prior knowledge of time delay. Thus, time-delay measurements require well-sampled light curves with accurate photometry over a period of time substantially longer than the time delay. Because the time delay is not known, one has to calculate a theoretical time delay before planning the observations.

Assuming that the theoretical prediction of the time delay for a given system is a good approximation (which is not always the case) there is still a question as to whether the quasar will vary during the period of monitoring and what will be the timescale and amplitude of the

variations. Quasar brightness might vary from a day up to years independently of the mass of the black hole (Wold et al. 2007). We know that the rapid variability implies a light source at very small distance from the black hole (Webb & Malkan 2000), while variations on long time-scales are related to morphological changes of jets on parsec scales or to accretion-disk instabilities (de Vries et al. 2006). However, it is impossible to predict whether a quasar will vary or not within a given period and timescale, which is why the success of each quasar monitoring is uncertain.

Another difficulty with gravitationally lensed quasar observations is microlensing by stars in the lensing galaxy. Microlensing can change the results by about $0.5 - 1.0$ magnitudes and it is completely unpredictable (Chang & Refsdal 1979).

Thus, in order to get a time delay one has to monitor quasars with high sampling, so that events like microlensing can be extracted from the quasar variability in further analysis. Our monitoring program was designed to minimize this problem.

Observation planning, monitoring supervision and image reduction was made by the first author during her stay at the NOT. Data reduction was performed using IRAF reduction utilities.

5.3 TARGETS

The individual targets observed are introduced below. The astrometry and redshifts of the quasars images and the lenses are summarized in Table 5.3.1.

5.3.1 SDSS J0903+5028

SDSS J0903+5028, a doubly lensed quasar system, was discovered from the Sloan Digital Sky Survey by Johnston et al. (2003). Using the ARC 3.5 meter telescope it was found that the system has two quasar images separated by $2\farcs8$ with the lens, a red galaxy ($z = 0.388$), in between. Spectroscopic follow up observation at the Keck II telescope proved that the two objects are the images of one quasar at $z = 3.6$. Johnston et al. (2003) concluded that other galaxies in the vicinity of the lensing galaxy might be gravitationally bound with the lens, adding external shear to the lensed system.

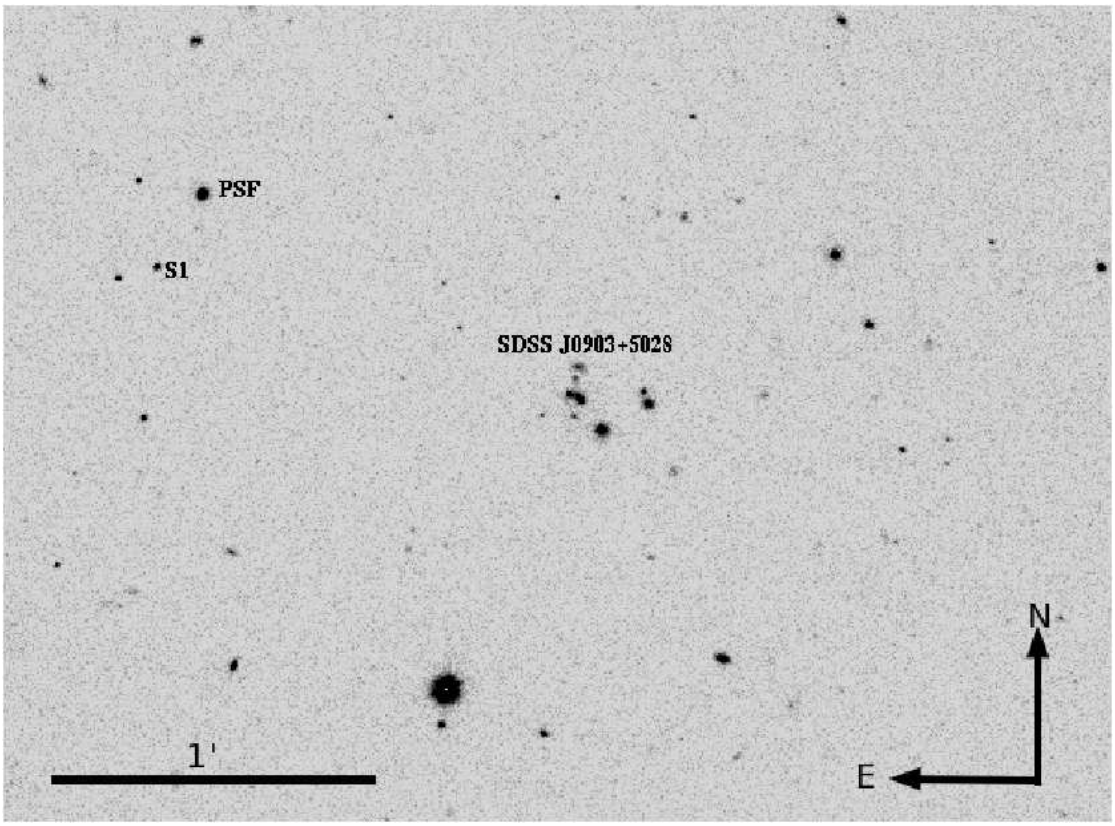

Figure 5.1: *Finding chart of the system SDSS J0903+5028. The reference star (S1) and the star used to model the PSF are indicated.*

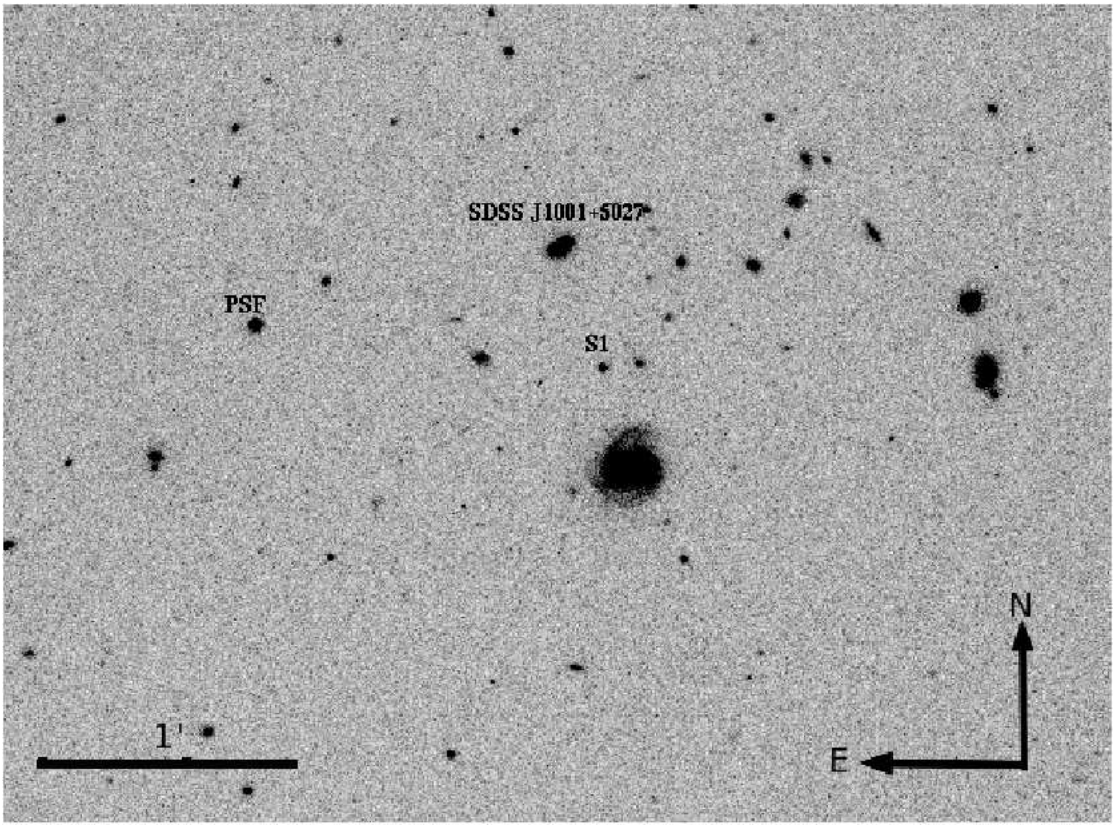

Figure 5.2: *Finding chart of the system SDSS J1001+5027. The reference star (S1) and the star used to model the PSF are indicated.*

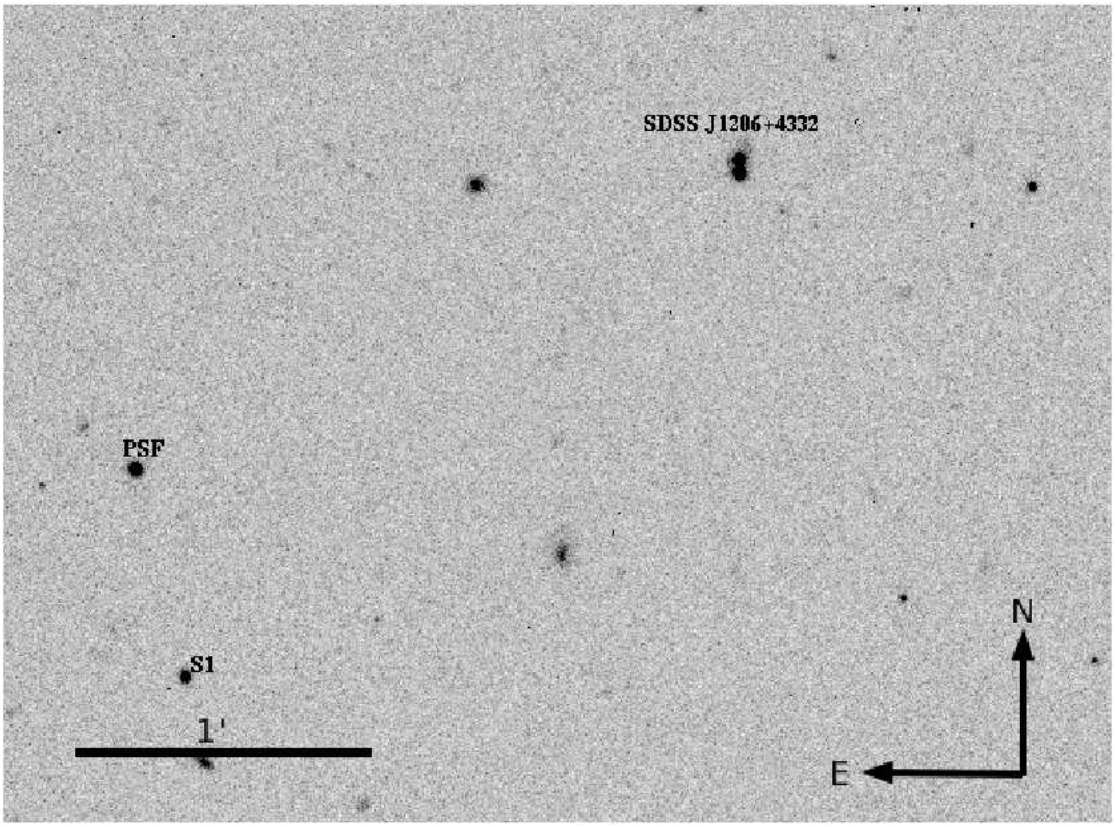

Figure 5.3: *Finding chart of the system SDSS J1206+4332. The reference star (S1) and the star used to model the PSF are indicated.*

	SDSS J0903+5028		
Object	R.A. (J2000.0) (h:m:s)	Dec. (J2000.0) (d:m:s)	z
A	09 03 35.13	+50 28 20.21	3.6
B	09 03 34.88	+50 28 18.75	3.6
G	09 03 34.93	+50 28 19.53	0.388
	SDSS J1001+5027		
Object	R.A. (J2000.0) (h:m:s)	Dec. (J2000.0) (d:m:s)	z
A	10 01 28.61	+50 27 56.9	1.838
B	10 01 28.35	+50 27 58.5	1.838
	x (arcsec)	y (arcsec)	z
G1	1.779 ± 0.049	0.857 ± 0.123	$0.2 \leq z \leq 0.5$
G2	1.795 ± 0.088	-0.700 ± 0.053	$0.2 \leq z \leq 0.5$
	SDSS J1206+4332		
Object	R.A. (J2000.0) (h:m:s)	Dec. (J2000.0) (d:m:s)	z
A	12 06 29.65	+43 32 17.6	1.789
B	12 06 29.65	+43 32 20.6	1.789
	x (arcsec)	y (arcsec)	z
G1	-0.664 ± 0.137	1.748 ± 0.028	0.748
G2	1.320 ± 0.147	5.999 ± 0.148	≥ 0.7
G3	$+2.052 \pm 0.200$	2.397 ± 0.152	blue
	SDSS J1335+0118		
	x (arcsec)	y (arcsec)	z
A	0.000 ± 0.001	0.000 ± 0.001	1.57
B	-1.038 ± 0.002	-1.165 ± 0.002	1.57
G	-0.769 ± 0.011	-0.757 ± 0.011	0.44
	SDSS J1353+1138		
	R.A. (J2000.0) (h:m:s)	Decl. (J2000.0) (d:m:s)	z
A	13 53 06.35	+11 38 04.81	1.63
B	13 53 06.08	+11 38 01.43	1.63
G	13 35 06.10	+11 38 00.39	~ 0.3

Table 5.1: *Astrometric properties and redshifts. All x,y positions are relative to the A component and their errors do not include the error of the image scale. The positive direction of the those coordinates are to the west and north, respectively.*

5.3.2 SDSS J1001+5027 & SDSS J1206+4332

SDSS J1001+5027 and SDSS J1206+4332 were recognized as lensing candidates in a strong lensing survey using the Sloan Digital Sky Survey. Oguri et al. (2005) photometrically and spectroscopically confirmed using the ARC 3.5 meter and University of Hawaii 2.2-meter telescopes, that those two targets are indeed lensing systems. They reported that SDSS J1001+5027 and SDSS J1206+4332 have image separation of 2.″86 and 2.″90 respectively with the source objects being quasars at $z = 1.838$ and $z = 1.789$.

Oguri et al. (2005) noted that the two lensing galaxies of SDSS J1001+5027 have colors consistent with those of early-type galaxies at $0.2 \leq z \leq 0.5$. SDSS J1206+4332 appears to have three lensing galaxies where the main lens, G1, has an associated absorber at redshift $z = 0.748$, the second galaxy, G2, is identifed as a high redshift galaxy $z \leq 0.7$ and, the third galaxy, G3, is a blue galaxy. Oguri et al. (2005) using the *lensmodel* software (Keeton 2001) modeled the two systems showing that they are both strongly affected by the potential of more than one galaxy.

5.3.3 SDSS J1335+0118

SDSS J1353+1138 is a doubly lensed system, discovered in the Sloan Digital Survey by Oguri et al. (2004). The photometric follow up made at the Subaru 8.2-m and Keck I telescopes confirmed that the system consists of two gravitationally lensed images separated by 1.″56 with a single lensing galaxy in the centre. Spectroscopic observations made at the ESO New Technology Telescope (NTT) showed that the A and B components of the system are images of a quasar at redshift $z = 1.57$. Eigenbrod et al. (2006*a*) reported that the lensing galaxy is a low-redshift galaxy with $z = 0.44$.

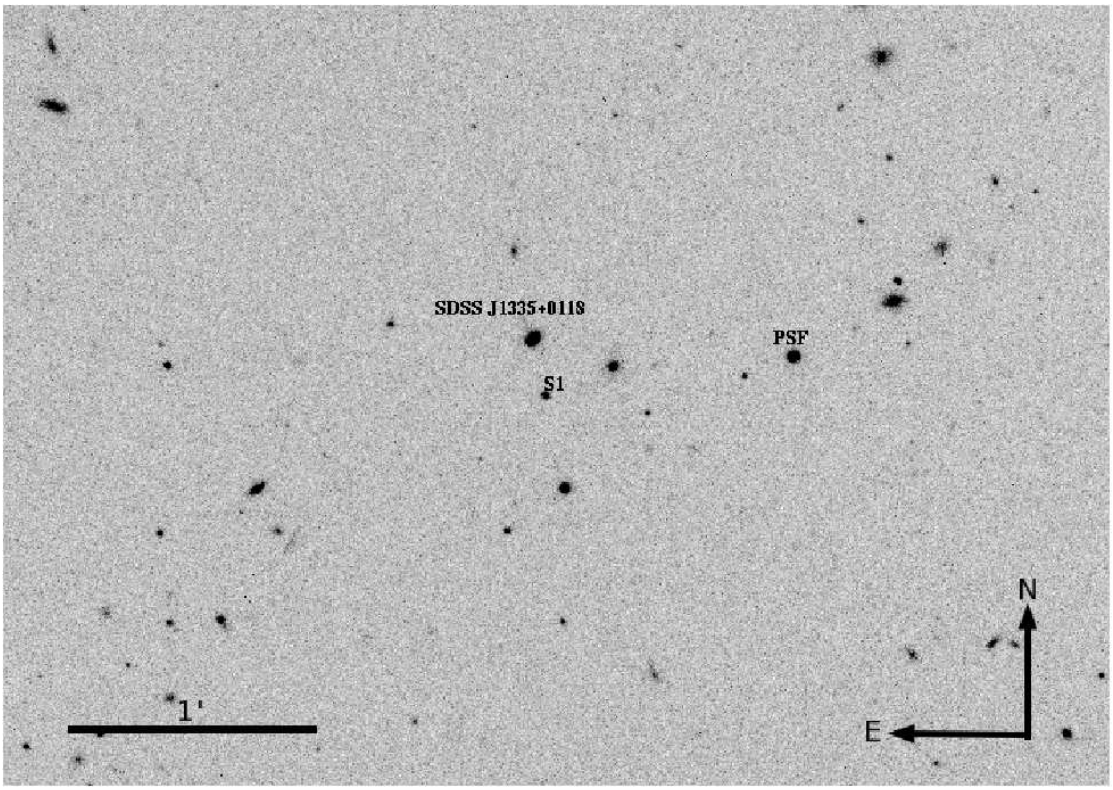

Figure 5.4: *Finding chart of the system: SDSS J1335+0118. The reference star and the star used to model the PSF are indicated*

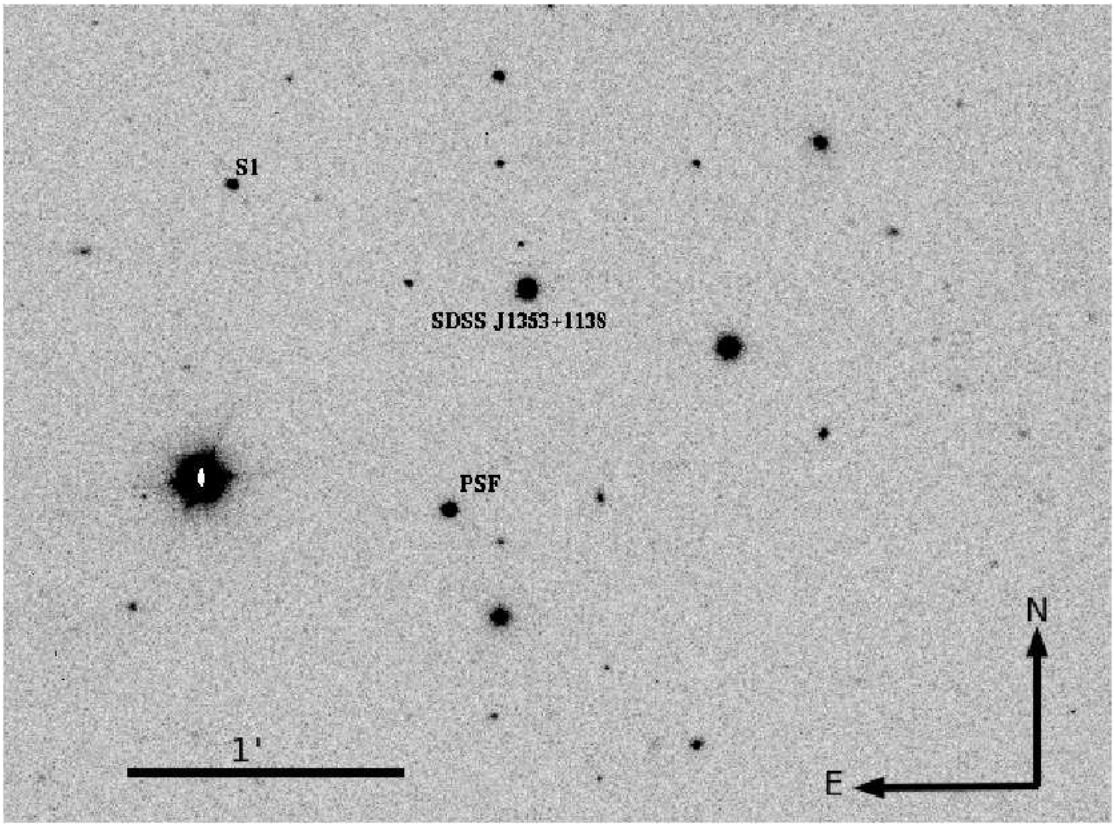

Figure 5.5: *Finding chart of the two system SDSS J1353+1138. The reference star and the star used to model the PSF are indicated*

5.3.4 SDSS J1353+1138

Inada et al. (2006) discovered the SDSS J1353+1138 lensed quasar system from SDSS lensed quasar survey. For imaging and spectroscopy Inada et al. (2006) used the University of Hawaii 2.2-m telescope, the Keck I and II telescopes and the Magellan Consortium's Landon Clay 6.5-m telescope. The observations showed that the two quasar components separated by $1\farcs41$ have redshift $z = 1.629$ and the lensing galaxy in between the images is at $z \sim 0.3$.

5.4 PHOTOMERY AND IMAGE DECONVOLUTION

5.4.1 IMAGE DECONVOLUTION

Time delay estimation requires high precision photometry separately for each lensing image. Since our targets are small angular separation systems we need to use a mathematical method, deconvolution, to separate the images.

An observed image is a convolution of a real light distribution with the so-called total blurring function or point spread function (PSF). The goal of the deconvolution is to extract the brightness of a source using knowledge about the PSF. Deconvolution is an inverse problem without a unique solution. The method used for choosing the best solution is minimization of the difference between a model and a real image.

All data used in this paper were deconvolved using the PSF Controled Deconvolution software created by Magain et al. (1998). In this software the input are the position and intensities of the images, which need to be well defined to succeed. We take the image positions from previous studies because these were better resolved and the quasar postions well determined (see Table 5.3.1).

In Figure 5.6 we present the deconvolution results for the observed targets. On the left are shown the deconvolved images (mathematical models of lensing systems) and on the right the data images. We can see that the deconvolution reveals not only the quasars images but also the lensing galaxies which are not visible in the raw data.

5.4.2 PHOTOMETRY

Photometry of all objects presented in this paper was made using the PSF Controled Deconvolution software (Magain et al. 1998). The software deconvolves all frames of a given object simultaneously, it constrains the position of the images and lensing galaxies and allows the magnitude of the quasar images to vary freely. The algorithm has been implemented in various analysis of quasars (Burud et al. 2000, Burud, Courbin, Magain, Lidman, Hutsemékers, Kneib, Hjorth, Brewer, Pompei, Germany, Pritchard, Jaunsen, Letawe & Meylan 2002, Burud, Hjorth, Courbin, Cohen, Magain, Jaunsen, Kaas, Faure & Letawe 2002*a*, Hjorth et al. 2002, Jakobsson et al. 2005*b*, Vuissoz et al. 2007, Eigenbrod et al. 2006*b*).

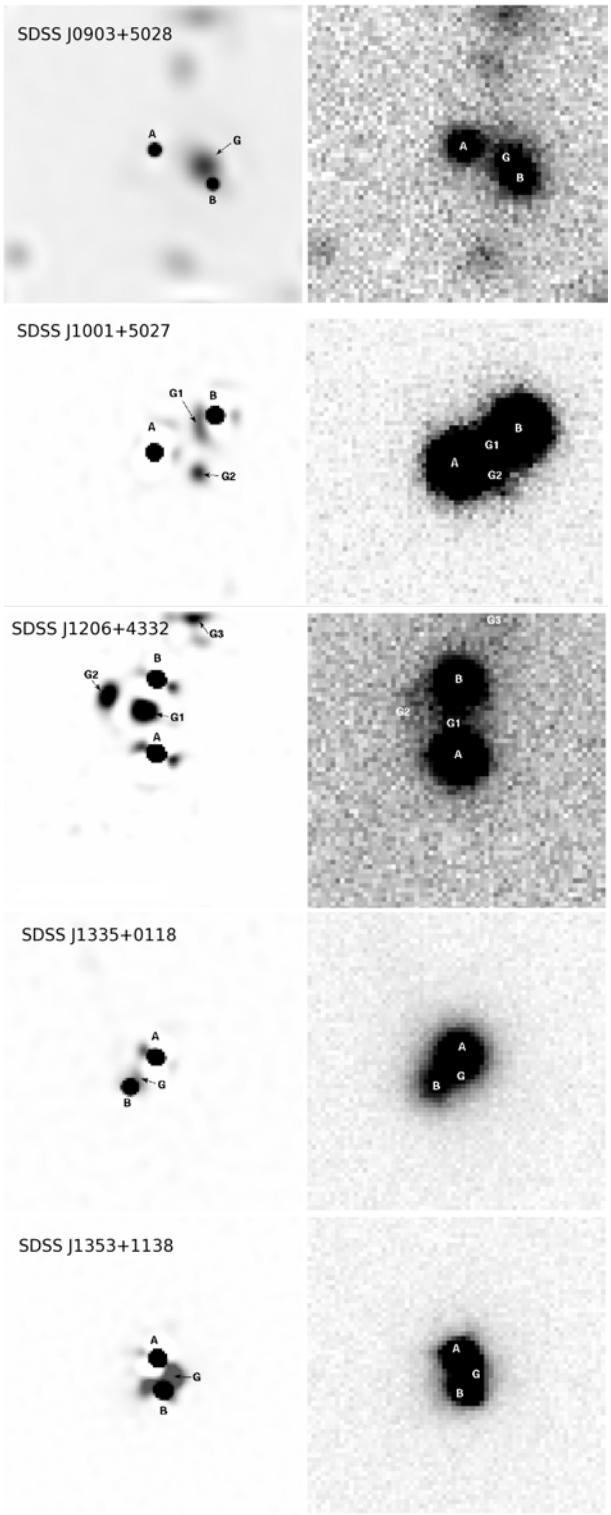

Figure 5.6: *Results of the deconvolution of the 5 systems. On the left are deconvolved images and on the right original images. The deconvolution reveals not only quasar images but also the lensing galaxy which is otherwise not visible.*

The light curves of SDSS J0903+5028, SDSS J1335+0118, SDSS J1353+1138, SDSS J1001+5027, SDSS J1206+4332 consist of 34, 31, 31, 24, 34 R-band data points, respectively, as presented in Figures 4-8. Data were taken from two optical cameras, ALFOSC (marked in black) and StanCam (marked in blue). The magnitudes are calculated relative to the PSF magnitude marked on the finding charts (Figures 5.1, 5.2, 5.3, 5.4 and 5.5). Due to the small field of view and comparatively small sensitivity of StanCam and lack of bright stars next to our targets the reference stars presented in the plots are only from ALFOSC. The reference star images were also deconvolved to look for systematic errors in the deconvolution and to estimate the photometric uncertainties. Assuming that reference stars are not intrinsically variable any variability seen in their light curves must be due to photometric and deconvolution uncertainties. The error bars of the quasar images and the reference stars coming from ALFOSC are the averaged photon noise and uncertainties measured from the variations of the reference stars combined in quadrature. For data points from StanCam we have assumed one standard error bar of 0.02 mag which should approximately include all uncertainties. In the case of ALOSC data of SDSS J0903+5028 and StanCam data of SDSS J1335+0118 there were no non-variable star in the field except PSF star, thus the error bars of the quasar magnitude are set to 0.02 mag., which is the approximate photometric uncertainty of the B image in average atmospheric conditions.

5.5 LIGHT CURVES

5.5.1 QSOS WITH LITTLE VARIABILITY

In 3 of the 5 systems (SDSS J0903+5028, SDSS J1335+0118, SDSS J1353+1138) no significant variability was observed. In Figures 5.7, 5.8 and 5.9 we plot the light curves of the three systems. By visual examination we see no variability in the quasar images.

In order to see whether small fluctuations in the light curves say something about the time delay we fitted polynomials to the light curves of the A counterpart. These were then fitted to the B light curves with magnitude and time shift. Since there are no visible peaks in either light curves, the magnitude shift was chosen simply by taking a difference between average magnitude of image A and image B. The time shift is taken from the theoretical prediction of the time delay of those systems (see Section 8). The fitted polynomials do not show any preferred time shift. This means that due to the lack of quasar variability during the time span of the monitoring we did not manage to measure time delays in these systems.

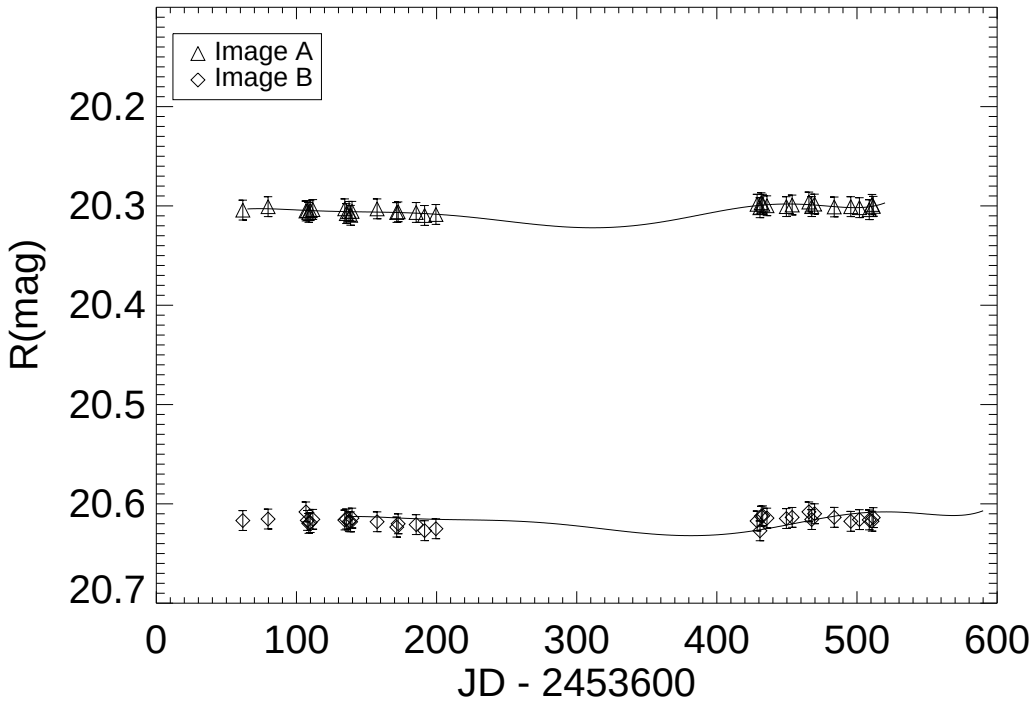

Figure 5.7: *R-band light curves of SDSS J0903+5028. A polynomial is fitted to the light curve of A counterpart. This polynomial was also fitted to the B image with magnitude and time shift (see Table 5.2).*

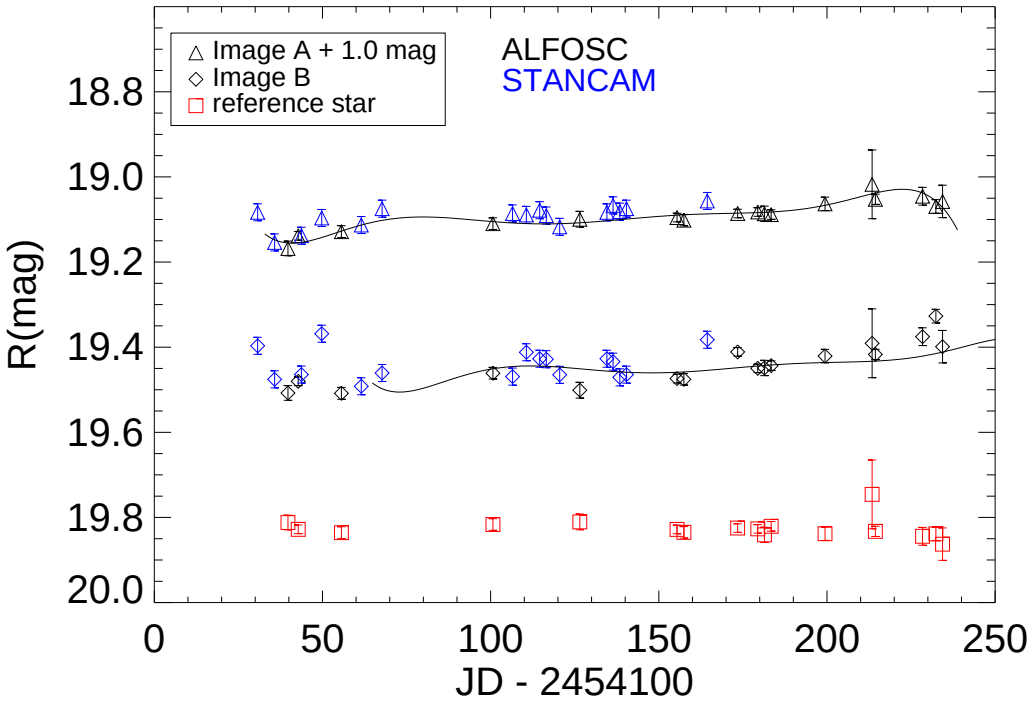

Figure 5.8: *R-band light curves of SDSS J1335+0118. A (diamonds) and B (triangles) images of the quasar are plotted with black and blue colors indicating weather data coming from ALFOSC or StanCam. The reference star is plotted with red squares. A polynomial is fitted to the A counterpart of the quasars light curve. This polynomial is also fitted to the B image with magnitude and time shift. The time shift is taken from the theoretical prediction of the time delay of this system (see Table 5.5).*

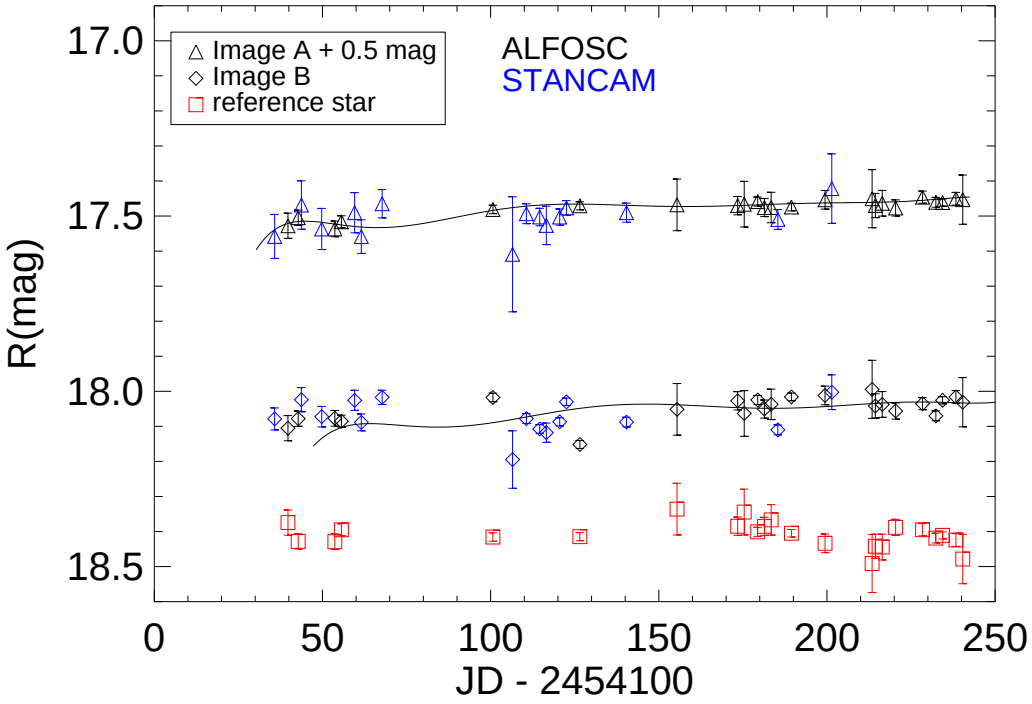

Figure 5.9: *R-band light curves of SDSS J1353+1138. Shapes and colors of the data point and fitting procedure identical with previous light curve. The time shift is taken from the theoretical prediction of the time delay of those systems (see Table 5.6).*

5.5.2 QUASARS WITH VARIABILITY

In 2 out of the 5 monitored gravitationally lensed quasars variability was detected. In Figure 5.10 and 5.11 we show the light curves of SDSS J1001+5027 and SDSS J1206+4332, respectively.

SDSS J1001+5027

Figure 5.10 shows the light curves of SDSS J1001+5027 quasar images. We see that both images have some small variabilities in the light curve and also that both the A and B images have steadily decreased their brightness.

We have fitted a 7th order polynomial (see Figure 5.10 - black solid line) to the A data set. This was then fitted to the B light curve with magnitude shift which is the average magnitude difference between light curves (0.4 mag) and time shift which is the predicted time delay (52 days).

We also have fitted a straight line to light curves (see Figure 5.10 – red dashed lines). The linear regression shows that both light curves have very similar evolution. Both images decreased their brightness by 0.2 magnitude during the first 200 days. This indicates that the brightness decrease is due to long intrinsic quasar variability de Vries et al. (2003).

Although variability is clearly visible, it is impossible to measure the time delay for this system just from the slope. The small fluctuations on the slope also do not give any conclusive results, neither visual shifting nor polynomial fitting help to find the time delay.

SDSS J1206+4332

In Figure 5.11 we show the light curve of SDSS J1206+4332. We see clear long variabilities for both the A and B light curves. The variabilities are 100–150 days long, so the gaps in the sampling do not strongly influence the precision of the time delay estimation. The observed variabilities, consisting of bumps, allow for measurement of the time delay for SDSS J1206+4332, as detailed in section 6.

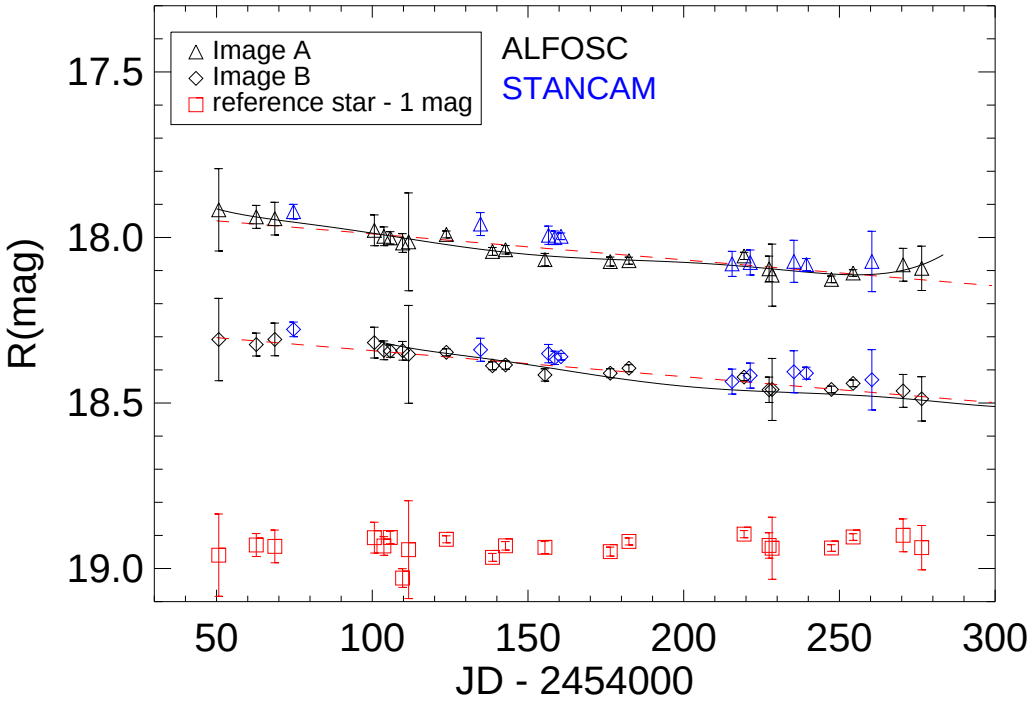

Figure 5.10: *R-band light curves of SDSS J1001+5027. Polynomials (solid, black lines) and linear regressions (dashed, red lines) are fitted to the A and B counterpart of the quasars separately. Shapes and colors of data point identical as described on previous plots.*

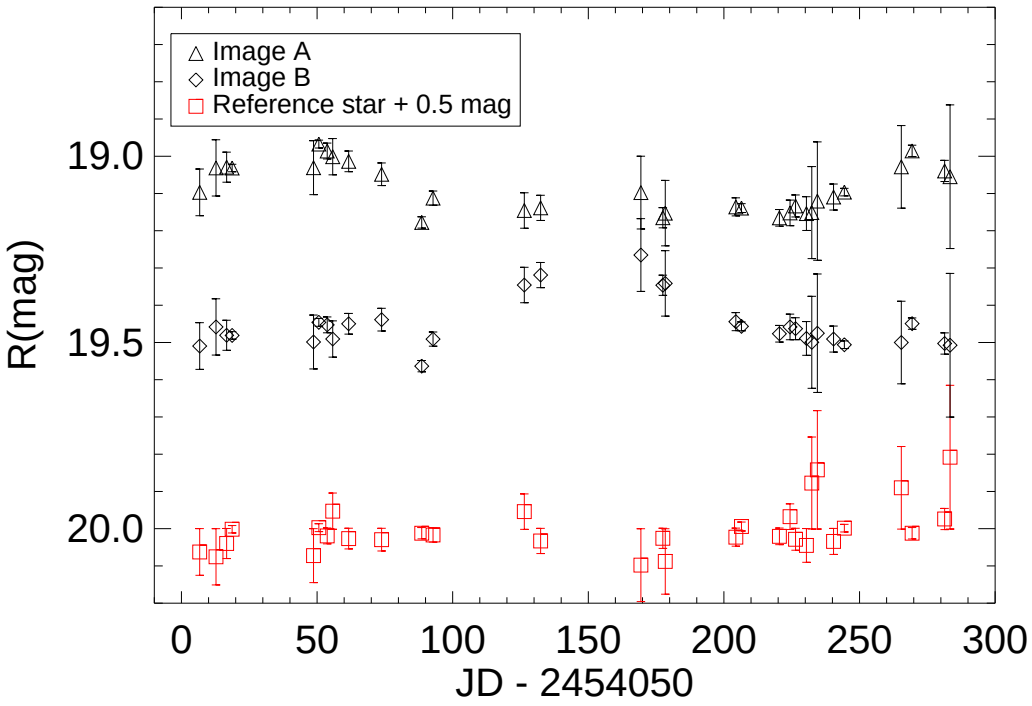

Figure 5.11: *R-band light curves of SDSS J1206+4332. Magnitude variabilities are seen in both light curves A (diamonds) and B (triangles) as bumps. The reference star is plotted with red squares.*

5.6 TIME DELAY OF SDSS J1206+4332

From the geometry of the system SDSS J1206+4332 (see Figure 5.6) we anticipate that the A image is a leading since it is farther from the center of the main lensing galaxy. Thus, we predict that any intrinsic quasar variabilities should appear first in the A image. From the mass modeling we know also that the time delay for this system is $\geq$50 days (see Section 8). We apply these constraints when measuring the time delay from the light curves.

The simplest form of such a measurement is visual shifting. Knowing that the variability has to appear first in the image A and then at least 50 days later in the image B we can associate the bump at the beginning of the A light curve centered at $\sim$50 days with the bump in the B light curve centered at $\sim$150 days.

A more quantitative measurement of a time delay is obtained by polynomial fitting. We fitted 7th order polynomials to both light curves using minimum χ^2. In Figure 5.12 we show the two polynomials (solid lines). We have marked in red the parts of the polynomials which were used for calculating the time delay. In order to calculate the time delay we have shifted the A polynomial in time and magnitude to fit it to the B data points and the B polynomial was shifted in time and magnitude to fit it to A data points. For each shift of the polynomials the goodness of fit was calculated. The results of these fits are presented in Figure 5.13. For the magnitude shift, $B - A = 0.31$ mag average of the two time delay estimations is 116^{+6}_{-7} days, where errors are added in squares uncertainties of the two values of the time delay corresponding to 99% confidence level. Based on our modeling (G1 – SIE and G3 – SIS) and using the measured time delay ($\Delta\tau = 116^{+6}_{-7}$ days) we find a Hubble constant of 73^{+3}_{-4} $\mathrm{km\ s^{-1}\ Mpc^{-1}}$.

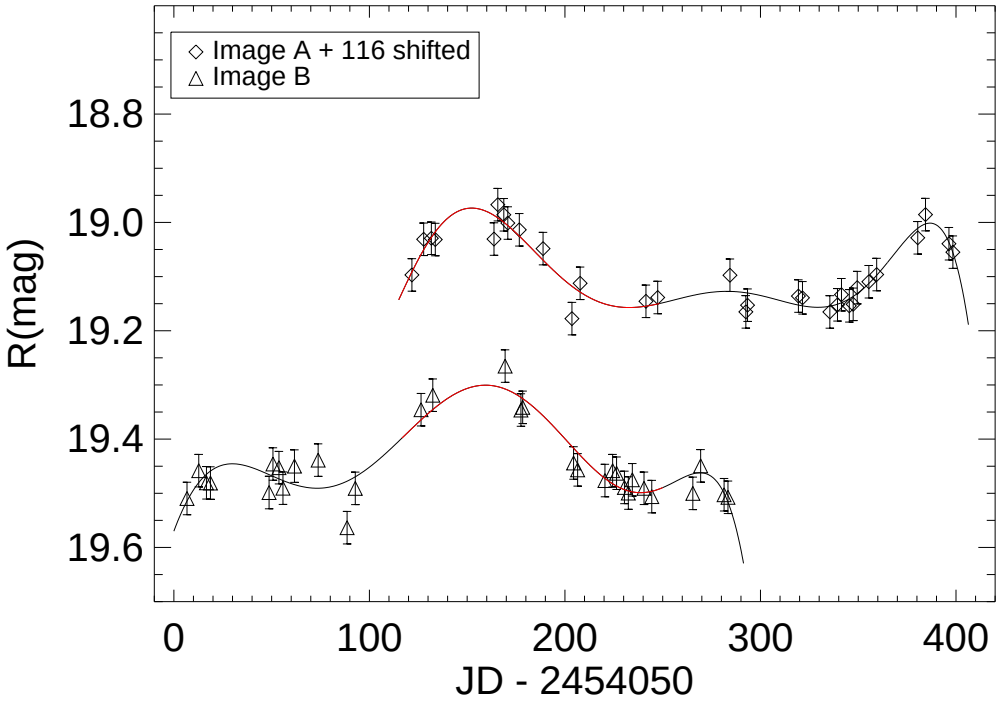

Figure 5.12: *R-band light curves of SDSS J1206+4332. Magnitude variabilities are seen in both light curves A (diamonds) and B (triangles) as bumps. The A light curve is shifted in time by 116 days. The red line indicates the intervals used for cross correlation.*

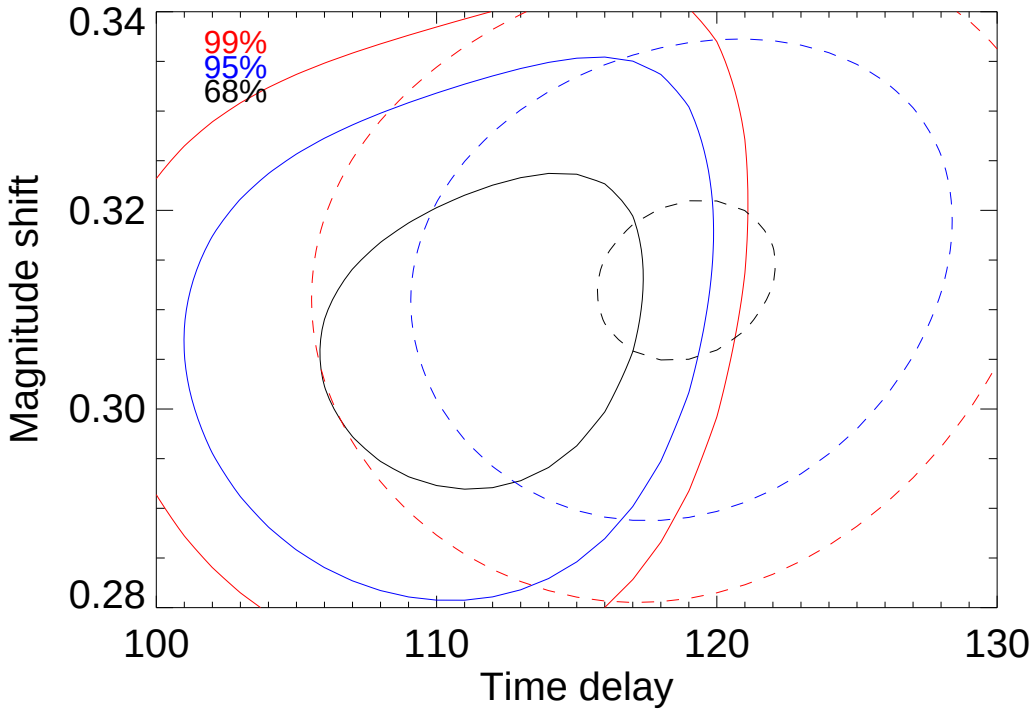

Figure 5.13: *Results of two cross correlation between data on one image and fitted polynomial fitted to light curve of second image. Solid lines represents cross correlation between A data and polynomial fitted to B data, dashed lines are representing cross correlation between B data and polynomial fitted to A data.*

5.7 MICROLENSING

Chang & Refsdal (1979) predicted that in lensed quasar systems the light path should be affected by stars in the lensing galaxy. Moving compact objects in the lensing galaxy can cause spectral changes, brightness variability and, in the case of multiple images, flux-ratio anomalies in the lensed quasar.

The images of a lensed quasar may vary due to intrinsic quasar brightness changes and/or microlensing. Microlensing affects the light paths of each image differently (in the simplest case only one path is affected) whereas the intrinsic variations show up in all the images but at different times due to the time delay. Therefore, one can isolate the microlensing signal by simply calculating the difference between two light curves.

If we shift one of the light curves in magnitude (by the magnitude difference between light curves) and in time (by the time delay) and subtract it from the other quasar counterpart light curve the remaining variation in the light curve difference should not belong intrinsically to the quasar but rather to microlensing.

Our previous study Paraficz et al. (2006) showed that microlensing variabiliy can be detected in this way. The monitoring program presented in this paper was designed to be sensitive to such microlensing signals. The only limitation are S/N and gaps in the light curve due to bad weather conditions. In Figures (5.14–5.18) we present the result of a microlensing variability analysis for our observed targets.

The top plots present the quasar images lightcurves, with one of the images being shifted in time (by the theoretically predicted or, if available, the measured time delay) and in magnitude (by average magnitude difference between the images). The lower panels show the light curves difference. The difference is calculated between a linearly interpolated B light curve and the A data points. In Figures 5.14–5.18 we see that there is no signal stronger than 0.1 mag which is $\sim$ 2 σ. We therefore conclude that we did not detect any significant microlensing event in any of the systems during our monitoring program.

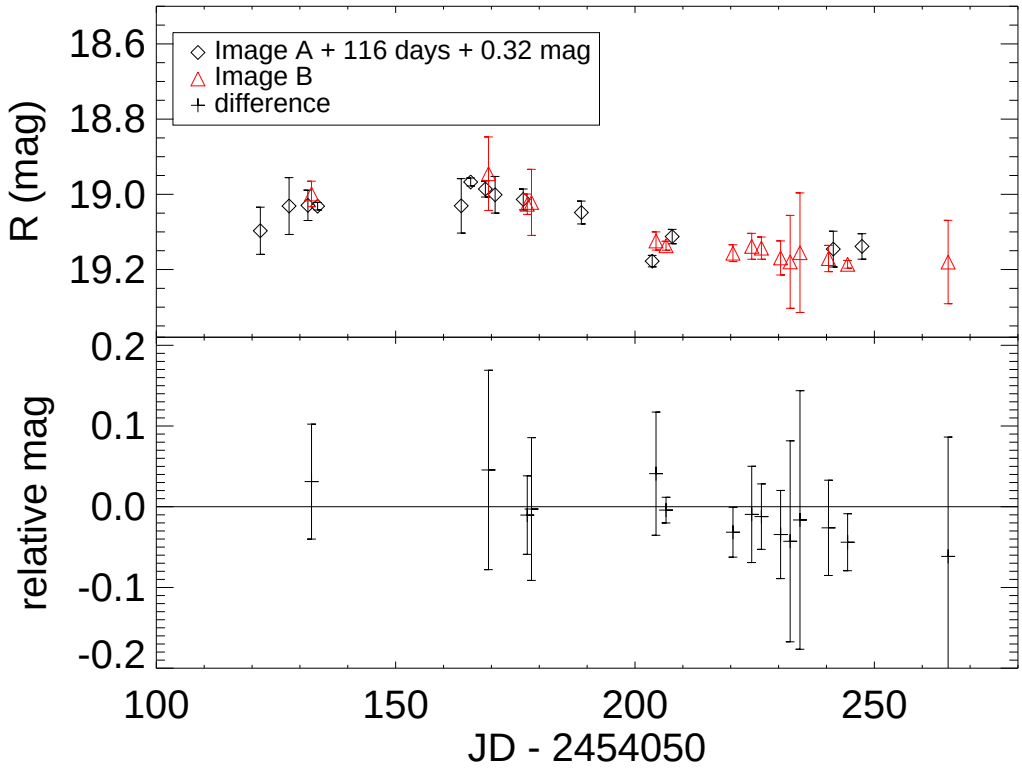

Figure 5.14: *Microlensing of the SDSS J1206+4332.* ***Top:*** *Time-delay shifted light curves, with the A image offset by* 0.32 *mag and* 116 *days.* ***Bottom:*** *Difference between linearly interpolated A image and B image.*

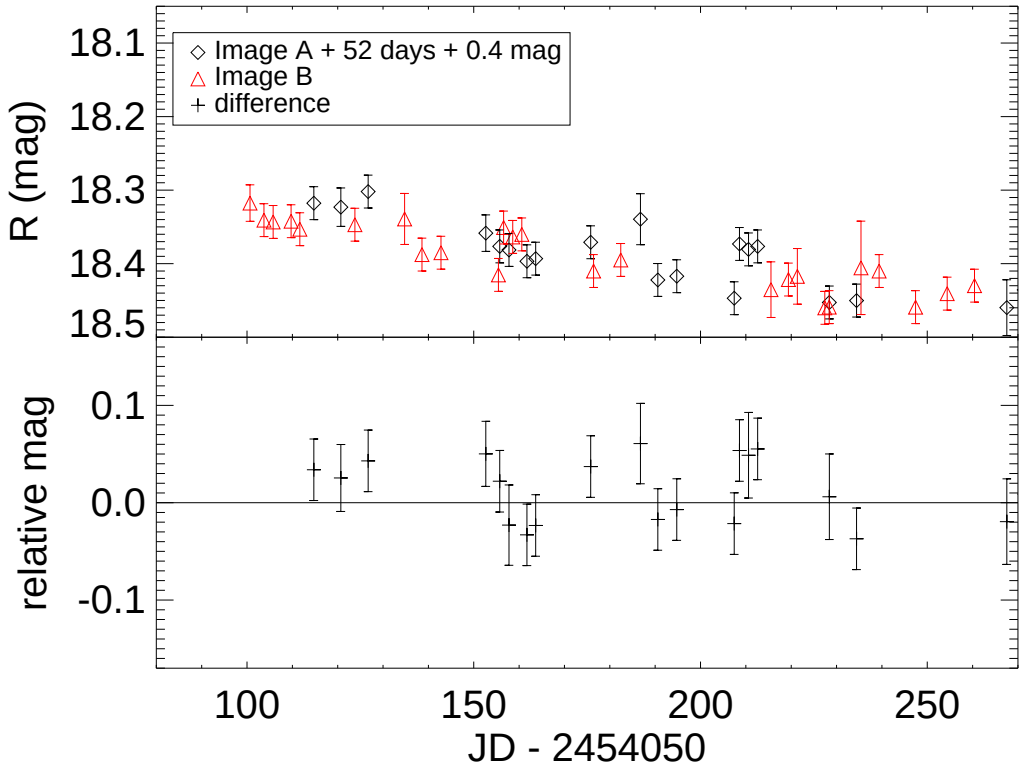

Figure 5.15: *Microlensing of the SDSS J1001+5027.* ***Top:*** *Time-delay shifted light curves, with the A image offset by* 0.4 *mag and* 52 *days.* ***Bottom:*** *Difference between linearly interpolated A image and B image.*

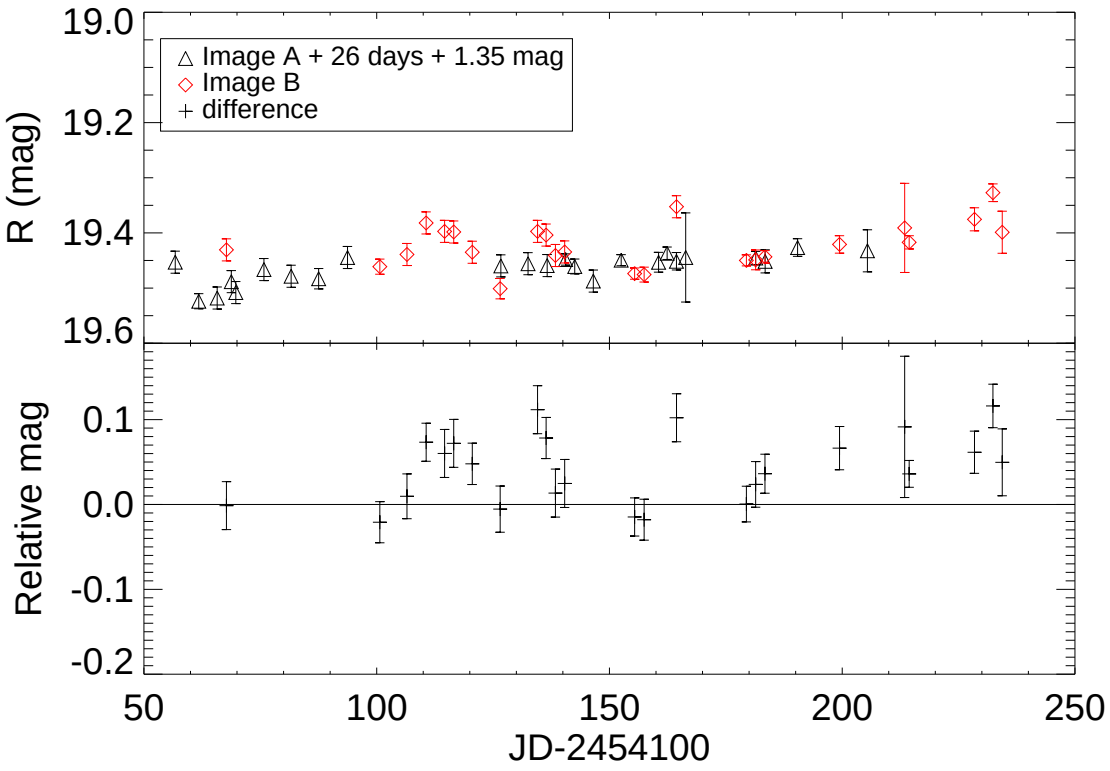

Figure 5.16: *Microlensing of the SDSS J1335+0118.* ***Top:*** *Time-delay shifted light curves, with the A image offset by* 1.35 *mag and* 26 *days.* ***Bottom:*** *Difference between linearly interpolated A image and B image.*

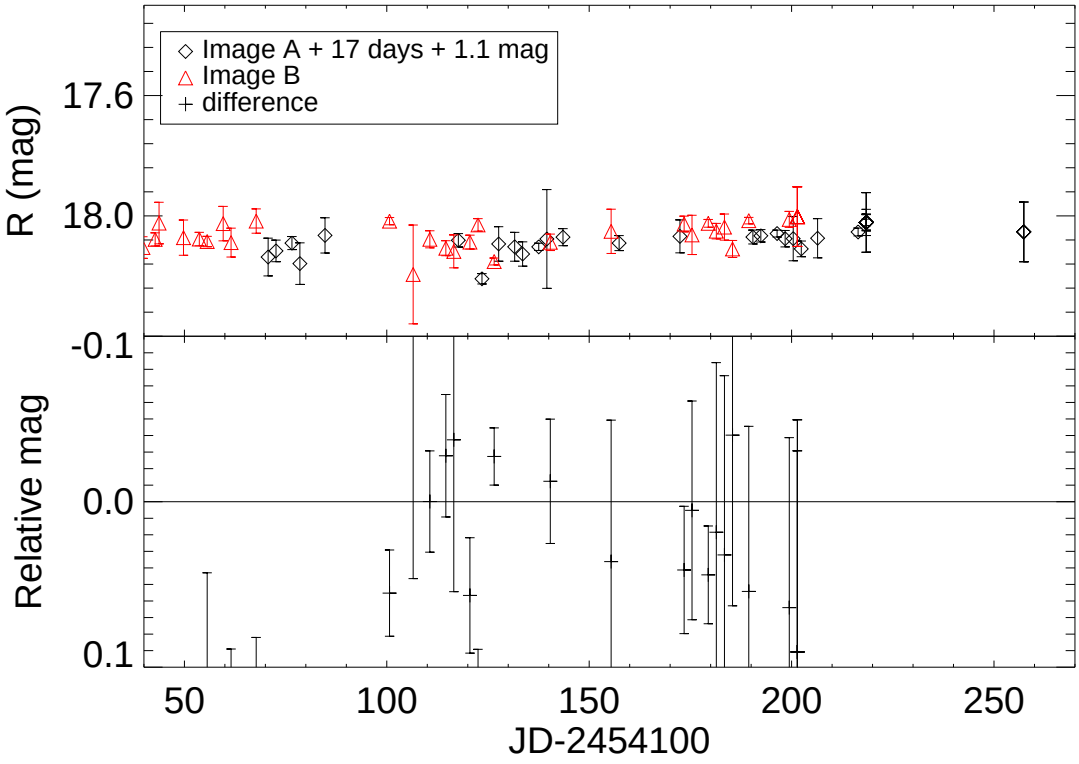

Figure 5.17: *Microlensing of the SDSS J1353+1138.* ***Top:*** *Time-delay shifted light curves, with the A image offset by* 1.1 *mag and* 17 *days.* ***Bottom:*** *Difference between linearly interpolated A image and B image.*

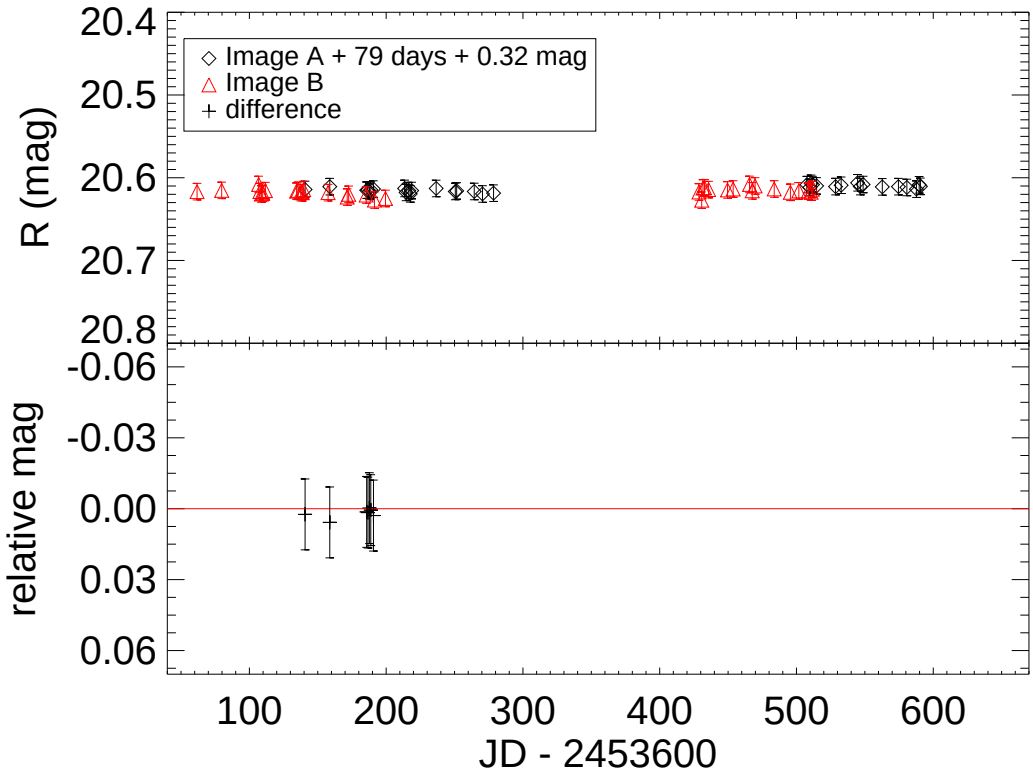

Figure 5.18: *Microlensing of the SDSS J0903+5028.* ***Top:*** *Time-delay shifted light curves, with the A image offset by* 0.32 *mag and* 79 *days.* ***Bottom:*** *Difference between linearly interpolated A image and B image.*

5.8 MODELING

5.8.1 ANALYTICAL MODELING

In principle, one can calculate the Hubble constant from the time delay of a gravitationally lensed system, but there is one major obstacle, namely the mass-sheet degeneracy Falco et al. (1985). This degeneracy is between the Hubble constant and the radial density profiles of the lens Wucknitz & Refsdal (2001) and its angular structure Freedman et al. (2001). Summarizing, different mass profiles give different results on the Hubble constant without changing the lensing configuration. To break this degeneracy we need to have information about the mass profile, e.g., through the velocity dispersion Romanowsky & Kochanek (1999). For our systems we do not know which lens model is the correct one, but fortunately in many cases a lens can be quite well modeled using a fairly simple mass model like SIE (Singular Isothermal Ellipsoid) Kormann et al. (1994) or NFW (Navarro-Frank-White) Golse & Kneib (2002).

In this paper, for the analytical modeling, we have modeled all our systems using singular isothermal potentials. We used those models because of their simplicity and because they agree with physical properties of many observed lenses Kochanek (1993), Rusin et al. (2003), Koopmans et al. (2006*a*).

In the analytical modeling we have the positions of the two images as constraints and as free parameters we have the lens velocity dispersion, σ_0 and the ellipticity, ϵ. We also have two fixed parameters, the position angle, θ_ϵ and the position of the lens galaxy. The number of degrees of freedom is 0, thus we can look for the one model which perfectly fits the data. The positions of the images and lens are visible on the decovolved images (see Figure 5.6). The position angle of the lenses can be roughly estimated from analysis of the deconvoled images, as the mass profile of a lens tends to align to its visible component (Keeton et al. 1998). We allow this constraint to vary within 45°. We have not used flux ratios as constraints because of the possible influence of reddening by dust (Elíasdóttir et al. 2006), microlensing (Paraficz et al. 2006) or small-scale structure in the lens potential (Dalal & Kochanek 2002).

The ellipticity used here is defined as $\epsilon = (a^2 - b^2)/(a^2 + b^2)$, where a and b are the major and minor axis. The position angle corresponds to the direction of the semi-major axis of the isopotential counted east of north. The modeling has been performed using the LENSTOOL software package available at http://www.oamp.fr/cosmology/lenstool/ (Jullo et al. 2007). LENSTOOL is a software created for modelling strong lensing systems with parametric methods which chooses models using the Bayesian evidence. In all models we set the Hubble constant to be $H_0 = 73\ \mathrm{km\ s^{-1}\ Mpc^{-1}}$.

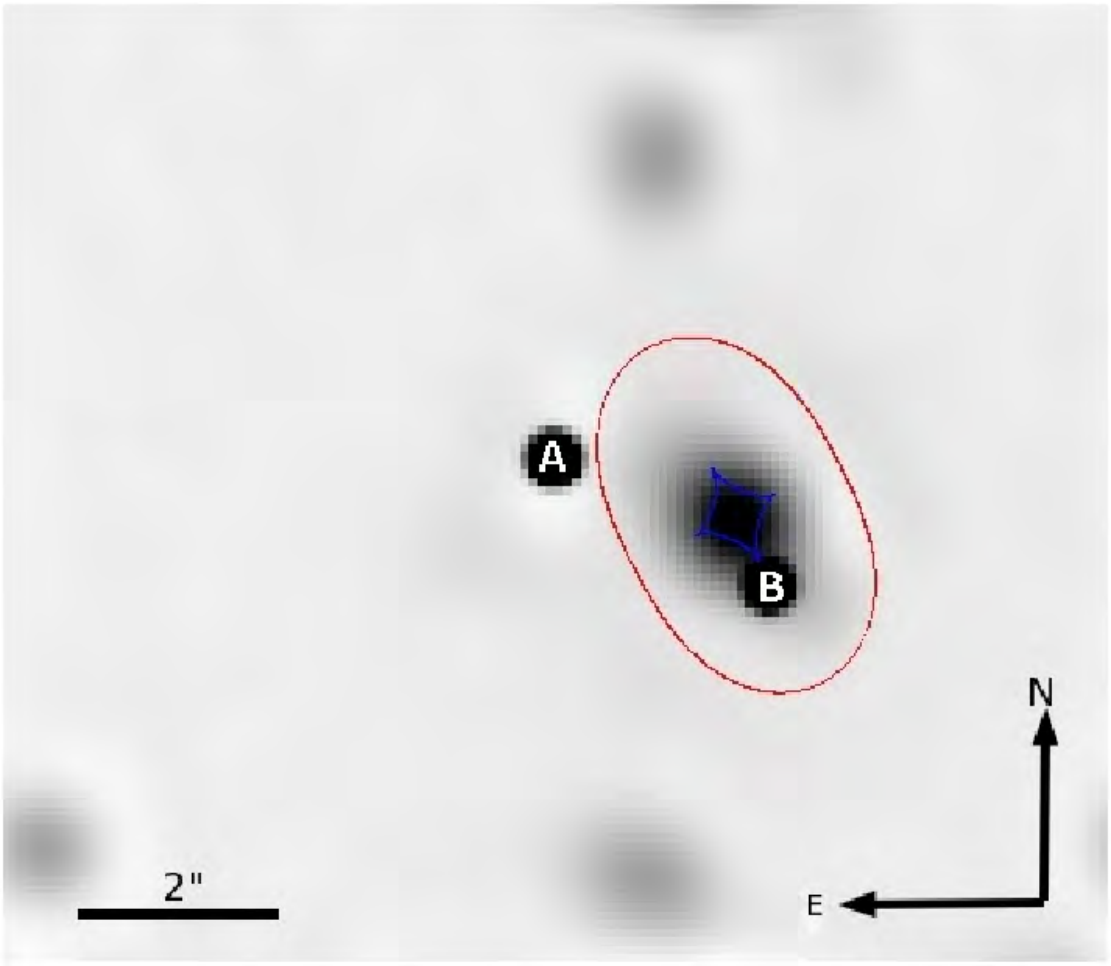

Figure 5.19: *Lens model of SDSS J0903+5028. The figure shows an image of the system with over-plotted results of lens modeling. Blue and red lines represent critical and caustic lines, respectively.*

SDSS J0903+5028

We have fitted the two simple models, SIS (Singular Isothermal Sphere) and SIE (Singular Isothermal Ellipsoid) to the lensing galaxy of SDSS J0903+5028. We have assumed that only one galaxy, the central one, influences the quasar light, even though other galaxies are visible to the north and south of the images (see Figure 5.19). The lensing images of the quasar are not collinear with the central galaxy which indicates that there is a quadruple moment in the potential. This moment can come from the tidal effect of the nearby galaxies or may be due to elongation of the central galaxy. Because of the degeneracy we are not able to distinguish which one of the possibilities is true, thus we use one lens, SIE model which accurately predicts image positions. In Table 5.2 we summarize the results of the SDSS J0903+5028 modeling where the central single lens is an SIE. Based on this model, the predicted time delay for the system is 79.4 days. The uncertainty in this value is entirely dominated by systematic modeling uncertainties.

#	Type	x (arcsec)	y (arcsec)	σ_0 ($\mathrm{km\ s^{-1}}$)	ϵ	θ_ϵ	$\Delta\tau$ (days)
G	SIE	1.99	-0.70	264.6	0.49	27°	79.4

Table 5.2: *Lens model of SDSS J0903+5028. Modeled parameters are galaxy position, x, y, lens velocity dispersion, σ_0, ellipticity, ϵ, position angle, θ_ϵ and time delay, $\Delta\tau$.*

SDSS J1001+5027

The lens of SDSS J1001+5027 consists of two galaxies (see Figure 5.6) which according Oguri et al. (2005) are at similar redshifts $0.2 < z < 0.5$. For our modeling we fix both lensing galaxies at redshift 0.3.

We have created two possible models of the lens environment of SDSS J1001+5027. In the first one the system has only one galaxy with elongated SIE mass profile. This model is able to ray-trace the position of the quasar images. From Figure 5.20 we also see that the position angle, P.A. of the model is consistent with the light distribution of the main galaxy but it is also in the direction of the other galaxy. This leads to the conclusion that the quadruple moment might come from the second galaxy rather then from the elongation of the main one. In the second version of the lens model we have set both gravitational lenses as Singular Isothermal Spheres, SIS. This model also reproduces the position of the quasar images and gives a sensible result of the galaxy velocity dispersions being 223 $\mathrm{km\ s^{-1}}$ for main lens (G1) and 159 $\mathrm{km\ s^{-1}}$ for G2. The results from both models are presented in Figure 5.20 and summarized in Table 5.3. The predicted time delay of the system is 34 days based on the SIE model and 52 days based on the double SIS model.

#	Type	x (arcsec)	y (arcsec)	σ_0 ($\mathrm{km\ s^{-1}}$)	ϵ	θ_ϵ	$\Delta\tau$ (days)
G1	SIE	1.749	0.861	258	0.23	11°	52
G1	SIS	1.749	0.861	223	0	···	34
G2	SIS	1.629	−0.588	159	0	···	34

Table 5.3: *Lens model of SDSS J1001+5027. Parameters are as in Table 5.2.*

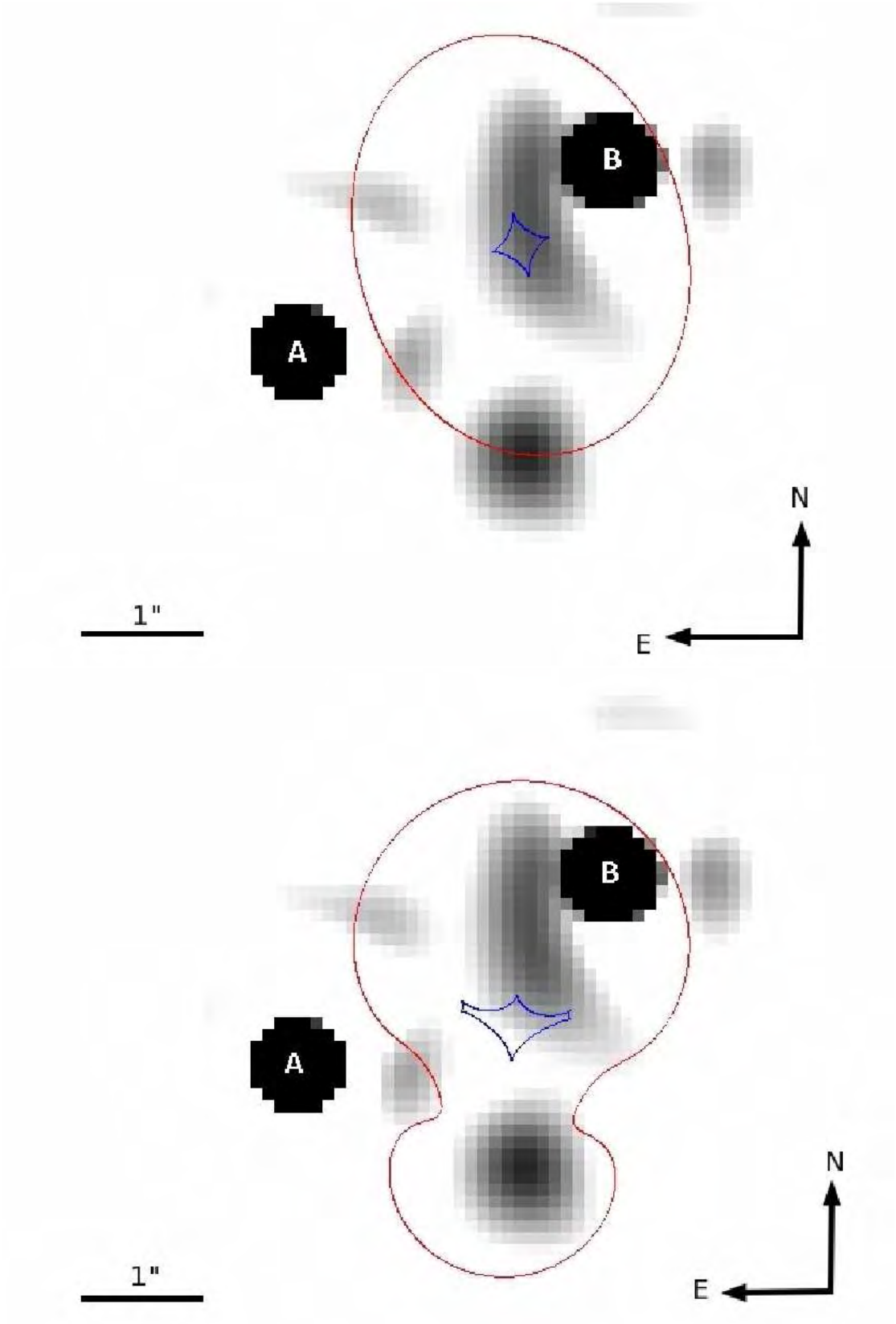

Figure 5.20: *Lens model of SDSS J1001+5027. The figure shows an image of the system with over-plotted results of lens modeling. Blue and red lines represent critical and caustic lines, respectively. Top plot present the single SIE lens model and the bottom plot presents the two SIS lens models.*

SDSS J1206+4332

We have fitted SIS and SIE to the main lensing galaxy of the SDSS J1206+4332. We have assumed that the only galaxy which influences the quasar light is the central galaxy G1 (see Figure 5.6). Unfortunately neither of these mass models gives physically realistic results. The system seems to be more complicated, so presumably the other galaxies seen in vicinity of the system may play a role. A model of the main galaxy G1 (SIE) and G2 (SIS) does not give any physical solutions either, which is expected since the redshift of G2 is predicted to be rather small.

It appears that the third galaxy lying $\sim 3\farcs$ north of the system (see Figure 5.6) has a strong influence on the system geometry. If we assume our model to be two lensing galaxies with one of them being G1 (SIE) and the other G3 (SIS) it is possible to reproduce the positions of the images. The results of that final fitting are summarized in Table 5.4. Based on this model, the predicted time delay of the system is 112.5 days which is in agreement with our measurement of 116^{+6}_{-7} days (see section 6).

#	Type	x (arcsec)	y (arcsec)	σ_0 ($\mathrm{km\ s^{-1}}$)	ϵ	θ_ϵ	$\Delta\tau$ (days)
G1	SIE	-0.66	1.75	347.5	0.1	$-2°$	112.5
G3	SIS	1.32	5.9	279.5	0	$\cdots$	112.5

Table 5.4: *Lens model of SDSS J1206+4332. Parameters are as in Table 5.2*

SDSS J1335+0118

The system has one lensing galaxy, at redshift $z = 0.5$, we have modeled as an SIE. The lensing galaxy is barely visible in our images, hence the position of the galaxy was taken from Oguri et al. (2004). According to observations made by Oguri et al. (2004) with Keck, the lensing galaxy is misaligned with the QSO images which indicates the existence of external shear or elongation of the lensing galaxy. A model with an SIE lens accurately predicts the image position and gives plausible galaxy parameters. The model details are summarized in Table 5.5. The estimated time delay of the system is 26.2 days which is in agreement with previous studies.

#	Type	x (arcsec)	y (arcsec)	σ_0 ($\mathrm{km\ s^{-1}}$)	ϵ	θ_ϵ	$\Delta\tau$ (days)
G	SIE	-0.786	-0.649	218	0.16	$-5°$	26.2

Table 5.5: *Lens model of SDSS J1335+0118. Parameters are as in Table 5.2*

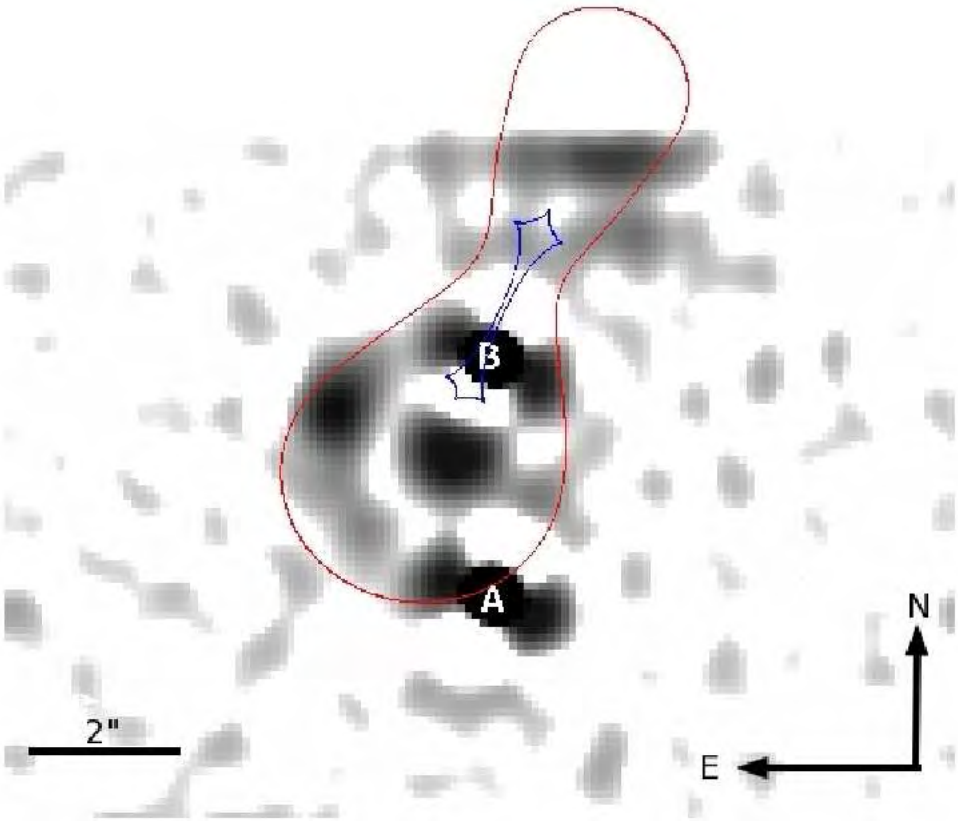

Figure 5.21: *Lens model of SDSS J1206+4332. The figure shows an image of the system with over-plotted results of lens modeling. Blue and red lines represent critical and caustic lines respectively.*

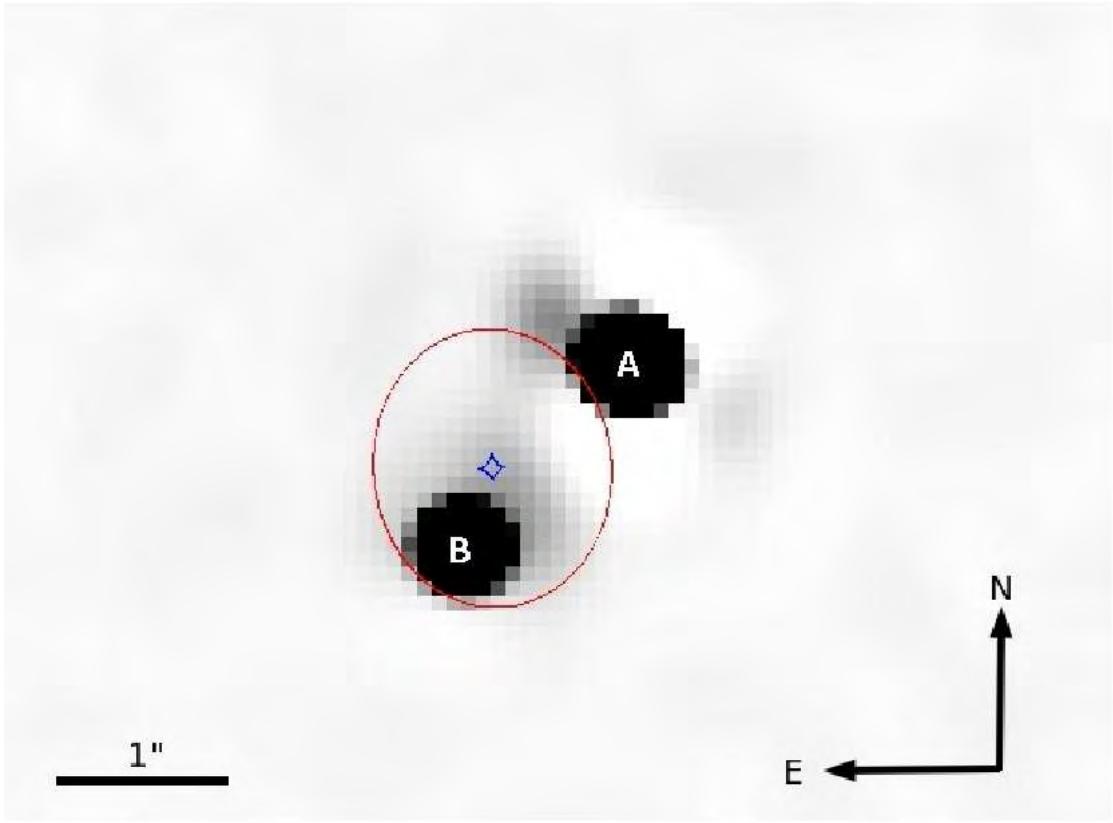

Figure 5.22: *Mass model of SDSS J1335+0118. Figure shows an image of the system with over-plotted results of lens modeling. Blue and red lines represent critical and caustic lines, respectively.*

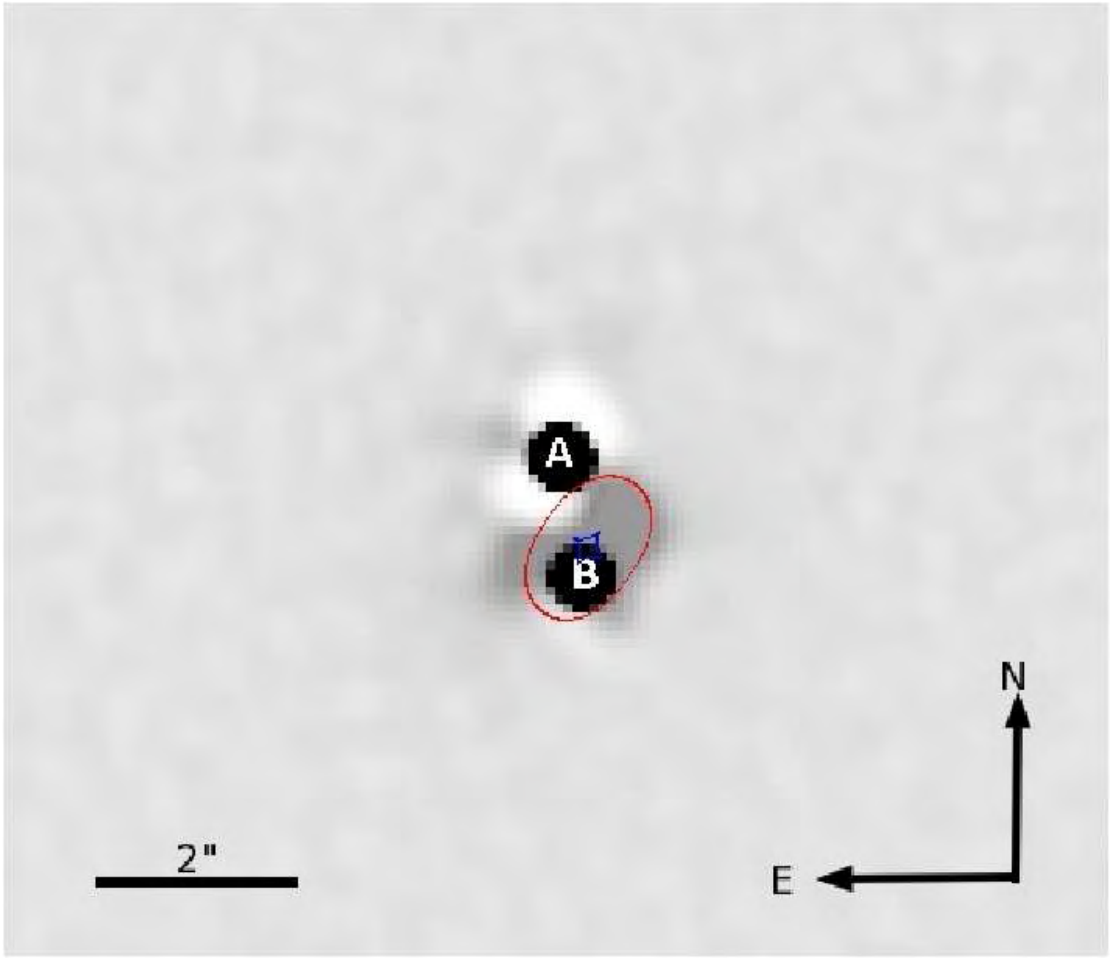

Figure 5.23: *Mass model of SDSS J1353+1138. Figure shows an image of the system with over-plotted results of lens modeling. Blue and red lines represent critical and caustic lines, respectively.*

SDSS J1353+1138

SDSS J1353+1138 has a centrally aligned lensing galaxy and the B image very close to the galaxy centre. There are no other close-by galaxies; thus the lens can be modeled with a simple SIE. The predicted time delay for that system is 17 days (see Table 5.6) which is in agreement with previous studies.

#	Type	x (arcsec)	y (arcsec)	σ_0 ($\mathrm{km\,s^{-1}}$)	ϵ	θ_ϵ	$\Delta\tau$ (days)
G	SIE	-0.25	-1.04	177	0.46	35°	17.2

Table 5.6: *Lens model of SDSS J1353+1138. Parameters are as in Table 5.2*

5.8.2 NON-PARAMETRIC MODELING

We have also modeled our systems based on a non-parametric method proposed by Saha & Williams (1997) using the publicly available code PixeLens Saha & Williams (2004).

PixeLens reconstructs a pixelated mass map of the lens by implementing Bayesian statistics, it generates numerous lens models which fit to the lens system geometry. There are two major advantages of using this method. First, it allows to explore a wide range of models not restricted with parameters, which circumvents the non-uniqueness problem of lens modeling. Second, it gives the systematic error estimation on the modeled time delay which is not possible to get when using analytical methods. Our purpose of using it is to check the robustness of our time delay estimations, i.e. we want to know whether the two approaches, analytical and pixeleted, give consistent results for the time delays.

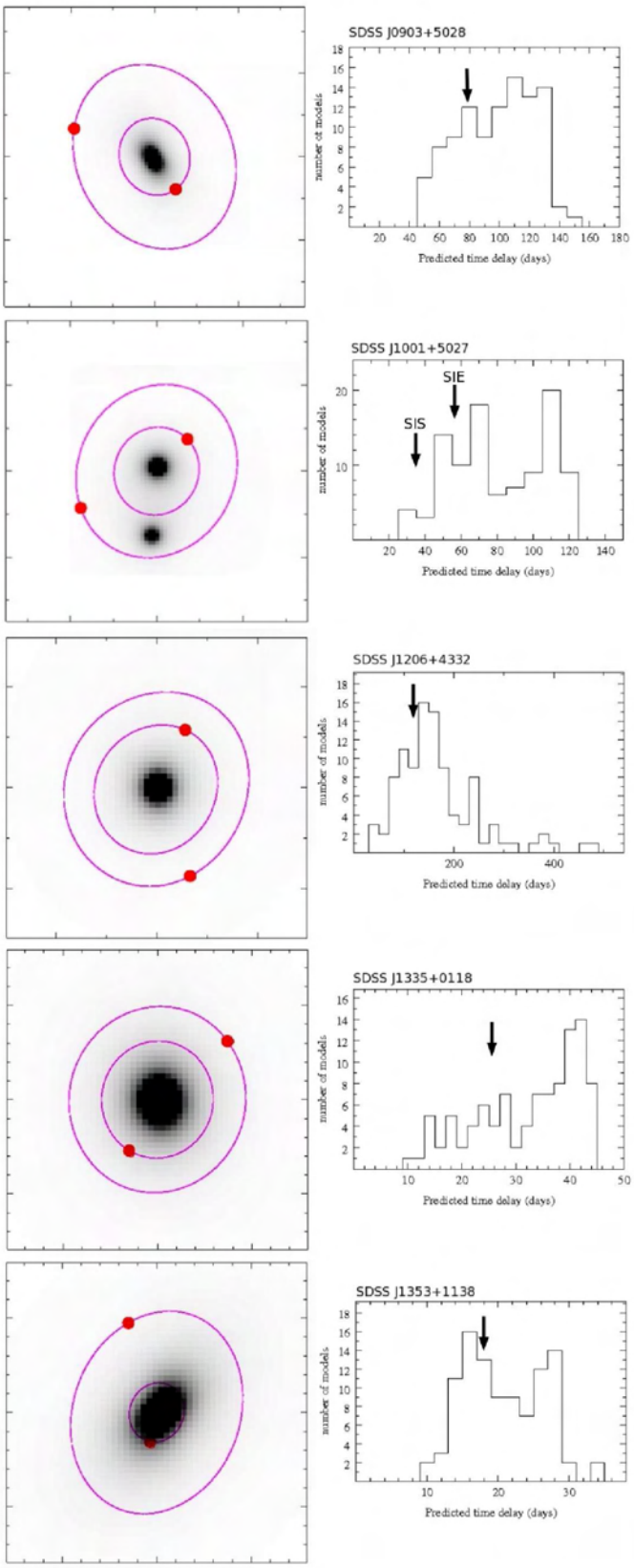

Figure 5.24: *The modeling results of the five lensed quasars. On the left side we see potential contours modeled by PixeLens which are over-plotted on the mass map created in analytical modeling. On the right the are time delay histograms generated for each system by the 300 suitable lens models, arrows indicate the time delays estimated from analytical modeling. We see that the potentials of the PixeLens correspond quite well to the analytical models*

PixeLens generates models which reproduce the exact position of lensing images and aligned within 45° of the visible lens P.A. All our systems were modeled assuming existence of external shear and all of them, except SDSS J1206+4332, were modeled as symmetric. For each system we generated 300 lens models which were used to estimate the average and median time delay and their model uncertainties. The modeling results of the 5 gravitationally lensed QSOs with PixeLens are summarized in Table 5.7. Figure 5.24 shows the potentials and time delays of the 5 systems modeled with pixelated method. On the left side we see potential contours modeled by PixeLens which are over-plotted on the mass map created in analytical modeling. On the right are histograms of the time delays generated for each system by the 300 lens models.

We see that the lens potentials of the PixeLens correspond to the analytical models and from the Table 5.7 we see that the estimated time delay values from analytical modeling lie within error bars of the PixeLens time delays. This is reassuring and gives confidence in our approach. We note also that the analytically obtained time delays are systematically lower than the average values obtained using PixeLens by 20–50%.

#	Analytical (days)	PixeLens (average) (days)	PixeLens (median) (days)
0903+5028	79.4	98±21	101^{+9}_{-12}
1001+5027	52	81±23	76^{+14}_{-9}
1206+4332	113	173±64	152^{+41}_{-21}
1335+0118	26	32±8	35^{+2}_{-6}
1353+1138	17	21±5	20^{+3}_{-2}

Table 5.7: *Modeled time delays of the five lensed quasars.*

5.9 SIMULTANOUS MODELING

The Hubble constant estimated from time delay measurements is model dependent, as illustrated above. Different models give a different Hubble constant and measuring the time delay with high precision does not resolve that issue. One way of dealing with this problem is to generate a large number of models of many lenses and create a distribution of possible values for the Hubble constant based on these models. Thus, we use the pixelated method for several gravitationally lensed systems constraining them to have the same shared value of H_0. Simultaneous modeling has been done in the past by e.g. Saha et al. (2006) – with 10 lenses and Coles (2008) – with 11 lenses.

Figure 5.25 shows the result of the simultaneous modeling of 5 systems with time delays obtained at the NOT, these are RX J0911+055 Hjorth et al. (2002), SBS B1520+530, Burud, Hjorth, Courbin, Cohen, Magain, Jaunsen, Kaas, Faure & Letawe (2002*a*), B1600+434 Burud et al. (2000) and J0951+263 Jakobsson et al. (2005*b*) and the time delay of SDSS J1206+4332 reported in this paper. On the histogram the results of our simultaneous modeling of the 5 QSOs are presented, for each object 100 lens models were created. The Hubble constant estimated using this method is $H_0 = 61.5^{+8}_{-4}\,\mathrm{km\,s^{-1}\,Mpc^{-1}}$.

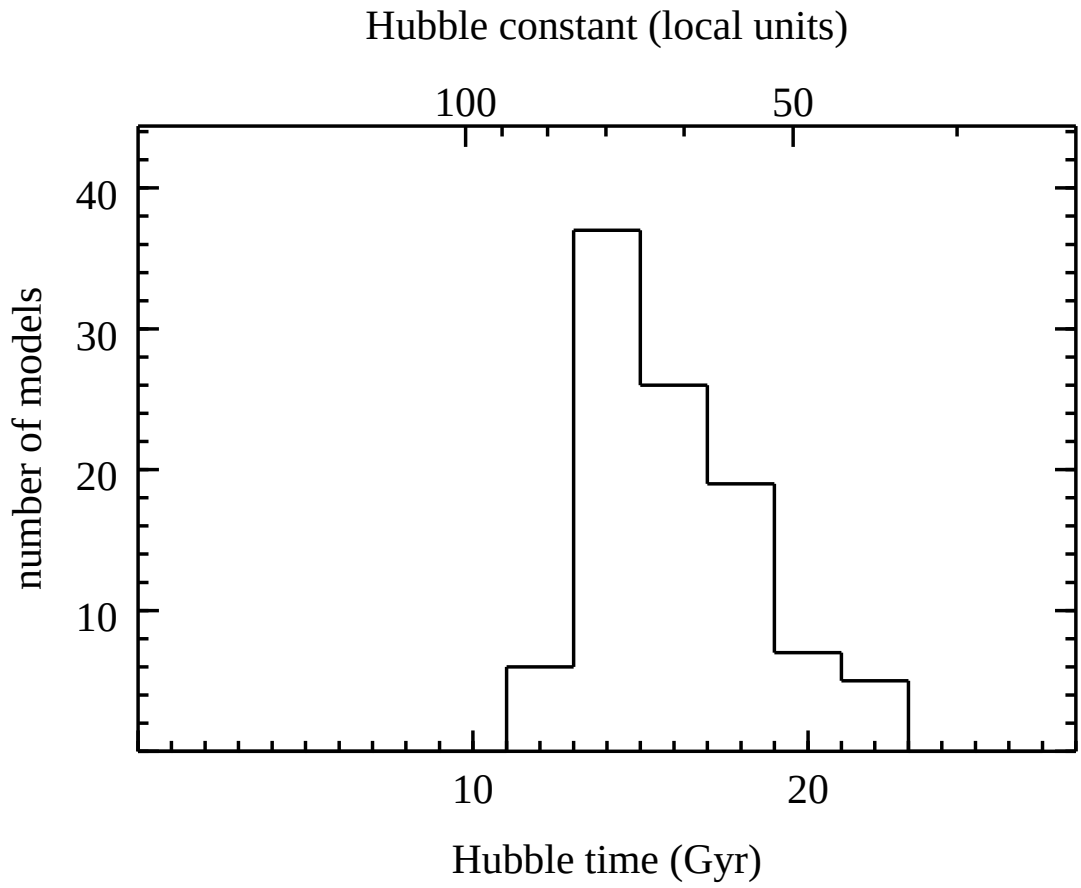

Figure 5.25: *The result of the simultaneous modeling, it is a histogram created from the modeling of the 5 QSOs for each of them 100 lens models were created, the Hubble constant estimated using this method is* $H_0 = 61.5^{+8}_{-4}$ $\mathrm{km\,s^{-1}\,Mpc^{-1}}$.

5.10 DISCUSSION

We have estimated the time delay of the SDSS J1206+4332 to be $\Delta\tau = 116^{+6}_{-7}$ based on a 280-day long monitoring campaign at the Nordic Optical Telescope. This shows the feasibility of measuring time delays from campaigns not much longer than the time delay itself. To model the system, we first assumed a single lensing galaxy modeled with the Singular Isothermal Ellipsoid (SIE), but were unable to reproduce the image positions. By adding to the lens model the G2 and G3 galaxies we found that the influence of the G2 galaxy is negligible due to its small redshift but the G3 galaxy has a major impact on the system's geometry. A lens model with two galaxies, where the main one is a SIE and the second is a SIS, predicts the image positions very well. Thus this model resulted in a Hubble constant of $73^{+3}_{-4}\ \mathrm{km\ s^{-1}\ Mpc^{-1}}$ assuming $\Omega_{\mathrm{m}} = 0.3$ and $\Omega_{\Lambda} = 0.7$.

Lack of short-term variability in the other monitored systems (SDSSJ 0903, SDSS J1001+5027, SDSS J1353+1138, SDSS J1335+0118) meant that we did not succeed in measuring their time delays. From the quasar studies of Fohlmeister et al. (2008), Vuissoz et al. (2007), Koopmans et al. (2000) and many others we see that during the 200–300 days of a quasar monitoring a quasar might be at the quiet stage or at the slow increase or decrease. Thus, despite our success in measuring the time delay of SDSS J1206+4332, it appears that monitoring substantially longer than the predicted time delay of a given system will be unavoidable in most cases.

We have modeled all five systems using both analytical and pixelated methods. Using the predicted time delays we have shown that none of the systems exhibited significant microlensing variability for the observing campaign.

We have also performed simultaneous pixelated modeling with a shared Hubble constant of five lenses which time delays were measured at the NOT. The estimated Hubble constant from this analysis is $H_0 = 61.5^{+8}_{-4}\ \mathrm{km\ s^{-1}\ Mpc^{-1}}$.

Acknowledgments The Dark Cosmology Centre is funded by the DNRF. DP acknowledges receipt of a research studentship at the Nordic Optical Telescope. Á.E. acknowledges the support of the EU under a Marie Curie International Outgoing Fellowship, contract PIOF-GA-2008-220049. DP thanks Andreas Jaunsen for his contribution in the definition phase of the project, Jin Hyeok An and Andrea Morandi for useful comments, Páll Jakobsson for extensive help with MCS deconvolution. Also, we would like to thank all visiting observers at the NOT who obtained data on our behalf. The data used are based on observations made with the Nordic Optical Telescope, operated on the island of La Palma jointly by Denmark, Finland, Iceland, Norway, and Sweden, in the Spanish Observatorio del Roque de los Muchachos of the Instituto de Astrofisica de Canarias.

6

THE HUBBLE CONSTANT INFERRED FROM 18 TIME DELAY LENSES

Danuta Paraficz and Jens Hjorth
2009, ApJ submitted

ABSTRACT –

We present a simultaneous analysis of 18 galaxy lenses with time delay measurements. For each lens we derive mass maps using pixelated simultaneous modeling with shared Hubble constant. We estimate the Hubble constant to be 66^{+6}_{-4} km s^{-1}Mpc^{-1} *(for a flat Universe with* $\Omega_m = 0.3$, $\Omega_\Lambda = 0.7$*). We have also selected a subsample of five relatively isolated early type galaxies and by simultaneous modeling with an additional constraint on isothermality of their mass profiles we get* $H_0 = 76^{+3}_{-3}$ km s^{-1}Mpc^{-1}.

6.1 INTRODUCTION

The Hubble constant is one of the most important parameters in cosmology. It determines the age of universe, the physical distances to objects, constrains the dark energy equation-of-state and furthermore, it is used as a prior in many cosmological analysis. Hence, it is essential for cosmology to know the precise value of H_0 (Riess et al. 2009). The newest measurements give a quite well defined H_0 with estimated errors at the 5-10% level but unfortunately H_0 differs among different cosmological methods and there is only marginal consistency between their 1σ errors (see Table 6.1).

Moreover, those methods are based on different physical principles and more importantly they measure different consequences of H_0. Both SNe and Cepheids measure luminosity distance but at different scales (distant and local Universe respectively). Cepheids can provide a luminosity distance via the period-luminosity relation but only in the local Universe, on the other hand, the significantly brighter SNe with their characteristic peak luminosity can measure cosmological distances but need to be calibrated with Cepheids. The SZ effect, which is based on high energy electrons in a galaxy cluster distorting the CMB through inverse Compton scattering, is proportional to the gas density of the galaxy cluster and that combined with the cluster's X-ray flux gives an estimate of the angular diameter distance. Finally, the angular power spectrum of the CMB gives information about many cosmological parameters which have correlated effects on the power spectrum, especially strong degeneracies are between H_0 and Ω_m and Ω_b. Furthermore, there are significant differences in the obtained results even within one method (eg. SNe Branch et al. (1996), Sandage et al. (2006), Riess et al. (2009), see Table 6.1).

Additionally, any astrophysical approach suffers from systematic uncertainties, e.g., supernovae are not standard but standardized candles with possible redshift evolution, CMB have various parameter degeneracies and interference with foregrounds, and the SZ method is assuming spherical symmetry on often significantly non-spherical clusters of galaxies. It is therefore important to explore complementary methods for measuring H_0. Gravitationally lensed quasars QSOs offer such an attractive alternative.

Table 6.1: *H_0 comparison*

Method	H_0	Author
CMB (3 years)	$73.2^{+3.1}_{-3.2}$	Spergel et al. (2007)
CMB (5 years)	$71.9^{+2.6}_{-2.7}$	Komatsu et al. (2009)
Ia SNa	74.2 ± 3.6	Riess et al. (2009)
Ia SNa	62.3 ± 1.3	Sandage et al. (2006)
SZ	65^{+8}_{-7}	Jones et al. (2005)
Cepheids	72 ± 8	Freedman et al. (2001)

As shown by Refsdal (1964) the Hubble constant can be measured based on the time delay Δt between multiply lensed images of QSOs, because $H_0 \propto 1/\Delta t$, provided that the mass distribution of the lens is known. Time delays measure $\frac{D_{OL}D_{OS}}{D_{LS}}$, where $D_{\rm OL}$, $D_{\rm OS}$, $D_{\rm LS}$ are the angular diameter distances between observer and lens, observer and source, and lens and source, respectively. Gravitational lensing has its degeneracies but it is based on well understood physics and unlike distance ladder methods there are no calibration issues (Branch et al. 1996, Sandage et al. 2006).

Gravitational lensing has, up to now, not been seen as reliable as other leading cosmological

methods. Determination of the Hubble constant using lensing is problematic, because the mass distribution of a lens strongly influences the result of H_0 and unfortunately we never have a complete knowledge of that, hence a choice of a lens model is needed.

Recently, however, time-delay lenses have successfully been used for H_0 estimation. In particular, Oguri (2007) used a Monte Carlo method to combine lenses and derived $H_0 = 70 \pm 6$ $\mathrm{km\ s^{-1}Mpc^{-1}}$. Saha et al. (2006) obtained $H_0 = 72^{+8}_{-11}$ $\mathrm{km\ s^{-1}Mpc^{-1}}$ using a combination of 10 lenses, Coles (2008) got $H_0 = 71^{+6}_{-8}$ $\mathrm{km\ s^{-1}Mpc^{-1}}$ using a combination of 11 lenses, and Suyu et al. (2009) found $H_0 = 69.7^{+4.9}_{-5.0}$ $\mathrm{km\ s^{-1}Mpc^{-1}}$ by detailed analysis of one gravitational lens, B1608+656.

This paper extends the work of Saha et al. (2006) and Coles (2008), where results on H_0 were presented using combined modeling of 10 and 11 lenses, respectively. We have used those systems with refined properties of lenses as a part of our sample and have added new systems that have been discovered and monitored during the past 4 years. We therefore now posses an almost doubled sample of systems with measured time delay, which demonstrates that, gravitational lensing is valuable method for H_0 estimation.

6.2 PIXELATED MODELING

Two different approaches for modeling lenses are commonly used. The first one, the non-parametric (pixelated) method, generates a large number of models which perfectly fit the data, each of them giving a different result which can then be averaged. For the second method, model fitting, one assumes parametrized models of the mass distribution of the lens.

Pixelated modeling has the advantage of allowing the lens shape and profile to vary freely. It does not presume any parameters and can provide models that would not be possible to reproduce with parametric modeling. Using this approach to a combined analysis of a large sample of lenses is a powerful solution to the modeling problem in gravitational lensing.

In this paper we use the non-analytical method created by Saha & Williams (2004) - PixeLens. PixeLens generates an ensemble of lens models that fit the input data. Each model consists of a set of discrete mass points, the position of the source and optionally, if the time delays are known, H_0. The time delay $\Delta\tau$ is the combined effect of the difference in length of the optical path between two images and the gravitational time dilation of two light rays passing through different parts of the lens potential well,

$$\Delta\tau = \frac{1+z_{\mathrm{L}}}{c}\frac{D_{\mathrm{OS}}D_{\mathrm{OL}}}{D_{\mathrm{LS}}}\left(\frac{1}{2}(\vec{\theta}-\vec{\beta})^2 - \Psi(\vec{\theta})\right). \tag{6.1}$$

Here $\vec{\theta}$ and $\vec{\beta}$ are the positions of the images and the source respectively, z_{L} is the lens redshift, and Ψ is the effective gravitational potential of the lens.

The arrival time at position $\vec{\theta}$ is defined in PixeLens, as a modeled surface,

$$\tau(\vec{\theta}) = \frac{1}{2}|\vec{\theta}|^2 - \vec{\theta}\cdot\vec{\beta} - \int \ln|\vec{\theta}-\vec{\theta'}|\kappa(\vec{\theta'})d^2\vec{\theta'}, \tag{6.2}$$

where κ is surface mass density.

The errors of the positions of observed images and redshifts of source and lens are of the order of a few percent, thus can be ignored. The main source of errors in the data comes from time delays between images.

We have used PixeLens to generate a set of 100 models for a sample of lensing systems (see §3). PixeLens produces an ensemble of models with varying H_0, each consisting of sets of mass

pixels, which exactly reproduce the input data. Moreover, it also models several lenses simultaneously enforcing shared H_0 for all lenses. The images positions, the source and lens redshifts, and the time delay are assumed to be accurate enough for their errors to be ignored (Saha et al. 2006). PixeLens also imposes secondary constraints on mass maps: non-negative density; smoothness, where the density of a pixel must be no more than twice the average density of its neighbors; the mass profile is required to have 180° rotation symmetry (except if it appears very asymmetric); the shear is allowed within 45° of the chosen direction; circularly averaged mass profile should nowhere be shallower nor steeper than $r^{-\alpha_{min}}$ and $r^{-\alpha_{max}}$ respectively, where α_{min} and α_{max} is defined in PixeLens as the minimum and maximum steepness, those values can be chosen by the user however, the default PixeLens constraint is minimal steepness $\alpha_{min} = 0.5$; and finally, additional lenses as point masses can be constrained. PixeLens does not use flux ratios as constraints because of the possible influence of reddening by dust (Elíasdóttir et al. 2006), microlensing (Paraficz et al. 2006) or small-scale structure in the lens potential (Dalal & Kochanek 2002).

6.3 DATA SET

To date, there are 19 gravitational lens systems with published time delays. Table 6.2 summarizes the information about these 19 systems. We have made an attempt to use all the conclusions previously drawn about their shape, external shear, profile, etc. We have used the newest/best measurement of positions and redshifts of images and lens. Apart from the main lensing galaxies we have also included all the galaxies that might contribute to the lensing. We added them whenever they are visible in the field. These systems are RX J0911+055, HE 1104-181, SBS 1520+530, B1600+434 and B1608+656. All the mass maps of the doubly imaged quasars are required to have 180° rotation symmetry and in case of the quadruply imaged systems we allow the lens to be asymmetric if it has been reported asymmetric, which is the case for: HE 0435-1223, SDSS J1004+4112, RX J1131-1231, B1608+656. A constant external shear is allowed, for the lenses where the morphology shows evidence of external shear or the existence of external shear has been reported, which is the case for HE 0435-1223, RX J0911+055, FBQ J0957+561, SDSS J1004+4112, PG 1115+080, RX J1131-1231, SDSS J1206+4332, B1600+434, SDSS J1650+4251, WFI J2033-4723.

One lens systems has been excluded from our analysis, B1422+231. Raychaudhury et al. (2003) indicated that the time-delay measurements made by Patnaik & Narasimha (2001) are possibly inaccurate. Patnaik & Narasimha (2001) reported $\Delta T_{12} = 7.6 \pm 2.5$ days, whereas Raychaudhury et al. (2003) lens modeling predicts $\Delta T_{12} = 0.4h^{-1}$ days. According to Raychaudhury et al. (2003) this value would not be expected to show up in the Patnaik & Narasimha (2001) data, which sampled every 4 days. We follow the Raychaudhury et al. (2003) prediction also because in our analysis the system gives an unreasonably low Hubble constant $H_0 = 12 \pm 3$ $\mathrm{km\ s^{-1}Mpc^{-1}}$, and we exclude the system in what follows.

Figure 6.4 shows a mosaic of the average mass distributions for the remaining 18 lenses.

6.4 FULL SET RESULTS

Our resulting H_0 distribution is shown in Figure 6.2. We have performed the calculation of 18 systems for a flat Universe with $\Omega_\Lambda = 0.7$, $\Omega_m = 0.3$ and we obtain $H_0 = 66^{+6}_{-4}$ $\mathrm{km\ s^{-1}Mpc^{-1}}$ at 68% confidence and $H_0 = 66^{+8}_{-7}$ $\mathrm{km\ s^{-1}Mpc^{-1}}$ at 90% confidence. We also note that for $\langle z_L \rangle = 0.6$, $\langle z_S \rangle = 1.8$, that are average lens and source redshifts of our sample, the inferred H_0

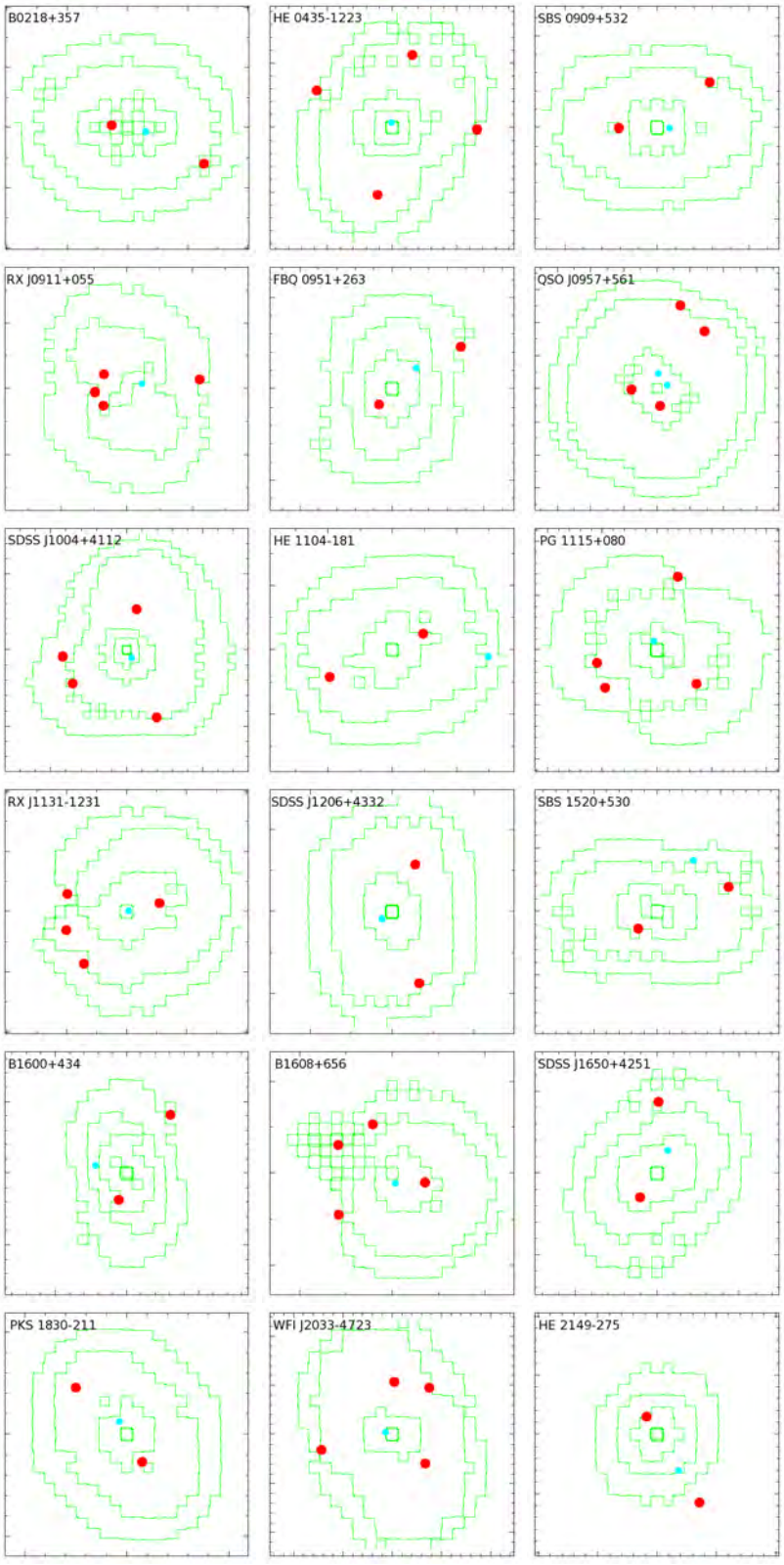

Figure 6.1: *Ensemble of 18 average mass maps of the lenses. The larger tick marks in each panel correspond to* $1''.0$. *Red and cyan dots represent the positions of the images and the sources respectively. The contours are in logarithmic steps, with critical density corresponding to the third contour from the outside.*

System	z_l	z_s	P.A.	Point mass[a]	x[b] ($''$)	y[b] ($''$)	$\Delta\tau$[c] (days)	Reference
PG 1115+080	0.311	1.722	$-45°$	0	0.381	1.344		1, 2, 3, 4
					-0.947	-0.69	$13.3^{+0.9}_{-1.0}$	
					-1.096	-0.232	0	
					0.722	-0.617	$11.7^{+1.5}_{-1.6}$	
HE 2149-275	0.495	2.030	-	0	0.714	-1.150		5, 6, 7
					-0.176	0.296	103 ± 12	
SDSS J1206+4332	0.748	1.789	$50°$	0	0.663	-1.749		8, 9
					0.566	1.146	116^{+4}_{-5}	
HE 0435-1223	0.454	1.689	$-65°$	0	-1.165	0.573		10, 11
					1.311	-0.03	$2.1^{+0.78}_{-0.71}$	
					0.311	1.126	$6^{+1.07}_{-1.08}$	
					-0.226	-1.041	$8.37^{+1.31}_{-1.37}$	
SDSS J1650+4251	0.577	1.547	$80°$	0	0.017	0.872		12, 13
					-0.206	-0.291	49.5 ± 1.9	
QSO J0957+561	0.356	1.410	$-30°$	0	1.408	5.034		14, 15, 16
					0.182	-1.018	422.6 ± 0.6	
					2.860	3.470	0	
					-1.540	-0.050	0	
RX J1131-1231	0.295	0.658	$-35°$	0	-1.984	0.578		17, 3
					-1.426	-1.73	$1.5^{+2.49}_{-2.02}$	
					-2.016	-0.610	$9.61^{+1.97}_{-1.57}$	
					1.096	0.274	87 ± 8	
RX J0911+055	0.769	2.800	$90°$	1	2.226	0.278		18, 19, 20, 21
					-0.968	-0.105	146 ± 8	
					-0.709	-0.507	0	
					-0.696	0.439	0	
SDSS J1004+4112	0.680	1.734	$90°$	0	3.943	-8.868		5, 22, 23, 24
					-8.412	-0.86	821.6 ± 2.1	
					-7.095	-4.389	40.6 ± 1.8	
					1.303	5.327	0	
WFI J2033-4723	0.661	1.660	$0°$	0	-1.439	-0.311		25, 26, 27
					0.756	0.949	35.5 ± 1.4	
					0.044	1.068	0	
					0.674	-0.5891	$27.1^{+4.1}_{-2.3}$	
PKS 1830-211	0.885	2.507	-	0	-0.498	0.456		28, 29, 30, 31
					0.151	-0.268	26^{+4}_{-5}	
B1600+434	0.410	1.590	$90°$	1	0.610	0.814		5, 32, 33, 34
					-0.110	-0.369	51 ± 4	
B0218+357	0.685	0.944	-	0	0.250	-0.119		35, 36, 37, 38
					-0.052	0.007	$10.1^{+1.5}_{-1.6}$	

System	z_l	z_s	P.A.	Point mass[a]	x[b] ($''$)	y[b] ($''$)	$\Delta\tau$[c] (days)	Reference
B1608+656	0.630	1.394	-	1	-1.155	-0.896		39, 40, 41, 42
					-0.419	1.059	31.5 ± 1.5	
					-1.165	0.610	0	
					0.714	-0.197	41 ± 1.5	
HE 1104-181	0.729	2.319	-	2	-1.936	-0.832		43, 44, 45
					0.965	0.5	$152.2^{+2.8}_{-3.0}$	
SBS 1520+530	0.761	1.855	-	1	1.130	0.387		46, 47, 48, 49
					-0.296	-0.265	130 ± 3	
FBQ J0951+263	0.24	1.246	-	0	0.750	0.459		50, 51
					-0.142	-0.169	16 ± 2	
SBS 0909+532	0.830	1.376	-	0	0.572	0.494		5, 52, 53
					-0.415	-0.004	45^{+1}_{-11}	
B1422+231	0.339	3.62	10°	0	1.014	-0.168		54, 55, 3
					0.291	0.900	7.6 ± 2.5	
					0.680	0.580	1.5 ± 1.4	
					-0.271	-0.222	0	

Table 6.2: *Properties of time-delay lenses. (a) We have included all the galaxies that might have contribution in the lensing, we add them whenever one or more galaxies are visible in the field and when their redshift is similar to the main lens. (b)The positions of the QSO images are calculated with respect to the position of the main galaxy G1. The images are in arrival-time order. (c) All measured time delays are listed expect those for which error bars are large and, therefore, the detections are marginal. REFERENCES: (1) Wucknitz et al. (2004); (2) Cohen et al. (2000); (3) Browne et al. (1993); Carilli et al. (1993); (4) Cohen et al. (2003); (5) Kochanek et al. (2006); (6) Morgan et al. (2005); (7) CASTLES; (8) Ullán et al. (2005); (9) Lubin et al. (2000); (10) Burud et al. (1998); (11) Hjorth et al. (2002); (12) Kneib et al. (2000); (13) Bade et al. (1997); (14) Jakobsson et al. (2005a); (15) White et al. (2000); (16) Bernstein & Fischer (1999); (17) Oscoz et al. (2001); (18) Falco et al. (1997); (19) Fohlmeister et al. (2008); (20) Inada et al. (2003); (21) Williams & Saha (2004); (22) Poindexter et al. (2007); (23) Lidman et al. (2000); (24) Wisotzki et al. (1993); (25) Morgan et al. (2008); (26) Barkana (1997); (27) Tonry (1998); (28) Weymann et al. (1980); (29) Claeskens et al. (2006); (30) Paraficz et al. (2009); (31) Oguri et al. (2005); (32) Raychaudhury et al. (2003); (33) Patnaik & Narasimha (2001); (34) Faure et al. (2002); (35) Burud, Hjorth, Courbin, Cohen, Magain, Jaunsen, Kaas, Faure & Letawe (2002b); (36) Auger et al. (2008); (37) Chavushyan et al. (1997); (38) Burud et al. (2000); (39) Jaunsen & Hjorth (1997); (40) Jackson et al. (1995); (41) Koopmans et al. (2003); (42) Fassnacht et al. (2002); (43) Myers et al. (1995); (44) Fassnacht et al. (1996); (45) Morgan et al. (2003); (46) Vuissoz et al. (2007); (47) Meylan et al. (2005); (48) Lovell et al. (1998); (49) Chengalur et al. (1999); (50) Lidman et al. (1999); (51) Vuissoz et al. (2008); (52) Eigenbrod et al. (2006b); (53) Morgan et al. (2004); (54) Burud, Courbin, Magain, Lidman, Hutsemékers, Kneib, Hjorth, Brewer, Pompei, Germany, Pritchard, Jaunsen, Letawe & Meylan (2002); (55) Wisotzki et al. (1996).*

should increase by 2% for an open Universe with $\Omega_\Lambda = 0.0$, $\Omega_m = 0.3$ and decrease by 7% for an Einstein-de Sitter Universe $\Omega_\Lambda = 0.0$, $\Omega_m = 1.0$. Figure 6.3 presents the comparison between estimation from our sample of lenses and samples from previous lensing studies using 15 lenses[1] (Oguri 2007) and 10 lenses (Saha et al. 2006). The H_0 distribution of the samples of 10 and 15 lenses are slightly different than the original results of Oguri (2007) and Saha et al. (2006)[2]. Oguri (2007) used 16 lensed quasar systems (40 image pairs) to constrain the Hubble constant. For each image pair, he computed the likelihood as a function of the Hubble constant. He then computed the effective χ^2 by summing up the logarithm of the likelihoods. The first summation runs over lens systems, whereas the second summation runs over image pairs for each lens system. He derived the best-fit value and its error of Hubble constant in the standard way using a goodness-of-fit parameter.

The difference with Oguri (2007) is mainly due to use of different modeling method and a different statistical and modeling approach to obtain H_0. In the case of Saha et al. (2006) the method is identical and the difference comes from the use of other/newer data, and the use of different rules for constraining shear, adding secondary lenses, etc. Using the Saha et al. (2006) sample of 10 lenses we have obtained $H_0 = 63^{+6}_{-5}$ km s^{-1}Mpc^{-1} and using the Oguri (2007) sample of 16 lenses (minus B1422+231), we got $H_0 = 66^{+5}_{-7}$ km s^{-1}Mpc^{-1}.

[1]Excluding B1422+231.

[2]Oguri (2007) obtained $H_0 = 70 \pm 6$ km s^{-1}Mpc^{-1}, Saha et al. (2006) got $H_0 = 72^{+7}_{-11}$ km s^{-1}Mpc^{-1}

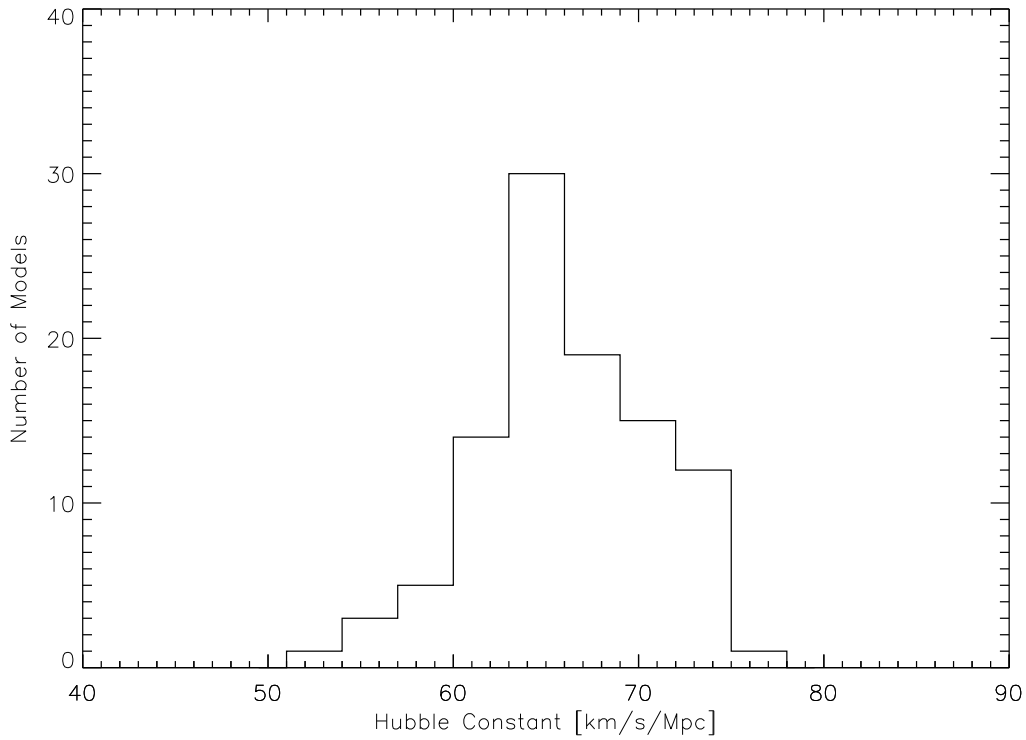

Figure 6.2: *Histogram of the ensembles of H_0 values estimated from 18 lensing systems. We have assumed $\Omega_\Lambda = 0.7$ and $\Omega_m = 0.3$.*

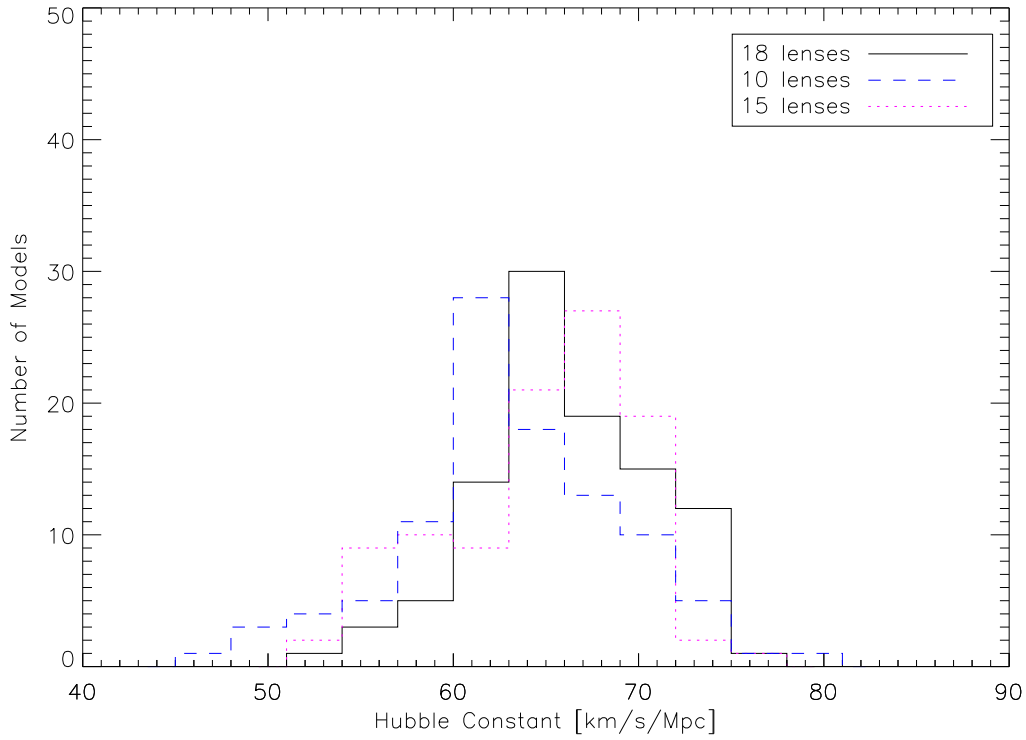

Figure 6.3: *Comparison of the three histograms of the ensembles of H_0 values. Histogram plotted with the solid line represents our results for 18 systems; the dashed line represents the results of 10 lenses (Saha et al. 2006) and the dotted line is a result of 16 lenses (Oguri 2007). All calculations are done for a flat Universe with $\Omega_\Lambda = 0.7$ and $\Omega_m = 0.3$.*

6.5 'ELLIPTICAL' SAMPLE

The strongest degeneracy in lens modeling is the so-called mass-sheat degeneracy between time delays and the steepness of the mass profile. This degeneracy causes that without change in the images position, we can change the steepness of the mass profile, hence, the resulting H_0. Thus, if the steepness and $\Delta\tau$ are known, H_0 is well constrained, although the time delays are also influenced by other more complicated degeneracies involving details of the shape of the lens but these effects are secondary (Saha & Williams 2006).

In our sample of 18 systems we have galaxies with a variety of steepness. Without detailed observations the profile steepness of each lens is not known, except possibly for elliptical galaxies.

Several studies have shown that elliptical galaxies may be considered as approximately isothermal $\rho \propto r^{-2}$ (Koopmans et al. 2006*a*, Oguri 2007, Koopmans et al. 2009, Gerhard et al. 2001). Hence, by selecting from our 18 system only elliptical galaxies we expect to get a uniform sample with known slopes of mass profiles.

We have selected five systems that are relatively isolated, elliptical galaxies: PG 1115+080 (Impey et al. 1998), HE 2149-275 (Lopez et al. 1998), SDSS J1206+4332 (Paraficz et al. 2009), HE 0435-1223 (Kochanek et al. 2006) and SDSS J1650+4251 (Vuissoz et al. 2007, Morgan et al. 2003).

Five other lenses were also found to be elliptical but a cluster or group to which they belong has strong influence on the lensing system, thus it is difficult to model them: QSO 0957+561 (Oscoz et al. 1997, Bernstein & Fischer 1999); RX J1131-1231 (Claeskens et al. 2006); RX J0911+055 (Kneib et al. 2000), SDSS J1004+4112 (Sharon et al. 2005) and WFI J2033-4723 (Eigenbrod et al. 2006*b*),

Three of the lenses are most probably spiral galaxies: PKS 1830-211 is a face-on spiral galaxy (Winn et al. 2002), B1600+434 is a spiral galaxy with a companion (Jaunsen & Hjorth 1997) and B0218+357 is an isolated spiral galaxy (Koopmans & the CLASS collaboration 2001).

The remaining five systems were not included into the 'elliptical' sample due to various other issues: B1608+656 has two lensing galaxies inside the Einstein ring; HE 1104+180 has little starlight, suggesting a dark matter dominated lens (Poindexter et al. 2007, Vuissoz et al. 2008); SBS 1520+530 has a steeper than isothermal slope, probably due to mergers (Auger et al. 2008); FBQ 0951+263 is a complicated system which is hard to model (Peng et al. 2006); SBS 0909+532 is probably early-type (Lehár et al. 2000) but according Motta et al. (2002) is not very typical due to lots of dust.

Using the sample of five elliptical galaxies and constraining the steepness of their mass profiles to be $\alpha_{min} = 1.8$ and $\alpha_{max} = 2.2$ we have run the PixeLens simultaneous modeling. The sample of 5 lensing systems gives us a Hubble constant estimation $H_0 = 79^{+2}_{-3}$ km s^{-1}Mpc^{-1} at 68% confidence and $H_0 = 79^{+3}_{-4}$ km s^{-1}Mpc^{-1} at 90% confidence. We have also combined the 5 constrained systems with the rest of the unconstrained sample to perform simultaneous modeling and obtained very well determined Hubble constant $H_0 = 76 \pm 3$ km s^{-1}Mpc^{-1} at 68% confidence and $H_0 = 76 \pm 5$ km s^{-1}Mpc^{-1} at 90% confidence. The results are presented in Figure 6.4.

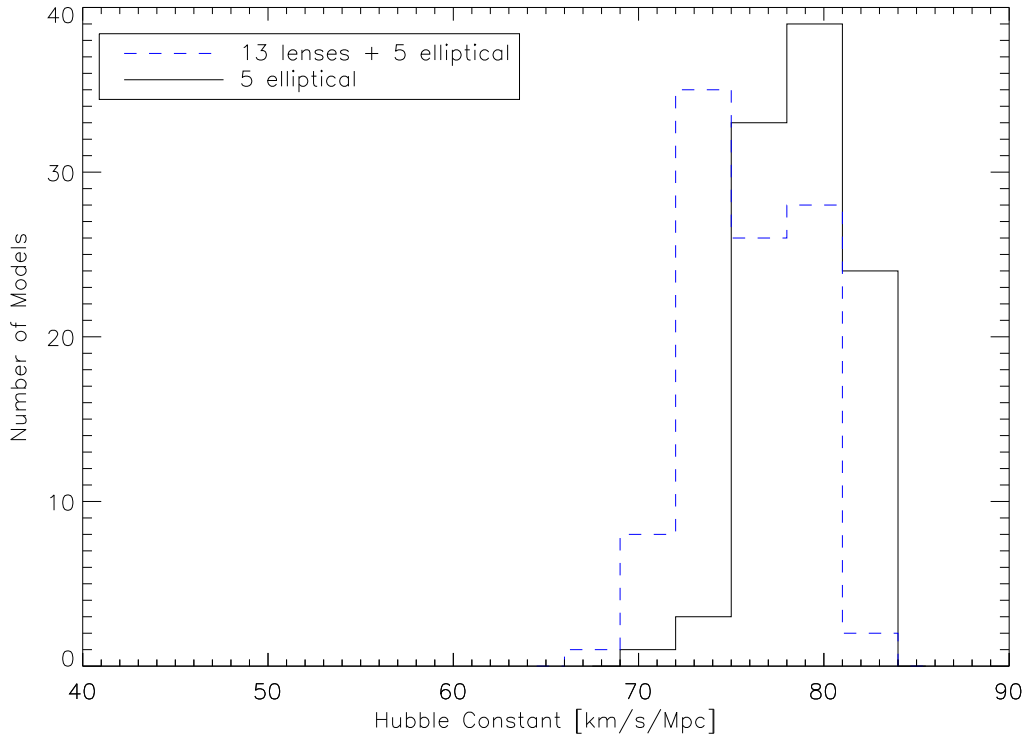

Figure 6.4: *Histogram of the distribution of H_0 values for the selected sample of 5 elliptical galaxies having constrained steepness of mass profiles in the range 1.8–2.2 (solid line) and the selected elliptical sample combined with the rest of the systems (dashed line). All calculations are done for a flat Universe with $\Omega_\Lambda = 0.7$ and $\Omega_m = 0.3$.*

6.6 CONCLUSIONS

Non-parametric modeling using PixeLens was applied to an ensemble of 18 lenses to determine a new value for the Hubble constant. We have obtained $H_0 = 66^{+6}_{-4}$ km s^{-1}Mpc^{-1} for a flat Universe with $\Omega_\Lambda = 0.7$, $\Omega_m = 0.3$. We have also compared our results with the two previous attempts to estimate H_0 from time delays (Saha et al. 2006, Oguri 2007) (Fig. 3).

Our additional result was based on studies of a selected sample of five lensing galaxies that have mass profiles close to $\rho \propto r^{-2}$. The Hubble constant recovered using the selected sample of elliptical galaxies combined with the rest of the systems is $H_0 = 76^{+3}_{-3}$ km s^{-1}Mpc^{-1}.

The gravitational lensing method that constrains H_0 has difficulties due to a couple of degeneracies between mass and time delay. The major degeneracy, the mass-sheet degeneracy, as we have shown, can be addressed by a careful choice of galaxies and the others partially by a combined, pixelated analysis of a large sample of lenses. Pixelated lens modeling provides insight into the structure of galaxies and the distribution of dark matter which together with precise measurements of time delays gives a reliable cosmological method.

Lensing can already determine the Hubble constant approaching the accuracy level of other leading measurements. Nevertheless, still more observation are needed. Future data with precise time delay measurements and better lens models will give even better constraints on H_0, perhaps turning lensing into a very competitive method.

The Dark Cosmology Centre is funded by the DNRF. DP thanks Prasenjit Saha for very extensive and patient help with PixeLens.

7

GRAVITATIONAL LENSES AS COSMIC RULERS: $\Omega_{\rm m}$, Ω_Λ FROM TIME DELAYS AND VELOCITY DISPERSIONS

Danuta Paraficz and Jens Hjorth
2009, A&A, accepted

ABSTRACT –

We show that a cosmic standard ruler can be constructed from the joint measurement of the time delay, $\Delta\tau$, between gravitationally lensed quasar images and the velocity dispersion, σ, of the lensing galaxy. This is specifically, for a singular isothermal sphere lens, $D_{OL} \propto \Delta\tau/\sigma^2$, where D_{OL} is the angular diameter distance to the lens. Using MCMC simulations we illustrate the constraints set in the $\Omega_{\rm m}$–Ω_Λ plane from future observations.

7.1 INTRODUCTION

In the cosmological ΛCDM model, it is currently estimated that 96% of the total energy density of the Universe is in the form of dark matter (25%) and dark energy (74%). These proportions have been inferred from a number of completely independent measurements, e.g. cosmic microwave background (CMB) (Spergel et al. 2003, Komatsu et al. 2009), baryon acoustic oscillations (Eisenstein et al. 2005), supernovae (Riess et al. 1998, Perlmutter et al. 1999), large scale structure (Peacock et al. 2001), clusters of galaxies (White et al. 1993) and weak gravitational lensing (Weinberg & Kamionkowski 2003). Unfortunately, any astrophysical approach suffers from potential systematic uncertainties (e.g. supernovae – not standard but standardized candles with possible redshift evolution; CMB – various parameter degeneracies and interference with foregrounds; weak lensing – PSF influencing the galaxy shape measurement). It is therefore important to explore complementary methods for measuring these quantities. Gravitationally lensed quasars QSOs offer such an attractive alternative.

QSOs that are positioned in a way that a lens, i.e., a massive foreground object such as a galaxy or a group of galaxies, intersects the line of sight, can be seen as magnified, multiple images. Gravitationally lensed QSOs have already been used to set constraints on cosmological parameters. Notably Refsdal (1964) showed that the Hubble constant H_0 can be measured from a multiple imaged QSO if the time delay between the lensed images and the mass distribution of the lens are known; attempts to constrain the cosmological constant Λ have been based on gravitationally lensed QSO statistics (Fukugita et al. 1990). The importance of strong gravitational lensing in future constraints on the evolution of the dark energy equation of state parameter $w(z)$ has also been emphasized (Linder 2004).

In recent years, joint studies of stellar dynamics and gravitational lensing have proven very fruitful, e.g. the Lenses Structure & Dynamics (LSD) Survey and the Sloan Lens ACS Survey (SLACS) were used to constrain the density profiles of galaxies (Treu & Koopmans 2004, Koopmans et al. 2006*b*). Methods for using either velocity dispersions (Grillo et al. 2008) or time delays (Dobke et al. 2009) of lensed systems have been proposed as estimators of $\Omega_{\rm m}$ and Ω_Λ.

We note that a standard cosmic ruler can be constructed from the joint measurement of the time delay between QSO images and the velocity dispersion of the lensing galaxy, independent of the redshift of the QSO. We explore its use to constrain $\Omega_{\rm m}$ and Ω_Λ in view of the large samples of lenses to be found in forthcoming experiments, such as from the Large Synoptic Survey Telescope (LSST), Square Kilometre Array (SKA), Joint Dark Energy Mission (*JDEM*), *Euclid*, and the Observatory for Multi-Epoch Gravitational Lens Astrophysics (*OMEGA*) (Dobke et al. 2009, Ivezic et al. 2008, Carilli & Rawlings 2004, Marshall et al. 2005, Moustakas et al. 2008).

7.2 LENSES AS STANDARD RULERS

The time delay $\Delta\tau$ is the combined effect of the difference in length of the optical path between two images and the gravitational time dilation of two light rays passing through different parts of the lens potential well,

$$\Delta\tau = \frac{1+z_{\rm L}}{c}\frac{D_{\rm OS}D_{\rm OL}}{D_{\rm LS}}\left(\frac{1}{2}(\vec{\theta}-\vec{\beta})^2 - \Psi(\vec{\theta})\right). \tag{7.1}$$

Here $\vec{\theta}$ and $\vec{\beta}$ are the positions of the images and the source respectively, $z_{\rm L}$ is the lens redshift, and Ψ is the effective gravitational potential of the lens. $D_{\rm OL}$, $D_{\rm OS}$, $D_{\rm LS}$ are the angular diameter distances between observer and lens, observer and source, and lens and source, respectively. If the lens geometry $\vec{\theta}-\vec{\beta}$ and the lens potential Ψ are known, the time delay measures the ratio

$D_{\rm OS}D_{\rm OL}/D_{\rm LS}$, also known as the effective lensing distance $r(z, \Omega_{\rm m}, \Omega_\Lambda)$, which depends on the cosmological parameters.

The observed velocity dispersion of a galaxy σ is the result of the superposition of many individual stellar spectra, each of which has been Doppler shifted because of the random stellar motions within the galaxy. Therefore, it can be determined by analyzing the integrated spectrum of the galaxy, which has broadened absorption lines due to the motion of the stars. The velocity dispersion is related to the mass through the virial theorem: $\sigma^2 \propto M_\sigma/R$, where M_σ is the mass enclosed inside the radius R. The mass is measured by the Einstein angle $\theta_{\rm E}$ of the lensing system $M_{\theta_{\rm E}} = \frac{c^2}{4G}\frac{D_{\rm OL}D_{\rm OS}}{D_{\rm LS}}\theta_{\rm E}^2$, where $R = D_{\rm OL}\theta_{\rm E}$. Thus, $\sigma^2 \propto \frac{D_{\rm OS}}{D_{\rm LS}}\theta_{\rm E}$.

Since the time delay is proportional to $D_{\rm OS}D_{\rm OL}/D_{\rm LS}$ and the velocity dispersion is proportional to $D_{\rm OS}/D_{\rm LS}$, the ratio $\Delta\tau/\sigma^2$ is dependent only on the lens distance and therefore acts as a cosmic ruler: $\Delta\tau/\sigma^2 \propto D_{\rm OL}$ [1]. In Fig. 7.1 we illustrate the dependency on the lens redshift of the measurables, time delay $\Delta\tau$, velocity dispersion squared σ^2, and the ratio between them, $\Delta\tau/\sigma^2$. To show the sensitivity of the three functions to Ω_Λ, we plot them for four cases of a flat ($\Omega_{\rm m} + \Omega_\Lambda = 1$) Universe with $\Omega_\Lambda = 0.2$, 0.5, 0.7 and 0.9, relative to an Einstein–de Sitter Universe ($\Omega_{\rm m} = 1, \Omega_\Lambda = 0$).

We can see that $\Delta\tau/\sigma^2$ is more sensitive to the cosmological parameters than $\Delta\tau$ or σ^2 separately. We also note that the higher the lens redshift the more pronounced is the dependency on cosmology, hence it is important for this method to study high redshift lenses. Finally, it has the advantage of being independent of the source redshift.

[1] A standard ruler can be used to measure angular diameter distances. Standard candles, on the other hand, measure luminosity distances, which can be obtained by multiplying angular diameter distances by a factor $(1+z)^2$.

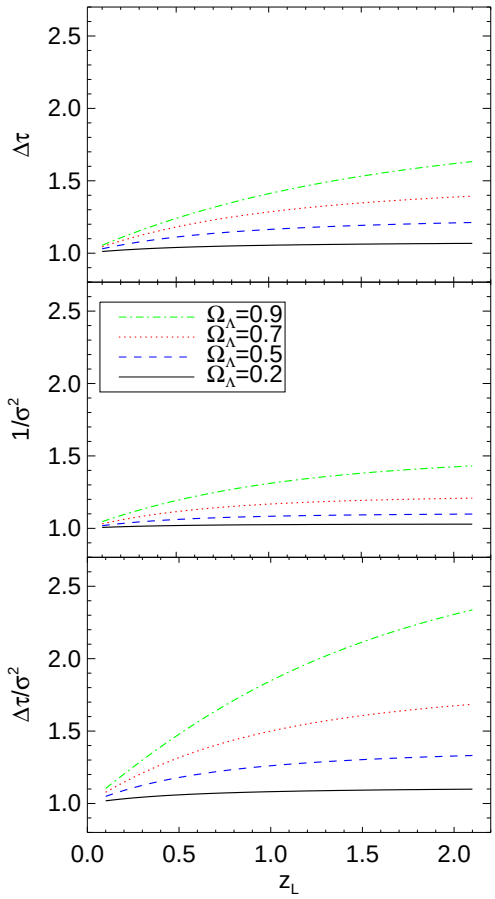

Figure 7.1: *Dependence of the three quantities, $\Delta\tau$ (**top** panel), σ^2 (**middle** panel), $\Delta\tau/\sigma^2$ (**bottom** panel) on the lens redshift. The source redshift was fixed to $z = 3$. A flat Universe ($\Omega_\mathrm{m} + \Omega_\Lambda = 1$) was assumed with 4 different values Ω_Λ: 0.2, 0.5, 0.7 and 0.9. Each curve is plotted relative to a flat Einstein–de Sitter Universe ($\Omega_\mathrm{m} = 1$, $\Omega_\Lambda = 0$).*

Both velocity dispersion and time delay depend on the gravitational potential of the lens galaxy. For the simple case of a singular isothermal sphere (SIS) both parameters can be easily expressed analytically. While the SIS model is convenient for its simplicity, it is also a surprisingly useful model for lens galaxies (Koopmans et al. 2006*b*, Oguri 2007, Guimarães & Sodré 2009, Koopmans et al. 2009).

The time delay is

$$\Delta\tau_{\rm SIS} = \frac{1+z_{\rm L}}{2c}\frac{D_{\rm OL}D_{\rm OS}}{D_{\rm LS}}(\theta_2^2-\theta_1^2) \tag{7.2}$$

and the velocity dispersion is

$$\sigma^2_{\rm SIS} = \theta_{\rm E}\frac{c^2}{4\pi}\frac{D_{\rm OS}}{D_{\rm LS}}. \tag{7.3}$$

For the SIS model the Einstein angle is half the distance between the lensed images, $\theta_{\rm E} = (\theta_1 + \theta_2)/2$ (we define $\Delta\tau$ and $\theta_{1,2}$ to be positive, with $\theta_2 \geq \theta_1$). Hence

$$D_{\rm OL}(\theta_2-\theta_1) = \frac{c^3}{4\pi}\frac{\Delta\tau_{\rm SIS}}{\sigma^2_{\rm SIS}(1+z_{\rm L})}. \tag{7.4}$$

7.3 MONTE CARLO MARKOV CHAIN SIMULATIONS

To explore the constraints set on cosmological parameters from the joint measurements of image positions, lens redshift, time delay and velocity dispersion, we perform simulations on SIS lenses using the Metropolis algorithm (Saha & Williams 1994). To simulate the uncertainties of the measurables we use χ^2 given by:

$$\chi^2 = \frac{\left[\frac{\Delta\tau}{\sigma^2\theta_{\rm E}(1+z_{\rm L})}\frac{c^3}{8\pi} - r(z,\Omega_{\rm m},\Omega_\Lambda)\right]^2}{\left(\frac{c^3}{8\pi}\right)^2\left[\left(\frac{\Delta\tau}{\sigma^2\theta^2_{\rm E}}\frac{\delta\theta_{\rm E}}{1+z_{\rm L}}\right)^2+\left(\frac{\Delta\tau}{\sigma^4\theta_{\rm E}}\frac{\delta\sigma^2}{1+z_{\rm L}}\right)^2+\left(\frac{\delta\Delta\tau}{\sigma^2\theta_{\rm E}(1+z_{\rm L})}\right)^2\right]}, \tag{7.5}$$

where, $r(z,\Omega_{\rm m},\Omega_\Lambda)$ is a angular diameter distance. For simplicity we have assumed that for each simulated lens, the lens images are aligned such that $\theta_1 = 0$ and $\theta_2 = 2\theta_{\rm E}$. Similar expressions are computed for $\Delta\tau$ and σ^2. In all the simulations we let $\Omega_{\rm m}, \Omega_\Lambda$ vary between 0 to 1 while either fixing or marginalizing over H_0.

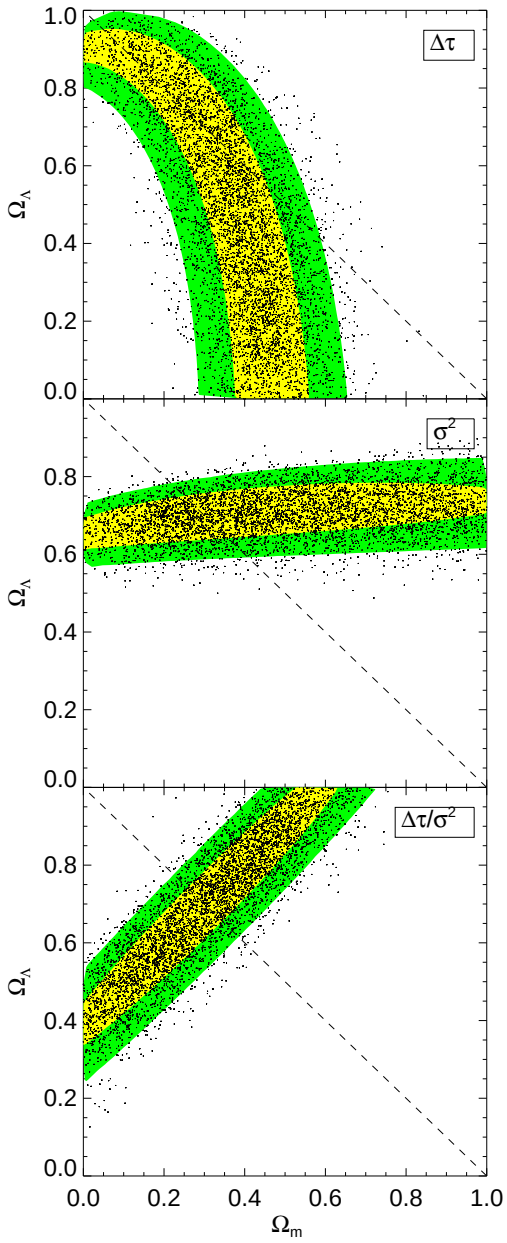

Figure 7.2: *MCMC simulations for three different cases:* $\Delta\tau$ (**top**, *panel),* σ^2 (**middle** *panel), and* $\Delta\tau/\sigma^2$ (**bottom** *panel). 125 galaxies were generated with redshifts equally distributed between 0.1 and 1.1, source redshifts between 1.5 and 3.5, and velocity dispersions varying from 100 to 300* km s^{-1}. For each lens we calculate the Einstein angle for a SIS in a cosmology with $\Omega_{\rm m} = 0.3$, $\Omega_\Lambda = 0.7$. H_0 was fixed at 70 km s^{-1} Mpc^{-1}. *Yellow* regions are 1σ, *green* are 2σ confidence levels.

7.3.1 COMPARISON OF METHODS

We first illustrate the constraints set in the $\Omega_{\rm m}$–Ω_Λ plane for 125 simulated galaxies. Their redshifts are equally distributed between 0.1 and 1.1, the source redshifts between 1.5 and 3.5, and the velocity dispersions in the range 100 to 300 km s^{-1}. For each lens we calculate the Einstein angle from Eq. 7.3 assuming $\Omega_{\rm m} = 0.3$, $\Omega_\Lambda = 0.7$ and $H_0 = 70$ km s^{-1} Mpc^{-1}. We constrain the sample to easily detectable systems, thus we include in the simulations only lenses with θ_E larger than $0\farcs5$ (Grillo et al. 2008). We assume simulated 5% uncertainties in the Einstein angle and run 10000 minimizations of χ^2 for three different observables: $\Delta\tau$, σ^2, and $\Delta\tau/\sigma^2$ (see Fig. 7.2).

The constraints on the parameter space from the time delay (Fig. 7.2, top panel) have a non-linear, curved shape (Coe & Moustakas 2009) elongated roughly in the $\Omega_{\rm m} + \Omega_\Lambda = 1$ direction. The velocity dispersion (Fig. 7.2, middle panel) gives a good constraint on Ω_Λ but a weak one on $\Omega_{\rm m}$. Joint observations of time delay and velocity dispersion (Fig. 7.2, bottom panel), give constraints approximately perpendicular to the flat Universe line similarly to Type Ia supernovae. As expected, the proposed cosmic ruler (Eq. 7.4) gives tighter constraints on both cosmological parameters than the two other methods.

7.3.2 ONE HIGH-REDSHIFT LENS

To study the constraints on cosmological parameters from a single lens we run 10000 minimizations on one system with parameters similar to an existing lens, MG 2016+112 (Lawrence et al. 1984). We set the lens redshift to 1.0, the source redshift to 3.27 and the Einstein angle to $1\farcs7$. The velocity dispersion is calculated from Eq. 7.3 assuming $\Omega_{\rm m} = 0.3$, $\Omega_\Lambda = 0.7$. We perform simulations for two uncertainty scales (5% and 10%). Because the results do not depend on the parameter from which the uncertainty comes, the simulated error can be understood as the uncertainty in either the velocity dispersion squared, the time delay, the Einstein angle, or a combination of these. We present the results from these simulations in Figure 7.3 (top row). The probability contours form a wide stripe going across the parameter space in a direction almost perpendicular to the $\Omega_{\rm m} + \Omega_\Lambda = 1$ line. To show the importance of H_0 in the simulations we present two cases, first for marginalized $H_0 = 70 \pm 5$ km s^{-1} Mpc^{-1} (left column) and second for fixed $H_0 = 70$ km s^{-1} Mpc^{-1} (right column). The shift in the marginalized case between the 5% and 10% confidence contours is due to the fact that high values of H_0 change the distances calculated from angular diameter distance equation less than the low ones, thus, to compensate, the region with simulated 10% uncertainties is shifted towards lower values of $\Omega_{\rm m}, \Omega_\Lambda$ compared to the 5% region.

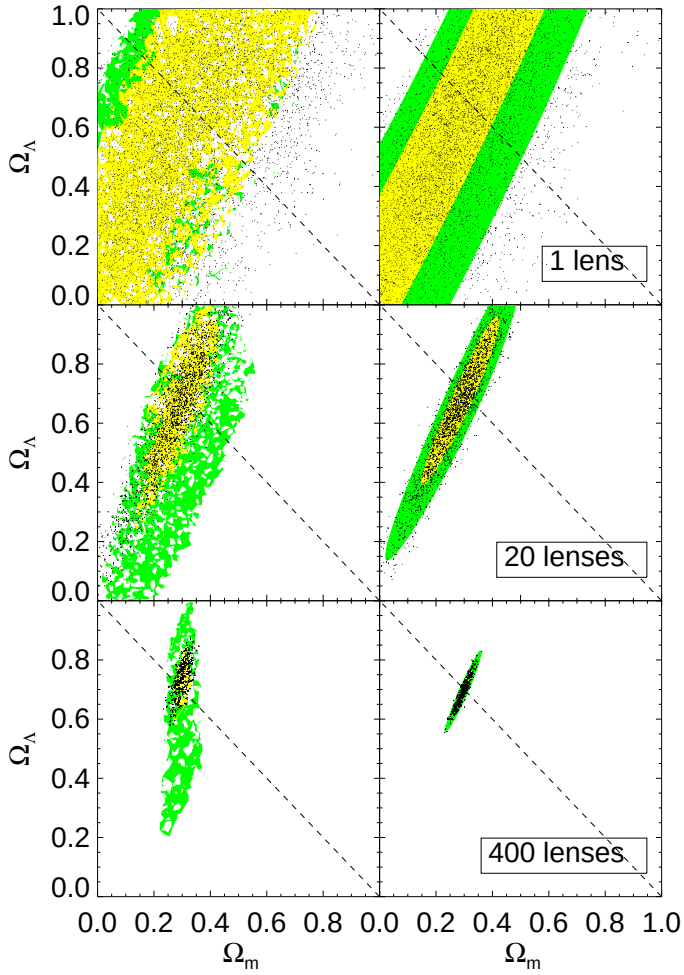

Figure 7.3: *MCMC simulations for $\Delta\tau/\sigma^2$. Top row: One lens with parameters similar to MG 2016+112 ($z_\mathrm{L} = 1.0$, $z_\mathrm{s} = 3.27$, $\theta_\mathrm{E} = 1\farcs7$). Middle row: 10 lensing systems with lens redshifts equally distributed between 0.5 and 1.5. Bottom row: 400 lensing systems as for middle row. 10000 MCMC minimizations were performed. All three simulations were performed for 2 uncertainty scales: 5% (yellow) and 10% (green). Left column: The plots marginalized over H_0. Right column: H_0 is fixed to 70 km s^{-1} Mpc^{-1}.*

7.3.3 MANY LENSES

We also simulate 20 and 400 lensing systems with lens redshifts equally distributed between 0.5 and 1.5 (Fig. 7.3). In this case the probability of detecting the correct cosmological parameters converges faster around the assumed 'real' values $\Omega_{\rm m} = 0.3$, $\Omega_\Lambda = 0.7$, creating, as a constant probability contour, an ellipse. The simulations show that by observing 20-400 lenses with small measurement errors, cosmological parameters can be well constrained. For a 5% error in the marginalized case we get for 20 lenses: $\Omega_\Lambda = 0.65^{+0.17}_{-0.21}$, $\Omega_{\rm m} = 0.30^{+0.15}_{-0.07}$ and for 400 lenses: $\Omega_\Lambda = 0.70^{+0.05}_{-0.06}$, $\Omega_{\rm m} = 0.30^{+0.02}_{-0.02}$ (1 σ confidence interval).

7.4 DISCUSSION

In our simulations we have assumed that the lenses have SIS mass distributions. The SIS profile seems to be a rather good choice, because several studies based on dynamics of stars, globular clusters, X-ray halos, etc. have shown that elliptical galaxies have approximately flat circular velocity curves (Koopmans et al. 2006*b*, Oguri 2007, Schechter & Wambsganss 2004, Guimarães & Sodré 2009, Gerhard et al. 2001). The structure of these systems may be considered as approximately homologous, with the total density distribution (luminous+dark) close to that of a singular isothermal sphere. We stress, however, that the proposed cosmic ruler does not rely on the assumption of a SIS. For any potential characteristic of the lens galaxies it is sufficient to assume that the potential (on average) does not change with redshift (or that any evolution can be quantified and corrected for). In other words, $\Delta\tau/\sigma^2 \propto D_{\rm OL}$ for all lens models. While we cannot rule out some redshift evolution, it is expected to be weak (Holden et al. 2009), given that lens galaxies are typically massive and hence fairly relaxed, giving rise to similar structures as their lower-redshift counterparts.

Nevertheless, like for any cosmic ruler, there is a range of possible systematic uncertainties which must be addressed before it can be used for precision cosmology. Several factors affect the lensing configuration, the velocity dispersion, and the time delays to various degrees: velocity anisotropy, total mass-profile shape (Schwab et al. 2009) and the detailed density structures (mass profiles of dark and luminous matter, ellipticities) of the lenses (Tonry 1983), mass along the line of sight to the QSO (Lieu 2008) and in the environment of the lenses, such as groups and clusters (Metcalf 2005) (the mass-sheet degeneracy (Saha 2000, Falco et al. 1985, Williams & Saha 2000, Oguri 2007)) and substructure (Dalal & Kochanek 2002, Macciò & Miranda 2006, Macciò et al. 2006, Xu et al. 2009). These factors are of the order of our assumed measurement uncertainties.

Fortunately, the velocity anisotropy appears to be small in lens galaxies (Koopmans et al. 2009, van de Ven et al. 2003) and in relaxed galaxies in general (Hansen & Moore 2006, An & Evans 2006). The density structures of elliptical galaxies appear to be fairly universal (Bak & Statler 2000, Alam & Ryden 2002). The effects of extrinsic mass are important but usually limited (Holder & Schechter 2003) and can be spotted from anomalous flux ratios or lensing configurations.

To date, there are around 200 known strong gravitational lens systems, but only 20 of them have measured time delays, with typical errors of 5–10%. Similar errors are obtained for measured velocity dispersions. In other words, applying the method to current data will not provide sufficiently tight constraints on $\Omega_{\rm m}$, Ω_Λ to be competitive with current cosmological methods. Ultimately therefore, to address systematic errors and to turn the proposed cosmic ruler into a useful cosmological tool, a large sample of homogenous systems is needed, e.g. high-redshift early-type galaxies with σ, $\Delta\tau$, and the locations of the images measured with high precision.

From the sample, one may eliminate problematic systems, such as systems with a lot of external shear, or non-simple lenses. Moreover, each lens would have to be modeled in detail, i.e. accounting for systematic uncertainties by measuring them directly and including the effects in the analysis.

Future facilities will allow such an experiment. LSST, SKA, *JDEM*, *Euclid*, and *OMEGA* (Dobke et al. 2009, Ivezic et al. 2008, Carilli & Rawlings 2004, Marshall et al. 2005, Moustakas et al. 2008)Â will both find large numbers of new lenses and have the potential to accurately constrain the time delays. And with the James Webb Space Telescope (*JWST*) or future 30–40-m class telescopes (e.g. TMT – Thirty Meter Telescope and E-ELT – European Extremely Large Telescope), velocity dispersions can be obtained to the precision required and velocity anisotropy can be effectively constrained through integral field spectroscopy (Barnabè et al. 2009). This must be coupled with high-resolution imaging which can constrain both the density structures of the lenses and significant mass structures affecting the lensing. Extrinsic mass and density structures can also be constrained indirectly by modeling the lensing configuration, including flux ratios and positions of the images.

The Dark Cosmology Centre is funded by the DNRF.

8

CONCLUSIONS AND OUTLOOK

8.1 CONCLUSIONS

In this Thesis we have extensively explored one property of strong gravitational lensing: the time delay. We have investigated strong gravitational lensing systems and in particular the time delay from both an observational and theoretical approach, focusing on the time delay as a cosmological and astrophysical tool to constrain H_0, Ω_m, Ω_Λ, and to measure the masses of lensing galaxies.

We have started out study by measuring the time delay of one lensed system and based on that we have measured H_0. However, due to degeneracy of H_0 with the mass of the lens, a measurement of H_0 based on only one case is not very reliable. Hence, we have combined all lensed systems with know time delays and measured H_0 using the statistical ensemble. Using this sample we have also shown that H_0 can be better constrained if only those systems where the lens is an elliptical galaxy are used. Our final result is that Ω_m and Ω_Λ can also be constrained using strongly lensed quasars. We have shown that combining gravitational lensing and stellar dynamics studies offers a competitive method for estimating cosmological parameters in the near future.

8.1.1 TIME DELAYS

We have estimated the time delay of SDSS J1206+4332 to be $\Delta\tau = 116^{+6}_{-7}$ based on a 280-day long monitoring campaign at the Nordic Optical Telescope. This shows the feasibility of measuring time delays from campaigns not much longer than the time delay itself. To model the system, we first assumed a single lensing galaxy modeled with a singular isothermal ellipsoid (SIE), but we were unable to reproduce the image positions. By adding to the lens model two further galaxies G2 and G3, we found that the influence of G2 is negligible due to its small redshift, but G3 has a major impact on the system geometry. A lens model with two galaxies, where the main one is a SIE and the second is a SIS, predicts the image positions very well. Thus this model resulted in a Hubble constant of 73^{+3}_{-4} km s^{-1} Mpc^{-1} assuming $\Omega_{\rm m} = 0.3$ and $\Omega_\Lambda = 0.7$.

Unluckily, lack of short-term variability in the other monitored systems (SDSSJ 0903, SDSS J1001+5027, SDSS J1353+1138, SDSS J1335+0118) do not allow us to measure their time delays. From the quasar studies of Fohlmeister et al. (2008), Vuissoz et al. (2007), Koopmans et al. (2000), and many others, we see that in the time span of 200–300 days of monitoring a quasar might be in its quiet stage or undergo a slow increase or decrease. Thus, despite our success in measuring the time delay of SDSS J1206+4332, it appears that monitoring substantially longer than the

predicted time delay of a given system is necessary in most cases.

We have modeled all five systems using both analytical and pixelated methods. Using the predicted time delays we have shown that none of the systems exhibited significant microlensing variability during the observing campaign.

We have also performed simultaneous pixelated modeling with a shared Hubble constant of five lenses which time delays were measured at the NOT. The estimated Hubble constant from this analysis is $H_0 = 61.5^{+8}_{-4}$ km s^{-1} Mpc^{-1}.

8.1.2 STATISTICS

Non-parametric modeling using PixeLens was applied to an ensemble of 18 lenses to obtain a new determination of the Hubble constant. We have obtained $H_0 = 65.7^{+6.2}_{-3.7}$ km s^{-1}Mpc^{-1} for a flat Universe with $\Omega_\Lambda = 0.7$ and $\Omega_m = 0.3$. We have also compared our results with the two previous attempts to estimate H_0 from time delays (Saha et al. 2006, Oguri 2007, Fig. 3).

An additional result was based on studies of a selected sample of five lensing galaxies that have mass profiles close to $\rho \propto r^{-2}$. The Hubble constant recovered using the selected sample of elliptical galaxies, combined with the rest of the systems, is $H_0 = 75.8^{+3.4}_{3.3}$ km s^{-1}Mpc^{-1}.

The gravitational lensing method to constrain H_0 faces a difficulty due to a couple of degeneracies between mass and time delay. The major degeneracy, the so-called mass-sheet, as we have shown, can be avoided by a careful choice of galaxies and the others, partially, by a combined, pixelated analysis of a large sample of lenses. Pixelated lens modeling provides insights into the structure of galaxies and the distribution of dark matter, which, together with precise measurements of time delays, provides a reliable cosmological method.

8.1.3 THEORY

We have shown that $\Omega_{\rm m}$ and Ω_Λ can be constrained from the joint measurement of the time delay, $\Delta\tau$, between gravitationally lensed quasar images and the velocity dispersion, σ, of the lensing galaxy, because $D_{OL} \propto \Delta\tau/\sigma^2$, where D_{OL} is the angular diameter distance to the lens.

Using Monte Carlo Markov Chain simulations we have illustrated the constraints set in the $\Omega_{\rm m}$–Ω_Λ plane from future observations. For 20 simulated lenses with cumulative 5% error we obtain: $\Omega_\Lambda = 0.65^{+0.17}_{-0.21}$, $\Omega_{\rm m} = 0.30^{+0.15}_{-0.07}$, and for 400 simulated lenses with cumulative 5% error we get: $\Omega_\Lambda = 0.70^{+0.05}_{-0.06}$, $\Omega_{\rm m} = 0.30^{+0.02}_{-0.02}$ (1σ confidence interval).

In our simulations we have used lenses that have SIS mass distributions. This choice was made because several studies, based on dynamics of stars, globular clusters, X-ray halos, etc., have shown that elliptical galaxies have approximately flat circular velocity curves (Koopmans et al. 2006*b*, Oguri 2007, Schechter & Wambsganss 2004, Guimarães & Sodré 2009, Gerhard et al. 2001), i.e., the structure of these systems can be considered as approximately homologous, with the total density distribution (luminous + dark matter) close to that of a singular isothermal sphere.

8.2 FUTURE

To date, there are around 200 known strong gravitational lens systems but only 20 of them have measured time delays, with typical errors of 5–10%. In other words, applying gravitational lensing methods to the currently available data will not provide sufficiently tight constraints on H_0, $\Omega_{\rm m}$, Ω_Λ to be competitive with other cosmological methods. Moreover, up to now most efforts have focused on studies of individual time delay lenses, which result in very different

values of H_0, which is due to varying lens properties (mostly mass slope) and environments (lensing by galaxy groups).

Therefore, to address systematic errors and to turn the gravitational lensing into a useful cosmological tool, additional stellar dynamics studies of lensing galaxies and a large sample of homogenous lensed systems is needed, e.g., high-redshift early-type galaxies that are known to be isothermal ($\rho \propto r^{-2}$; e.g. Koopmans et al. 2009, Gerhard et al. 2001). To make that sample more homogenous one may additionally eliminate problematic systems, such as systems with a lot of external shear, or non-simple lenses.

Gravitational lensing combined with stellar dynamics has a range of possible systematic uncertainties which must be addressed before it can be used for precision cosmology. Velocity anisotropy, total mass-profile shape (Schwab et al. 2009) and the detailed density structures (mass profiles of dark and luminous matter, ellipticities) of the lenses (Tonry 1983), mass along the line of sight to the QSO (Lieu 2008) and in the environment of the lenses, such as groups and clusters (Metcalf 2005), the mass-sheet degeneracy (Saha 2000, Falco et al. 1985, Williams & Saha 2000, Oguri 2007) and substructures (Dalal & Kochanek 2002, Macciò & Miranda 2006, Macciò et al. 2006, Xu et al. 2009), all affect the lensing configuration, the velocity dispersion, and the time delays to various degrees, which are of order of our assumed measurement uncertainties.

Fortunately, the velocity anisotropy appears to be small in lens galaxies (Koopmans et al. 2009, van de Ven et al. 2003) and in relaxed galaxies in general (Hansen & Moore 2006). The density structures of elliptical galaxies appear to be fairly universal (Bak & Statler 2000, Alam & Ryden 2002). The effects of extrinsic mass are important but usually limited (Holder & Schechter 2003) and can be spotted from anomalous flux ratios or lensing configurations.

The main objectives of the future research are the following.

- Using spectroscopic and imaging observations of lenses that are early-type galaxies, derive internal properties and distribution of environments of elliptical galaxies, resolve the source structure, study stellar populations of lensing galaxies, look for evidence of evolution with redshift and dust properties through absorption.

- Using statistics on available data from e.g. SDSS, SLACS, quantify the effects of systematics and the scatter in the H_0 estimation from individual galaxies due to physical properties of the lens (ellipticity, density profile slope) and environment (shear).

- Develop the technique to include the velocity dispersion constraint in the simultaneous pixelated modeling.

- Measure time delays of the newly discovered lenses and use existing and forthcoming data (e.g. COSMOGRAIL) elliptical lenses to constrain the cosmological parameters.

In recent years there has been an increase in the number of strong lenses discovered by searches such as CLASS (Myersetal. 2003) and SLACS (Bolton et al. 2006). Future facilities LSST, SKA, *JDEM*, *Euclid*, *OMEGA*, and Pan-STARRS (already operational Dobke et al. 2009, Ivezic et al. 2008, Carilli & Rawlings 2004, Marshall et al. 2005, Moustakas et al. 2008, Kaiser 2004) will both find large numbers of new lenses and have the potential to accurately constrain the time delays, through repeated observations in these surveys, and/or through lensing specialized missions (such as OMEGA; Moustakas et al. 2008).

With the James Webb Space Telescope (*JWST*) or future 30–40-m class telescopes (e.g. TMT, the Thirty Meter Telescope, and E-ELT – the European Extremely Large Telescope), velocity dispersions can be obtained to the precision required and velocity anisotropy can be effectively

constrained through integral field spectroscopy (Barnabè et al. 2009). This must be coupled with high-resolution imaging which can constrain both the density structures of the lenses and significant mass structures affecting the lensing.

Lensing can already determine the Hubble constant approaching the accuracy level of other leading measurements. Nevertheless, still more observations are needed. Future data with precise time delay measurements and better lens models will give even better constraints on H_0, perhaps turning lensing into a very competitive method.

A

RESOLVING THE DISCREPANCY BETWEEN LENSING AND X-RAY MASS ESTIMATES OF THE COMPLEX GALAXY CLUSTER ABELL 1689

ABSTRACT –

There is a long-standing discrepancy between galaxy cluster masses determined from X-ray and gravitational lensing observations of which Abell 1689 is a well-studied example. In this work we take advantage of 180 ks of Chandra X-ray observations and a new weak gravitational study based on a Hubble Space Telescope mosaic covering the central 1.8 *Mpc* $\times$ 1.4 *Mpc to eliminate the mass discrepancy. In contrast to earlier X-ray analyses where the very circular surface brightness has been inferred as Abell 1689 being spherically symmetric and in hydrostatic equilibrium, a hardness ratio map analysis reveals a regular and symmetric appearing main clump with a cool core plus some substructure in the North Eastern part of the cluster. The gravitational lensing mass model supports the interpretation of Abell 1689 being composed of a main clump, which is possibly a virialized cluster, plus some substructure. In order to avoid complications and mis-interpretations due to X-ray emission from the substructure, we exclude it from the mass reconstruction. Comparing X-ray and lensing mass profiles of the regular main part only, shows no significant discrepancy between the two methods and the obtained mass profiles are consistent over the full range where the mass can be reconstructed from X-rays (out to* $\approx$ 1*Mpc). The obtained cluster mass within* $\approx$ 875 *kpc derived from X-rays alone is* $6.4 \pm 2.1 \times 10^{14}\,\mathrm{M}_{\odot}$ *compared to a weak lensing mass of* $8.6 \pm 3.0 \times 10^{14}\,\mathrm{M}_{\odot}$ *within the same radius.*

A.1 INTRODUCTION

Gravitational lensing and X-ray observations are two independent methods, which can probe the mass of the largest virialized structures in the Universe, namely clusters of galaxies. The cluster mass is dominated by dark matter ($\approx 80\%$) and hot X-ray emitting gas ($\approx 20\%$). The baryonic matter in the galaxies only contributes a few percent of the mass. The spectrum of the X-ray emission from the gas depends on the temperature of the gas, which for a cluster in hydrostatic equilibrium is related to the total mass of the cluster. Gravitational lensing uses the distortion of background source images to probe the total mass along the line of sight. It has been widely debated whether cluster mass determinations from the two methods agree, and in some cases large discrepancies have been found (e.g. Loeb & Mao 1994, Miralda-Escude & Babul 1995, Voigt & Fabian 2006, Mahdavi et al. 2007, Zhang et al. 2008). The main motivation for studying a single cluster, Abell 1689, in large detail with the best available X-ray and lensing data is to get insight into the mass discrepancy by determining the mass distribution using both methods. It is checked that the results of a third independent mass determination method using the velocity dispersion of the galaxies within the cluster are consistent with the X-ray and lensing results.

Abell 1689 is a massive cluster with a redshift of $z = 0.1832$ (Teague et al. 1990). It is mostly known for its amazing gravitational arcs and large number of multiply imaged systems. Consequently it has been well studied with strong and weak gravitational lensing (Broadhurst, Takada, Umetsu, Kong, Arimoto, Chiba & Futamase 2005, Broadhurst, Benítez, Coe, Sharon, Zekser, White, Ford, Bouwens, Blakeslee, Clampin, Cross, Franx, Frye, Hartig, Illingworth, Infante, Menanteau, Meurer, Postman, Ardila, Bartko, Brown, Burrows, Cheng, Feldman, Golimowski, Goto, Gronwall, Herranz, Holden, Homeier, Krist, Lesser, Martel, Miley, Rosati, Sirianni, Sparks, Steindling, Tran, Tsvetanov & Zheng 2005, Halkola et al. 2007, Lemze et al. 2007, Limousin et al. 2007, Dahle et al. 2008). It has been proposed as a standard example of a spherical cluster of galaxies in hydrostatic equilibrium (Xue & Wu 2002, Lemze et al. 2007). However, earlier studies have found large discrepancies between the mass obtained from X-ray observations and from gravitational lensing (Andersson & Madejski 2004, Andersson et al. 2007, Lemze et al. 2007). Strong gravitational lensing analyses have found the central 300 kpc to consist of several subclumps (Limousin et al. 2007, Tu et al. 2007) and weak lensing reveals substructure on a larger scale (500 kpc) (Okura et al. 2008, Dahle et al. 2008). Furthermore an indication of substructure in the North Eastern (NE) part of Abell 1689 was seen by Andersson & Madejski (2004) in an *XMM-Newton* X-ray observation.

Recently new data have become available in the form of a very deep X-ray observation with *Chandra* (≈ 150 ks new exposure). In addition, a weak gravitational lensing analysis based on a mosaic using the Wide Field Planetary Camera 2 (WFPC2) instrument aboard the Hubble Space Telescope (HST) has recently been carried out (Dahle et al. 2008). This provides a unique mass map with an unprecedented combination of spatial resolution ($50\farcs$) and a large spatial extension. We explore both of these data sets in this work.

The long X-ray exposure allows us to create hardness ratio maps with a resolution of $5\farcs$ (Sec. A.2.4), revealing substructure in the X-ray emission from the NE part of the cluster. In contrast, the South Western (SW) part seems circular and very regular. Consequently we assume it to be spherically symmetric and relaxed, and we reconstruct the temperature and mass profiles from SW part alone (Sec. A.2.5). The mass profile of the SW part is compared to the lensing mass profile of the same region (Sec. A.3.3). The obtained profiles are in very good agreement and it is proposed that Abell 1689 consists of a spherically symmetric part plus some substructure in the NE part (Sec. A.2.9). We conclude that the mass profiles determined from high quality X-ray

and gravitational lensing data are in agreement.

Throughout the paper we have used a standard ΛCDM cosmology with $\Omega_{baryon} = 0.046$, $\Omega_\Lambda = 0.72$, $\Omega_{CDM} = 0.23$, and $H_0 = 70.1\,\mathrm{km\,s^{-1}\,Mpc^{-1}}$ (Hinshaw et al. 2008). At the redshift of Abell 1689, 1′ corresponds to 185 kpc for the chosen cosmological model. Unless otherwise stated, quoted uncertainties are one σ.

A.2 X-RAYS

A.2.1 X-RAY OBSERVATIONS

We have analyzed four *Chandra* X-ray observations from the NASA HEASARC archive[1] with a total exposure of approx. 180 ks (see Tab. A.1). It has been claimed that the two newest, and by far longest, observations cannot be used due to background issues (Lemze et al. 2007), but these can be overcome, as shown in Sec. A.2.3.

Observation id	Date	Exposure time	Data mode
1663	2001 Jan 7	10.73 ks	FAINT
5004	2004 Feb 28	19.86 ks	VFAINT
6930	2006 Mar 06	75.79 ks	VFAINT
7289	2006 Mar 09	74.61 ks	VFAINT

Table A.1: *The analysed Chandra observations of Abell 1689.*

The four observations in Tab. A.1 have been reprocessed with the calibration CALDB 3.4.1 and analysed with CIAO 3.4 (Fruscione et al. 2006) following standard procedures[2], The CIAO Data Analysis Page. We found the X-ray peak of Abell 1689 to have the position (R.A., decl.)=(197.87306^o, -1.3413889^o). In all observations, the X-ray peak was situated on the ACIS-I3 chip and we performed the analysis with events entirely from this chip.

A.2.2 X-RAY ANALYSIS: IMAGE AND SURFACE BRIGHTNESS

An exposure corrected X-ray image combined from the four observations is shown in Fig. A.1. The emission is almost circular tempting one to conclude that Abell 1689 is spherical and in hydrostatic equilibrium. However this is not the case, which is clearly demonstrated by the surface brightness profiles derived from Fig. A.1 for the NE and SW halves respectively (defined by the dashed white line). Fig. A.2 shows the ratio between the NE and SW profiles. It is evident that within ≈ 300 kpc the SW half is brighter, where outside ≈ 500 kpc the two halves are more equally bright with a tendency for the NW half to be brighter.

[1] http://heasarc.gsfc.nasa.gov/docs/archive.html
[2] http://cxc.harvard.edu/ciao3.4/

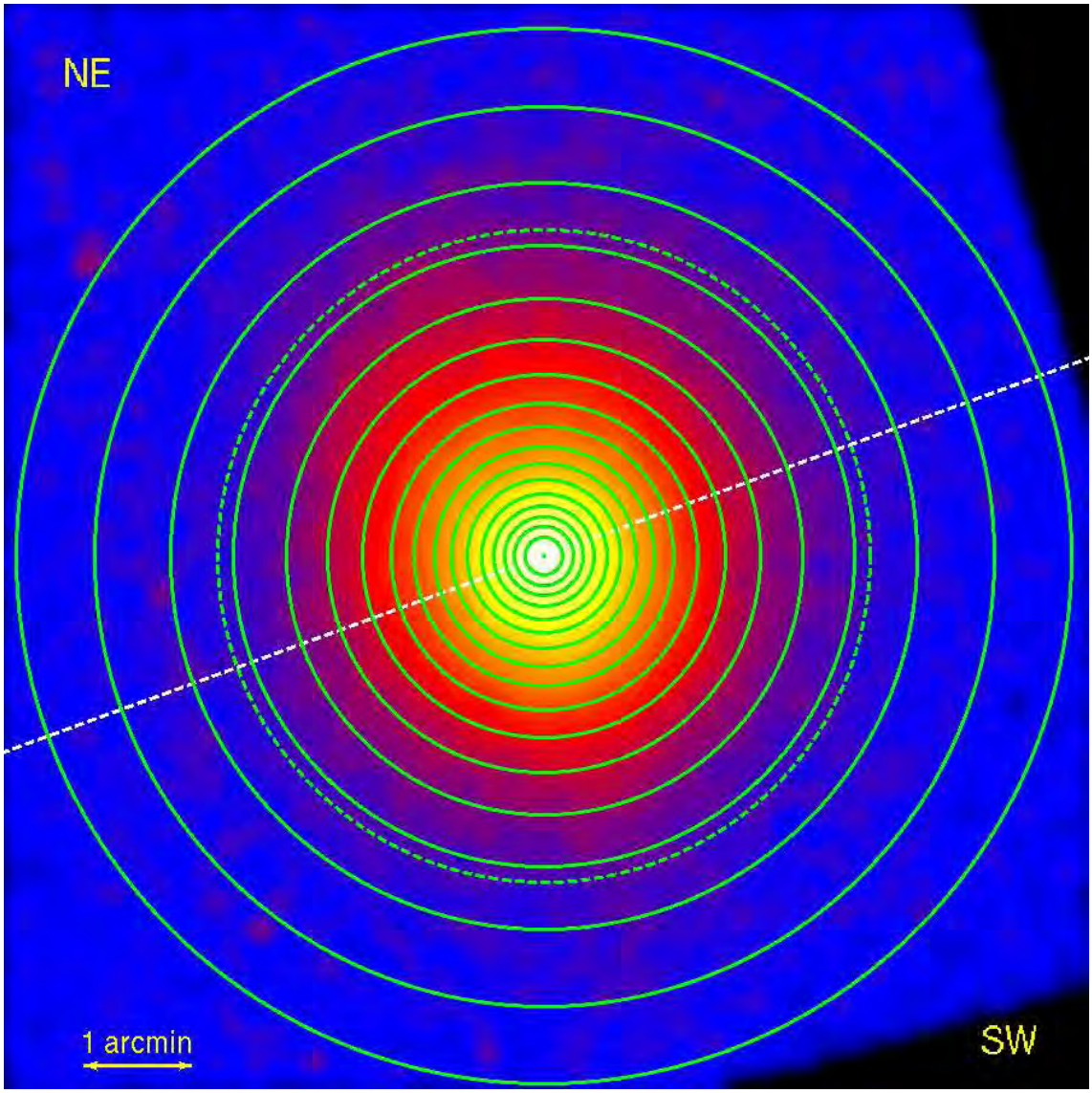

Figure A.1: *Exposure corrected X-ray image composed from the observations in Tab. A.1 (smoothed with a* $10''$ *wide Gaussian). The dashed white line through the X-ray peak (*20^o *angle) divides the cluster in the NE and SW halves. The annuli described in Sec. A.2.5 are shown in solid green and the* $3'$ *circle in dashed green.*

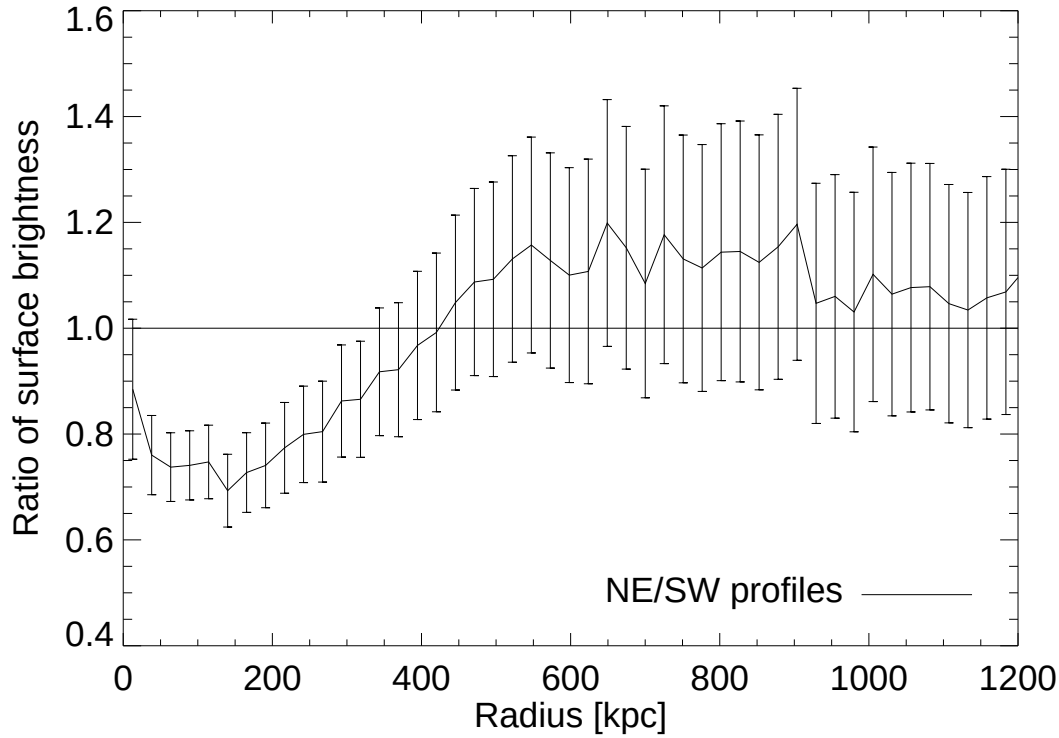

Figure A.2: *The ratio between the surface brightness profiles in the* $0.3 - 12.0$ *keV of the NE and SW halves with Poisson errors.*

A.2.3 X-RAY ANALYSIS: BACKGROUND

Chandra has two telemetry modes called FAINT and VFAINT (Very FAINT). They have different event gradings and thereby different background event selections (Chandra X-ray Centre Proposers' Observatory Guide, chapter 9 2007, ch. 6.14). Three of the four observations analysed here have been done in the VFAINT mode. The standard blank sky observations for background subtraction are produced from observations in the FAINT mode (Markevitch et al. 2003), and hence the shape of the background spectrum from a VFAINT observation deviates from the spectrum of a blank sky observation. However, instead of using the pipeline processed VFAINT data, the data can be reprocessed as FAINT observations. In the latter case, the shape of the background spectra of the two new, long observations 6930 and 7289 are identical to the corresponding blank sky spectra. We have extracted the blank sky spectra from the same chip regions as the observed cluster spectra and scaled the blank sky spectrum level to the corresponding observational spectrum in the 9-12 keV interval, where very little cluster emission is expected.

Instead of using the blank sky background, it is possible to use the local background from the same observation allowing to take advantage of the improved background reduction in the VFAINT mode. The background differs from chip to chip (in the CCD), so the local background has to be extracted from the same chip as the source region (in this case ACIS-I3). We have compared the two methods of background subtraction and the difference between the final results (e.g. the temperature) is negligible. In the following we have used the blank sky method whenever extracting spectra, since it allows us to use more of the chip for the actual analysis and hence determine the temperature further from the centre of the cluster. For the images we have used the VFAINT data since the background event grading is better.

A.2.4 X-RAY ANALYSIS AND RESULTS: HARDNESS RATIO

The ratio of low energy photons to high energy photons from the intra cluster medium is a proxy of the temperature structure of the cluster. If the cluster is isothermal and only radiates thermally, the ratio between soft and hard photons (S/H) will be independent of position (within the cluster). However, if there is a variation in temperature, we expect to see a difference in S/H. Even clusters in hydrostatic equilibrium have a radial temperature gradient, which we expect to see as a circular structure in the soft to hard photon ratio.

From the two longest exposures (observation id 6930 and 7289) we have created two hardness ratio maps with different energy splittings between the soft and hard photons. One has a splitting energy of 1.0 keV so S/H = E[0.3-1.0 keV]/E[1.0-10.0 keV] and the other of 6.0 keV so S/H = E[0.3-6.0 keV]/E[6.0-10.0 keV]. We produced a soft and a hard exposure corrected image with a binning of $5''$/pixel. The images were smoothed with a Gaussian of width $\sigma = 5''$, before the soft images were divided by the hard images. For visualisation, the hardness ratio maps were smoothed again with Gaussian of width $\sigma = 15''$, resulting in the two hardness ratio maps shown in Fig. A.3. Bright colour means excess of low energy photons. In the case of hydrostatic equilibrium this means colder, but since substructure is rarely in hydrostatic equilibrium, the temperature that can be derived from spectral fitting is not the actual physical temperature.

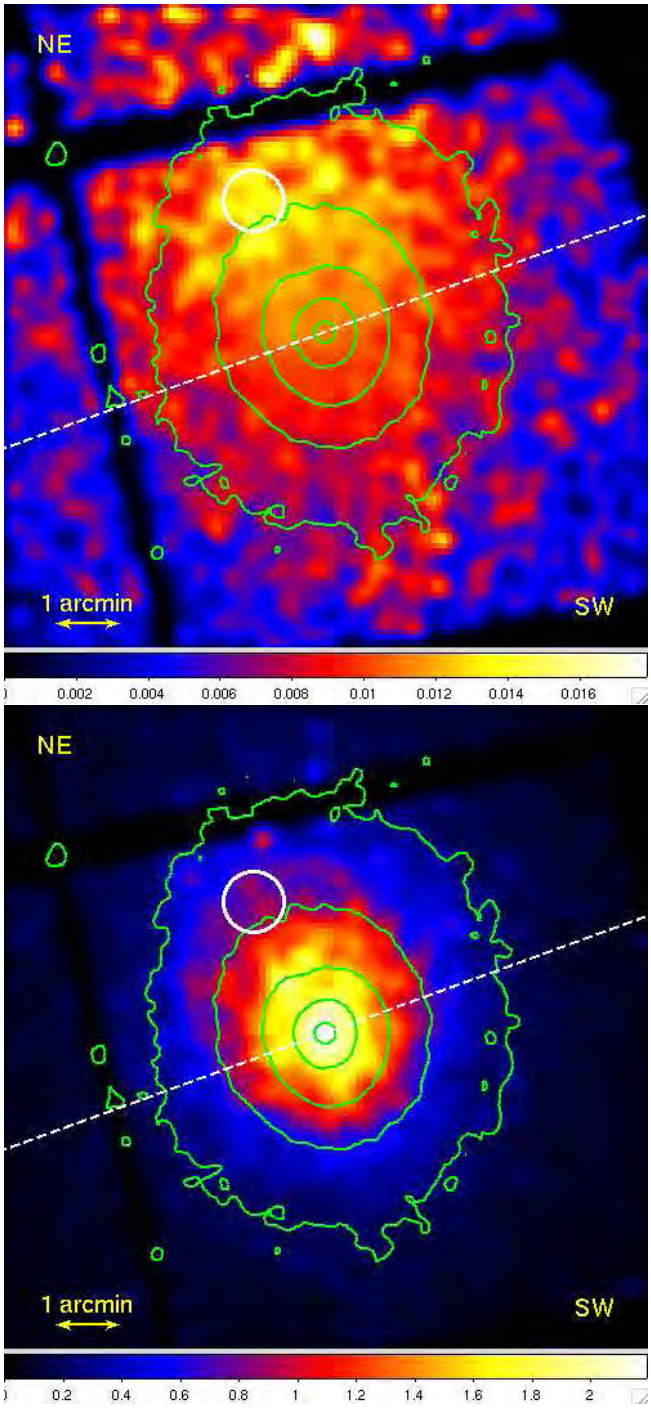

Figure A.3: *The obtained hardness ratio maps (bright is soft photon excess). The green contours show the almost circular total X-ray emission. The white line divides the cluster into the NE (upper) part and the SW (lower) regular and symmetrically appearing half. The white circle is the region analysed in Sec. A.2.8. Upper: The hardness ratio map for the energy splitting of* 1.0 *keV (S/H = E[0.3-1.0 keV]/E[1.0-10.0 keV]) Lower: The hardness ratio map for the energy splitting of* 6.0 *keV (S/H = E[0.3-6.0 keV]/E[1.0-10.0 keV]).*

In the 1.0 keV hardness ratio map (upper part of Fig. A.3) a substructure in the NE part of the cluster is clearly visible, where in the 6.0 keV hardness ratio map (lower part of Fig. A.3) only the (almost) circular symmetric part centered at the X-ray peak is visible. The splitting of 1 keV is commonly used (e.g. Fabian et al. 2000), but we have investigated several splittings between 0.5 keV and 7.0 keV. For splittings between 1.0 keV and 6.0 keV, the hardness ratio map shifts gradually between the two extremes shown in Fig. A.3, so increasing the splitting energy hides the NE structure and enhances the circular cluster structure.

The contours of the total X-ray emission from Abell 1689 (green in Fig. A.3) give the impression of being circular with only a slight elongation in the North-South direction. This elongation is more pronounced in the hardness ratio maps with the 1 keV splitting.

In the hardness ratio map with splitting at 6.0 keV there is a relative soft-photon excess centred at the position of the total X-ray peak, which indicates a cool core in the cluster.

From the hardness ratio maps it is inferred that Abell 1689 consist of a spherically symmetric part, which to the NE is obscured by come substructure. The cool core indicates that the spherical part of Abell 1689 is relaxed and in hydrostatic equilibrium (Voigt & Fabian 2006). Therefore we have split the cluster into two regions and in the following sections, the temperature and mass profiles have been determined from the symmetrically appearing SW part alone. The division line shown in Fig. A.1 and Fig. A.3 (white dashed) goes through the X-ray peak and is tilted by 20^o with respect to the East-West direction.

A.2.5 X-RAY ANALYSIS AND RESULTS: TEMPERATURE PROFILE

Assuming the intra cluster medium to be an optically thin and completely ionised gas, we determined the global properties of Abell 1689 by analysing a $0.5 - 8.0$ keV spectrum of the central $3'$. This radius was chosen because it includes most of the cluster emission (the dashed green circle in Fig. A.1) and the same radius is used in earlier analyses (Andersson & Madejski 2004, Lemze et al. 2007). An isothermal plasma model (MEKAL, Mewe et al. (1985)) including Galactic absorption was fitted to the spectrum using the spectral fitting package Xspec 12.3 (Arnaud et al. 2007). The absorption in neutral hydrogen along the line of sight was fixed to $1.83 \times 10^{20}\mathrm{cm}^{-2}$ (HeaSoft 2007, n_H tool). Leaving n_H a free parameter while fitting gave a consistent value. The redshift was fixed to $z = 0.183$. The redshift can also be determined from the spectral fitting, but the result had an uncertainty of $\approx 20\%$ and as a consequence we used the fixed value. Unfortunately this also excludes the idea of determining the distance along the line of sight to the NE substructure from the spectral fitting.

We obtained a global temperature of 10.5 ± 0.1 keV and an abundance of 0.37 ± 0.02 solar value for a reduced χ^2 of 1.3 (1725 degrees of freedom). This is consistent with earlier reported results (Xue & Wu 2002, Andersson & Madejski 2004, Lemze et al. 2007). 8 Clusters are not isothermal and consequently we made a radial temperature analysis. The X-ray emission of the NE part of Abell 1689 contains substructure in the low energies (see Sec. A.2.4 and Sec. A.2.9) indicating that this part of the cluster is complex. Hence, we have restricted the radial temperature analysis to the SW symmetrically appearing half of the cluster.

Using the four data sets and the blank sky background, we have extracted the spectra from the SW half of Abell 1689 in 17 half-circular bins centered at the X-ray peak and containing at least 30000 events each (green circles in Fig. A.1). The same model as for the global properties was fitted to the $0.5 - 8.0$ keV spectrum of each radial bin. The obtained (projected, 2D) temperature profile is shown in Fig. A.4 (black diamonds).

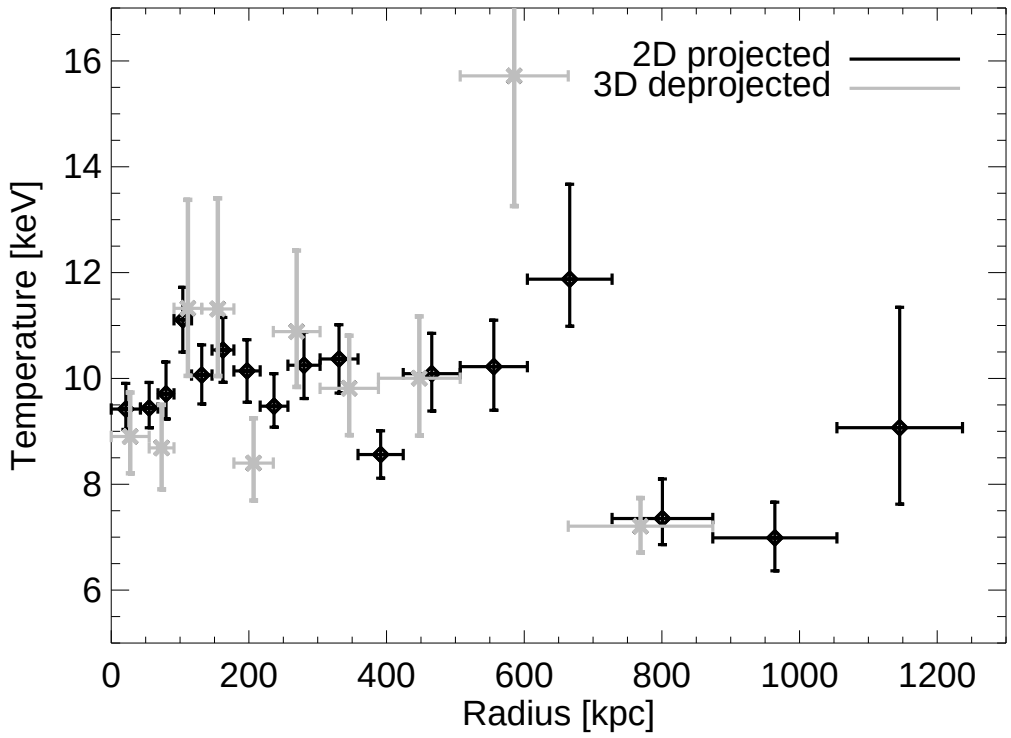

Figure A.4: *The temperature profile reconstructed from the SW symmetric part of Abell 1689. The black diamonds are the 2D projected profile and the grey crosses are the 3D deprojected profile. For the further analysis the 2D projected profiles was used.*

Fitting the complete annuli provides similar temperatures except for the annuli affected by the substructures. In general the reduced χ^2 of the fits are closer to one for the half annuli than for the complete annuli.

Since the observed X-ray emission is a superposition of gas shells of different temperatures we proceeded to deproject the temperature profile of Abell 1689 using ten half-circular bins, each containing at least 45000 counts. Using Xspec, the spectra and response matrices for all bins were fitted simultaneously to the same plasma model as for the 2D temperature profile, but now combined with the *projct* command, which accounts for the projection effects performing a 3D to 2D projection of prolate shell annuli. Each shell are assumed to have its own temperature and all the temperatures are allowed to vary independently. Spherical symmetry of the SW part was assumed as supported by the hardness ratio maps. The deprojected (3D) temperature profile is shown in Fig. A.4 as grey crosses.

The two temperature profiles are quite similar and for that reason, we have reconstructed the mass profile from the 2D projected temperature profile.

A.2.6 X-RAY ANALYSIS AND RESULTS: MASS PROFILE

Assuming the SW part of Abell 1689 to be one half of a spherical symmetric cluster in hydrostatic equilibrium, the 2D projected temperatures can be used to determine a mass profile following the procedure described in Voigt & Fabian (2006). The method is based on the hydrostatic mass equation (Sarazin 1988):

$$M_{3D}(< r) = -\frac{k_b T_g(r) r}{G\mu m_p}\left(\frac{d\ln(T_g(r))}{d\ln(r)} + \frac{d\ln(\rho_g(r))}{d\ln(r)}\right), \tag{A.1}$$

where k_B is the Boltzmann constant, G is the gravitational constant, μ is the mean particle weight weighted by the proton mass m_p. T_g is the gas temperature as a function of radius, and ρ_g is the gas density as function of radius, which can be found from the normalisation of the fitted plasma model. The resulting 3D mass profile of the SW part is shown in Fig. A.5 (black). The errors bars are determined by standard error propagation.

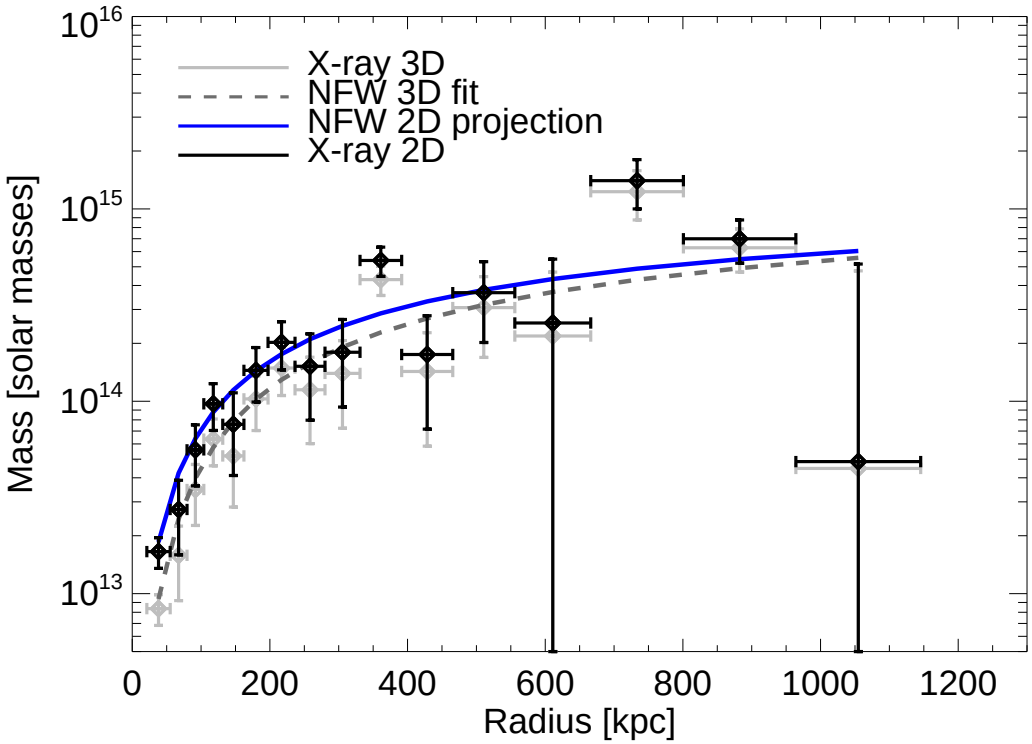

Figure A.5: *The 3D X-ray mass profile (grey diamonds). The fitted NFW profile is shown as a grey dashed line, and the projected 2D NFW profile as a blue solid line. The 2D projected X-ray mass profile i shown as black diamonds.*

A.2.7 X-RAY ANALYSIS AND RESULTS: NFW FIT AND PROJECTION

The mass profile determined from X-rays describes the 3D matter distribution. However the mass profiles from gravitational lensing (described in Sec. A.3.1) are 2D projected profiles, so in order to compare the two profiles, we need to project the X-ray profile as well. It is most easily done by projecting the density along line of sight, and then integrate along the projected radius, R (Sarazin 1988):

$$M_{2D}(< R) = \int_0^R 2\pi R' \int_{R'}^{\infty} \frac{\rho_{tot}(r) r}{\sqrt{r^2 - R'^2}} dr dR' \,. \tag{A.2}$$

If we naively calculate the density profile from the discrete X-ray mass profile, it becomes unphysical with negative densities because of the fluctuations in the mass (even if the uncertainties are taken into account). Instead we have investigated how large the projection effect is for different analytical density profiles. The projection mainly affects the inner part of the mass profile by a factor of up to two, and leave the outer parts effectively unchanged. In the very central parts of the cluster, the projection depends on the cuspiness of the chosen profile. However, the X-ray mass profile does not probe the central part in great detail and the chosen profile is required to reproduce the observed 3D mass profile by fitting, so we have chosen to use an NFW profile (Navarro et al. 1996). The 3D NFW integrated mass profile was fitted to the 3D X-ray mass profile using reduced χ^2 statistics. The best fit is shown as a dashed grey line in Fig. A.5 and has the following parameters: $r_s = 174 \pm 10$ kpc, $\rho_0 = (7.79 \pm 0.02) \times 10^6\,\mathrm{M}_\odot/\mathrm{kpc}^3$, $c_{200} = 5.6$ for a reduced $\chi^2 = 1.6$ (13 degrees of freedom) consistent with earlier published results (Lemze et al. 2007). The NFW profile was projected using Eqn. A.2 and the obtained 2D profile was divided by the 3D profile to achieve a radius-dependent projection factor, which ranged from approx. two in the centre of the cluster to one in the the outer parts. Each point in the 3D X-ray mass profile was converted to a 2D mass profile by multiplying with the projection factor at the corresponding radius. Fig. A.5 shows the 3D profile as grey diamonds, the fitted NFW profile as a grey dashed line, the projected 2D NFW profile as a blue solid line, and the corrected 2D X-ray mass profile as black diamonds. The one σ error bars were correspondingly corrected.

A.2.8 X-RAY ANALYSIS AND RESULTS: THE NE REGION

The NE region is dominated by soft photons (see Sec. A.2.4) and for that reason expected to be colder than the SW region. Fitting a single temperature component plasma model (same model as above) to the spectrum of the region within the white circle in Fig. A.3 gives a temperature of 9.3 ± 0.9 keV (reduced $\chi^2 = 0.97$ for 129 d.o.f.). This is slightly colder than the corresponding SW part of the cluster, which has a temperature of 11.1 ± 0.6 keV (reduced $\chi^2 = 1.02$ for 707 d.o.f.) at similar distance to the centre. The emission from the region is assumed to be a combination of the emission from the SW spherical component plus some softer component.

We have attempted to determine the temperature of the NE component, by fitting a two temperature model to the spectrum of the NE region. One of the temperatures was fixed to the temperature of the spherical component at the same distance (11.1 keV) while the other temperature was a free parameter of the fit. We obtained a cold component temperature of 1.3 ± 1.0 keV (reduced $\chi^2 = 0.92$ for 128 d.o.f.) with a normalisation of 9% of the normalisation of the warm component. Mazzotta et al. (2004) demonstrates that in general it is very hard to disentangle two temperature components with equal normalisation unless in the case where one temperature is around 10 keV and the other one well below a few keV. Comparing to our scenario, the normalisations are not equal. Therefore we have tested the stability of the

two temperature fit by varying the two temperatures and their fractional normalisation and then fitting for the overall normalisation. This procedure gives similar reduced χ^2 for a range of parameters. For a reduced $\chi^2 < 1.5$ the two temperatures can be varied independently between 4 keV and 14 keV as long as the normalisations stays a free parameter. The conclusion is that the best fit for the NE region is either a two temperature model with a warm and a very cold component or a one temperature model with a temperature slightly lower than the corresponding SW part of the cluster, which is consistent with fitting a one temperature model to a two temperature plasma (Mazzotta et al. 2004).

A.2.9 DISCUSSION OF X-RAY RESULTS

The hardness ratio maps and spectral analysis reveal that Abell 1689 is not spherically symmetric as indicated by the total X-ray image, but rather consists of a spherical main clump centred at the X-ray peak and a softer X-ray emitting substructure to the NE.

The NE substructure is not easily visible in the total X-ray emission. It is because the total cluster X-ray emission is generally dominated by low energy photons almost regardless of gas temperature, which again is dominated by emission from the main cluster. The absolute number of photons leading to the relative difference in the soft to hard photon ratio is simply drowned in the total X-ray emission. However, the substructure is clearly visible in the ratio between the surface brightness profiles of the two halves shown in Fig. A.2.

The substructure visible in the hardness ratio in the upper part of Abell 1689 is consistent with the results from *XMM-Newton* presented by Andersson & Madejski (2004), but it is more distinct in the work presented here.

The symmetric SW part of Abell 1689 has a cool core indicated by the hardness ratio map and by the temperature profile. The cool core has earlier been claimed missing in Abell 1689 (Andersson & Madejski 2004). The cool core indicates, that the SW part of Abell 1689 is in hydrostatic equilibrium (Voigt & Fabian 2006).

The temperature profile obtained from the SW part of the cluster is compared to earlier published X-ray temperature profiles in Fig. A.6. The error bars are smaller than earlier obtained profiles from *Chandra* data (Xue & Wu 2002, Lemze et al. 2007) due to better statistics, and the measurements extend to larger radii due to the use of blank sky background. Only the analysis of *XMM-Newton* data by Andersson & Madejski (2004) has comparable statistics and extension. However the temperature profile obtained in this work is generally slightly warmer which leads to an overall larger mass.

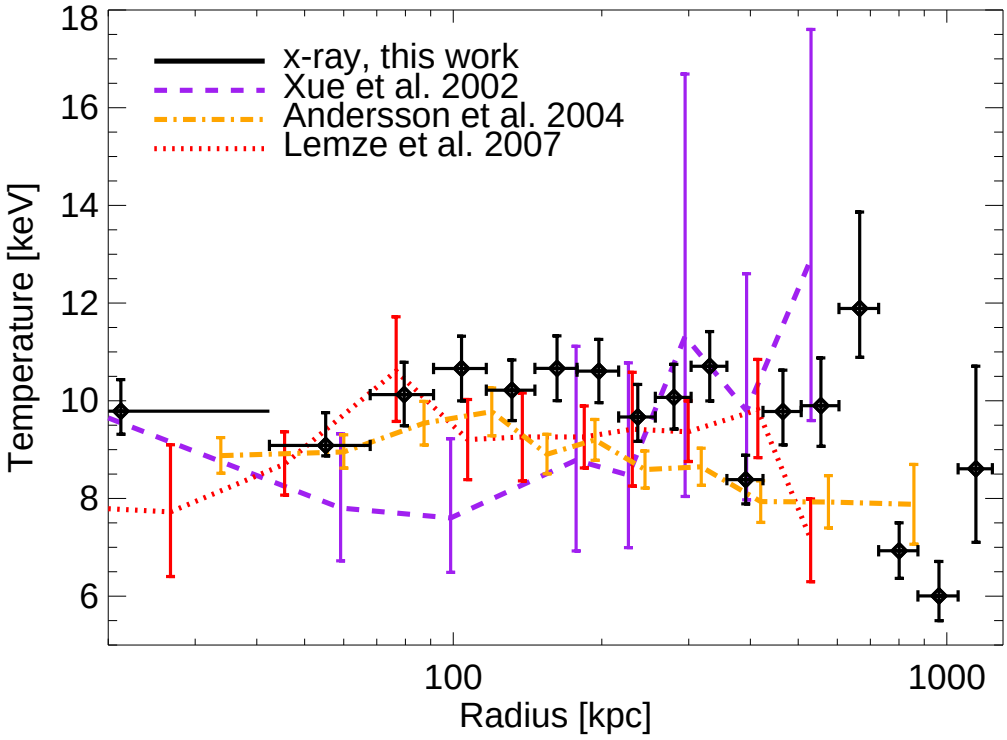

Figure A.6: *The obtained temperature profile compared to earlier results: purple (dashed) from Xue & Wu (2002), orange (dashed dotted) from Andersson & Madejski (2004) (3D deprojected), and red (dotted) from Lemze et al. (2007).*

The X-ray mass profile as inferred from the SW part of the cluster is well fitted by an NFW profile with a concentration parameter of $c_{200} = 5.6$. This values is in better agreement with the value of $c_{200} = 4.7 \pm 1.2$ predicted by Neto et al. (2007) from cosmological simulations, than the value of $c_{200} = 7.6 \pm 1.6$ obtained from gravitational lensing (Limousin et al. 2007) or the value of $c_{200} = 7.7$ from earlier X-ray analyses Andersson & Madejski (2004). This supports our interpretation of the SW part being spherical and in hydrostatic equilibrium.

A.3 ADDITIONAL OBSERVATIONS OF ABELL 1689

A.3.1 STRONG AND WEAK LENSING ANALYSES

We compare our X-ray analysis to strong and weak gravitational lensing analyses of Abell 1689. Strong and weak gravitational lensing are two different methods of determining the mass of the lensing object(s) based on distortions of the images of background sources. Strong lensing is tracing the mass of the lens within the Einstein radius where arcs and multiple images are forming. Weak lensing traces the mass outside the Einstein radius where the gravitational force is weaker, and stretches the images of background objects perpendicular to the direction to the center of the lens. Thus the two methods are valid in different ranges, overlapping only around the Einstein radius.

There have been many strong lensing studies of Abell 1689 (Broadhurst, Takada, Umetsu, Kong, Arimoto, Chiba & Futamase 2005, Broadhurst, Benítez, Coe, Sharon, Zekser, White, Ford, Bouwens, Blakeslee, Clampin, Cross, Franx, Frye, Hartig, Illingworth, Infante, Menanteau, Meurer, Postman, Ardila, Bartko, Brown, Burrows, Cheng, Feldman, Golimowski, Goto, Gronwall, Herranz, Holden, Homeier, Krist, Lesser, Martel, Miley, Rosati, Sirianni, Sparks, Steindling, Tran, Tsvetanov & Zheng 2005, Limousin et al. 2007, Lemze et al. 2007). Here we have used the latest and most detailed by Limousin et al. (2007), which is based on data from the HST Advanced Camera for Surveys (ACS) with the spectroscopic information of the lensed objects in the system from the Keck Telescope and the Very Large Telescope (VLT). The mass reconstruction was done using a Bayesian Monte Carlo Markov Chain method with LENSTOOL (Jullo et al. 2007). The result is an accurate mass mapping of the central parts of Abell 1689, which demonstrates a clear bimodality as shown in Fig. A.7 (black contours). In the very centre there is a main clump associated with the peak of the X-ray emission and then a second significant clump ≈ 180 kpc NE of the centre (A in Fig. A.7) associated with a clump of galaxies (not to be confused with the X-ray structure to the NE, at a distance from ≈ 500 kpc to the centre). Previous studies (Broadhurst, Benítez, Coe, Sharon, Zekser, White, Ford, Bouwens, Blakeslee, Clampin, Cross, Franx, Frye, Hartig, Illingworth, Infante, Menanteau, Meurer, Postman, Ardila, Bartko, Brown, Burrows, Cheng, Feldman, Golimowski, Goto, Gronwall, Herranz, Holden, Homeier, Krist, Lesser, Martel, Miley, Rosati, Sirianni, Sparks, Steindling, Tran, Tsvetanov & Zheng 2005, Halkola et al. 2006) were using fewer spectroscopically confirmed imaged background systems but are in good agreement with the results from Limousin et al. (2007).

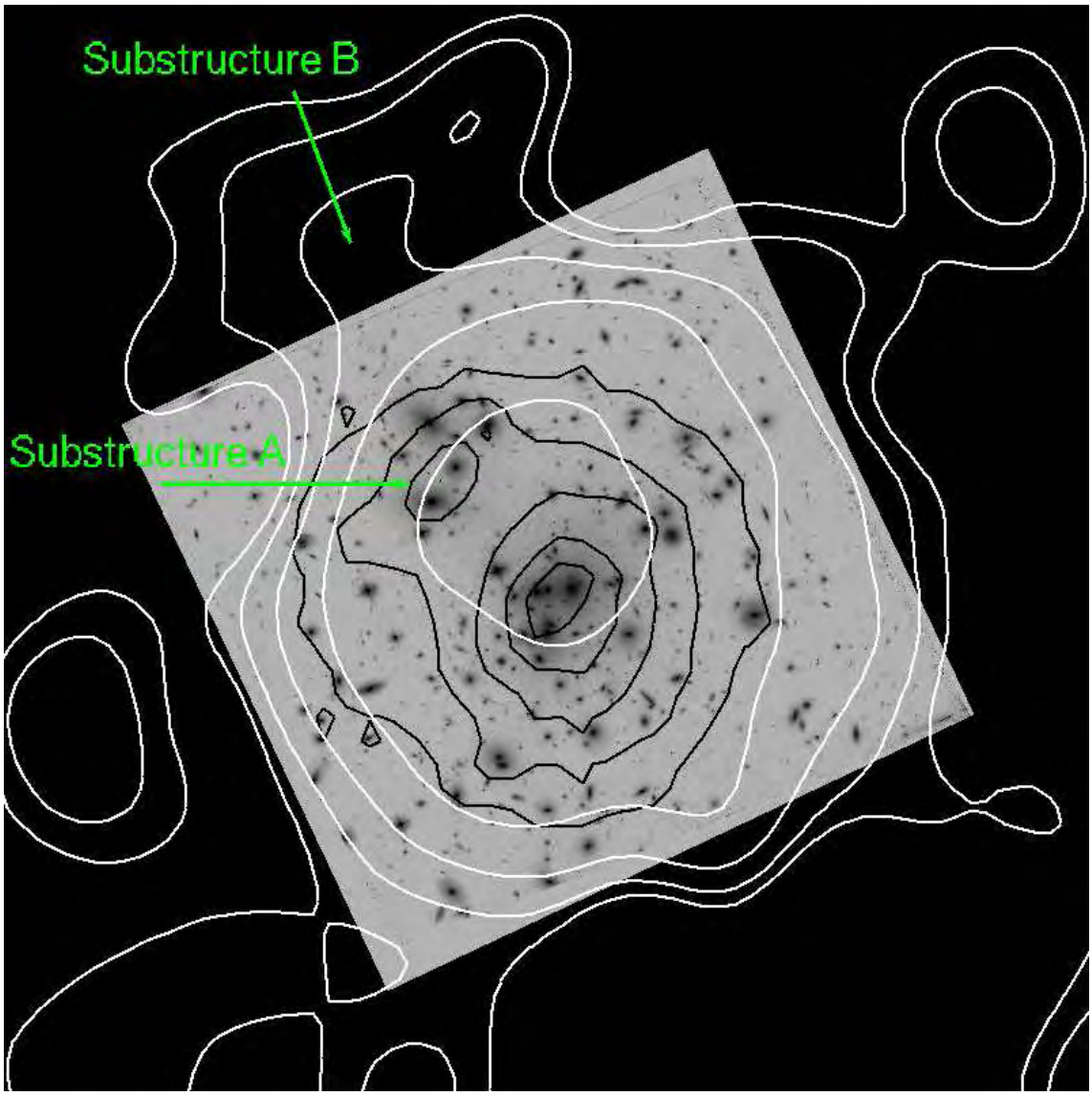

Figure A.7: *Optical images (HST/ACS) with gravitational lensing contours. The black contours are the mass contours from strong lensing. The minimum value is* $10^9\,\mathrm{M}_\odot/''^2$ *and the distance between contours is* $3.5 \times 10^8\,\mathrm{M}_\odot/''^2$*. The strong lensing has a mass peak at the centre of the cluster and a smaller peak* ≈ 180 *kpc to the NE (A). The white contours are the* κ *contours from weak gravitational lensing with a resolution of* $50''$ *(FWHM). The minimum value is* $\kappa = 0.1$ *and the distance between contours is* $\delta\kappa = 0.16$*. The weak lensing contours clearly shows a subclump* ≈ 500 *kpc to the NE of centre (B).*

For weak gravitational lensing we compare to a recent analysis by Dahle et al. (2008), which was based on a mosaic of 16 HST WFPC2 pointings covering the central ~ 1.8 Mpc $\times 1.4$ Mpc of the cluster, complemented at larger radii by ground-based data using the CFH12K mosaic CCD camera at the 3.6 m Canada-France-Hawaii Telescope (CFHT), covering a larger field of 7.7 Mpc $\times$ 5.2 Mpc. This provides a unique mass map with an unprecedented combination of spatial resolution ($50''$) and a large spatial extension. The surface mass density map from weak gravitational lensing shown in Fig. A.7 (white) was reconstructed by Dahle et al. (2008) using the Kaiser et al. (1995) method. This method relies on the fact that the convergence and the two components of the shear are linear combinations of the second derivative of the effective lensing potential. Using Fourier transformation of the convergence and the shear, one can obtain linear relations between the transformed components and determine the mass. The mass contours clearly shows a non-spherical morphology of Abell 1689 at ≈ 500 kpc from the centre (B in Fig. A.8).

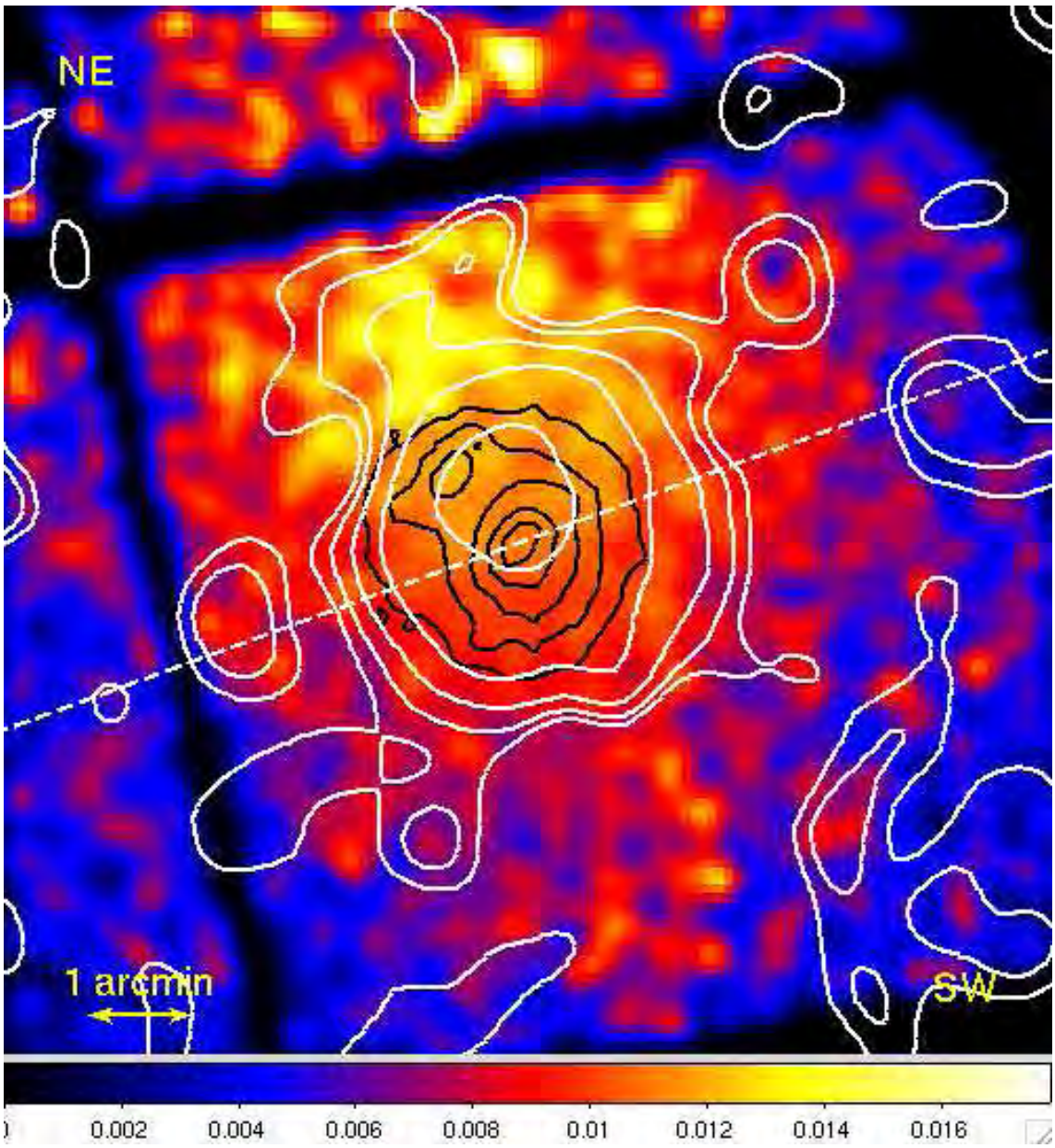

Figure A.8: *The hardness ratio maps with energy splitting of* 1.0 *keV (S/H = E[0.3-1.0 keV]/E[1.0-10.0 keV]). Bright is soft photon excess. The white line divides the cluster into the NE (upper) part and the SW (lower) symmetric part. The contours are identical to Fig. A.7 with white being weak gravitational lensing and black strong gravitational lensing.*

A.3.2 LENSING ANALYSIS: MASS PROFILES

From weak lensing the one dimensional radial mass profile was obtained using aperture mass densitometry (Kaiser 1995, Clowe et al. 2000, Fahlman et al. 1994). This method determines the mean surface mass density within an aperture minus the mean density in a surrounding annulus. Hence, a lower limit to the projected mass of the lens inside the aperture can be found. The degree of underestimation of the true enclosed mass depends on the inner and outer radii and the slope of the projected mass density profile. For realistic projected density profiles (steeper than r^{-1} at large radii) the mass results presented here will be underestimated by less than 30% at all radii.

For strong gravitational lensing the mass map was integrated in radial bins of $1''$ centered on the peak of the X-ray emission (which coincides with the strong lensing mass peak).

For both weak and strong lensing we reconstructed two different radial mass profiles: one by integrating the whole surface density map and the other by integrating the SW half of the surface density map as in the X-ray analysis (but multiplied by two to get a complete sphere).

A.3.3 LENSING RESULTS AND DISCUSSION

Both strong and weak lensing analyses show that Abell 1689 is not spherical, but has substructure in the NE direction on both small (≈ 180 kpc) and large scales (≈ 500 kpc).

The mass profiles of the SW part of Abell 1689 obtained from gravitational lensing are shown in Fig. A.9. The mass profiles were plotted keeping in mind that the strong lensing mass map is valid within the Einstein radius, which for Abell 1689 is $45\,''\approx 139$ kpc. The dashed curves in Fig. A.9 are the integration of the whole mass map and the solid curves are the integration of the SW part only, but multiplied by a factor of two to get a full sphere.

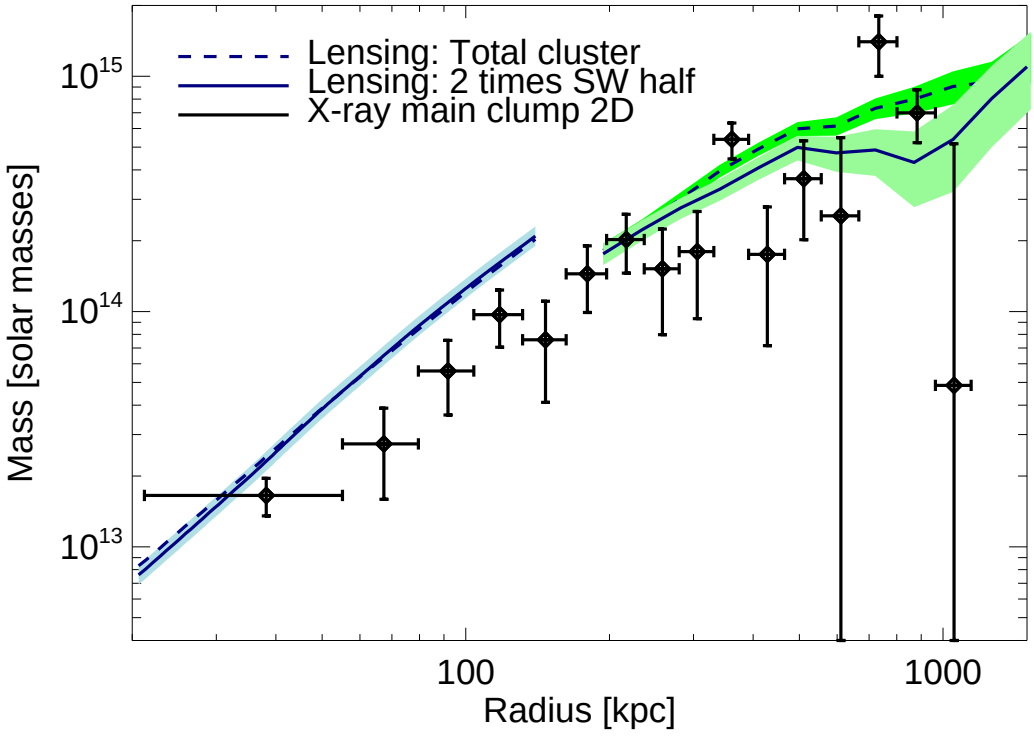

Figure A.9: *The 2D projected mass profile reconstructed from X-ray (black), strong gravitational lensing (blue) and weak gravitational lensing (green). The dashed lensing profile is for integration over the full cluster and the lower solid curve is for integration over the SW part multiplied by two (in order to get a full sphere). The width of the shaded regions corresponds to the one sigma errors on the lensing profiles.*

For the strong lensing, the mass profile integrated over the total cluster is very similar to the mass obtained by integrating the SW part only since the NE substructure at ≈ 180 kpc is negligible compared to the total mass of the cluster. For the weak lensing, the difference is a bit smaller and the total integration gives a larger value due to the NE substructure also seen in the X-rays. The total mass within 1200 kpc is $\approx 9 \times 10^{14}\ \mathrm{M}_{\odot}$.

The mass of the weak lensing substructure is determined to be $1.25 \pm 0.3 \times 10^{14}\,\mathrm{M}_{\odot}$ within $1'.56$.

In Fig. A.10 the total cluster mass profile is compared to earlier studies of Abell 1689 with weak gravitational lensing. It is seen that there is good agreement between the strong lensing mass profiles for radii smaller than 100 kpc. Above 100 kpc, the profile of Dahle et al. (2008) is slightly lower than the earlier profiles (Broadhurst, Takada, Umetsu, Kong, Arimoto, Chiba & Futamase 2005, Halkola et al. 2007, Umetsu & Broadhurst 2007).

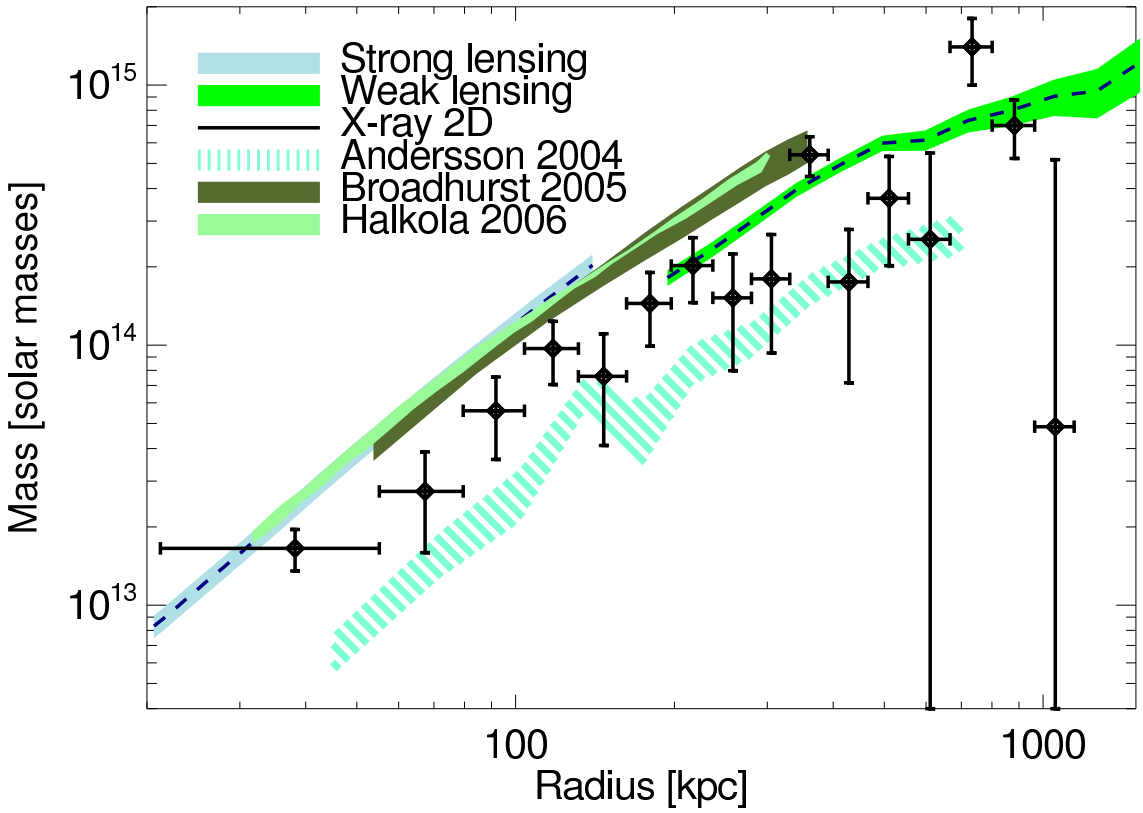

Figure A.10: *The weak and strong gravitational mass profiles (dashed navy) of the total cluster compared to earlier results by Broadhurst, Takada, Umetsu, Kong, Arimoto, Chiba & Futamase (2005) (olive green) and Halkola et al. (2007) (green). Also the X-ray mass profile obtained here is shown (black crosses) together with the one obtained by Andersson & Madejski (2004) (aquamarine dashed).*

Assuming the strong lensing mass profile to be the actual 2D projected mass profile of the inner part of Abell 1689 and the X-ray profile to be the actual 3D profile allows us to constrain the 3D to 2D projection factor as a function of radius, which depends on the cuspiness of the mass profile. The maximally allowed projection factors are $M_{2D}/M_{3D} = (2.8, 4.2, 3.1, 2.6)$ for radii of $r = (38, 67, 92, 188)$ kpc, which are all larger than the factors determined from the NFW profile projection in Sec. A.2.7.

A.3.4 REDSHIFT DISTRIBUTION OF CLUSTER GALAXIES

The redshift distribution of the galaxies within Abell 1689 is overall Gaussian (Duc et al. 2002, Teague et al. 1990, Czoske 2002), but with irregularities (Łokas et al. 2006). The full width at half maximum of the main structure is $\Delta z = 0.02$ corresponding to a line of sight velocity dispersion of ≈ 2500 km/s. This is in contrast to other clusters where very few rich clusters have been found with a velocity dispersion above $1000 - 1200$ km/s. It suggests either that Abell 1689 is not in hydrostatic equilibrium or it is a structure with several clumps along the line of sight. The latter interpretation is favoured by Girardi et al. (1997) and by Łokas et al. (2006) who compared the velocity distribution of Abell 1689 to simulations and argued that the high velocity dispersion is due to several clumps along the line of sight. Removing what they found to be separate unbound structures, they got a total dynamical mass of $2 \times 10^{15}\,\mathrm{M}_{\odot}$ within 3.5 Mpc.

Also Lemze et al. (2008) have studied the dynamics of Abell 1689. They derived the virial mass of the cluster to be $1.73 \pm 0.59 \times 10^{15}\,\mathrm{M}_{\odot}$ using the velocity caustics of the cluster galaxies.

A.4 DISCUSSION

Comparing the X-ray hardness ratio maps with the weak and strong gravitational lensing mass maps (Fig. A.8) we see a coincidence between the substructure in the X-ray emission and the bimodality in the lensing maps. The total X-ray emission (Fig. A.1) features a slight elongation along the same axis as the secondary clump in the strong lensing map. Further from the centre, the position of the NE substructure in the hardness ratio map coincides with the position of a large substructure in the weak lensing map. On the opposite site, the SW part of the cluster appears circular and symmetric in all observations. From this we conclude that Abell 1689 consist of a spherical main clump and some substructure to the NE, which is interfering with the emission from the NE half of the main clump.

The NE half of the cluster is slightly brighter than the SW half at the distance of the weak lensing substructure (Fig. A.2).

The mass of the substructure is $1.25 \pm 0.3 \times 10^{14}\,\mathrm{M}_{\odot}$ within a radius of $1'.56$ determined from weak lensing. This is only a small fraction of the total cluster mass. The gas mass within the same radius has been estimated assuming sphericity and uniform gas density. The result of $\approx 9.7 \pm 0.3 \times 10^{12}\,\mathrm{M}_{\odot}$ only contributes with a very small fraction to the total cluster mass. Nonetheless the X-ray emission from the substructure is bright enough to introduce a complication of the spectral analysis and thereby potentially introduce a mis-interpretation of the temperature of the cluster.

Reconstructing mass profiles from the SW half of the main clump only leads to unprecedentedly good agreement between weak and strong gravitational lensing, and the 2D projected X-ray mass profile, which supports the interpretation of Abell 1689 consisting of a spherical main clump and substructure to the NE.

We have quantified the deviation between the different mass profiles by comparing the relevant part of the 2D projected X-ray mass profile to the weak and strong lensing profiles separately. The values of one profile were compared to a linear interpolation of the other profile. The reduced χ^2 was determined to be 1.8 (four degrees of freedom) for the weak lensing and X-ray comparison and 1.2 (10 degrees of freedom) for comparison of the strong lensing to the X-ray mass profile.

The cool core indicates that Abell 1689 is not a recent merger and supports the claim that the SW main clump is in hydrostatic equilibrium. It indicates that the NE substructure is not leftovers from an early collision and maybe not gravitationally interacting with the main clump at all. If it is infalling, the merging is in such an early state that the hydrostatic equilibrium of the SW part has not yet been disturbed. The line of sight galaxy velocity distribution supports a scenario with several clumps along the line of sight, where the gas does not interact.

The hardness ratio maps can be used as easy diagnostics for the thermal distribution of the cluster, which is related to any substructure. For Abell 1689 the substructure to the NE is visible in a hardness ratio map with an energy splitting of 1.0 keV and a resolution of $10''$ made from 15 ks of the 6930 observation. Many cluster observations have exposures of the order of 15 ks so we propose to use hardness ratio maps in the selection process of relaxed clusters to be further studied.

In this work we have taken advantage of high quality X-ray and gravitational lensing data, which have improved the agreement between several mass estimation methods significantly.

A.5 Conclusions

The new X-ray data analysed here and compared with weak and strong gravitational lensing data show that on large scale Abell 1689 appears spherical, in agreement with earlier data. However, both temperature structure and gravitational lensing shows that Abell 1689 contains some substructure to the NE. The main part appears circular and is centered at the peak of the total X-ray emission. Only the SW half is not significantly influenced by other structures. From X-ray hardness ratio maps and temperature profile it is seen that the SW part features a cool core. The NE substructure is seen in the weak gravitational lensing mass map and the X-ray hardness ratio maps. It has an excess emission of soft X-ray photons relative to hard photons.

We have determined the mass profile of the spherical main clump of the cluster from X-ray observations and compared to recent gravitational lensing results. The obtained cluster mass within ≈ 875 kpc derived from X-rays alone is $6.4 \pm 2.1 \times 10^{14}\,\mathrm{M}_{\odot}$ compared to a weak lensing mass of $8.6 \pm 3.0 \times 10^{14}\,\mathrm{M}_{\odot}$ within the same radius. The profiles are in very good agreement out to 1200 kpc and the discrepancy between X-ray and lensing mass profiles has been significantly reduced due to high quality data.

Acknowledgments We would like to thank M. Markevitch for useful comments on the background analysis. The Dark Cosmology Centre is funded by the Danish National Research Foundation. KP acknowledges support from Instrument Center for Danish Astrophysics. ML acknowledges support from the Agence Nationale de la Recherche (France) project nř BLAN06-3_135448. HD acknowledges support from the Research Council of Norway

BIBLIOGRAPHY

Alam, S. M. K. & Ryden, B. S. (2002), 'The Shapes of Galaxies in the Sloan Digital Sky Survey', ApJ **570**, 610–617.

An, J. H. & Evans, N. W. (2006), 'Galaxy Models with Tangentially Anisotropic Velocity Distributions', AJ **131**, 782–789.

Andersson, K. E. & Madejski, G. M. (2004), 'Complex Structure of Galaxy Cluster A1689: Evidence for a Merger from X-Ray Data?', ApJ **607**, 190–201.

Andersson, K., Peterson, J. R. & Madejski, G. (2007), 'Application of an XMM-Newton EPIC Monte Carlo Technique to Analysis and Interpretation of Data for the Abell 1689, RX J0658-55, and Centaurus Clusters of Galaxies', ApJ **670**, 1010–1026.

Arnaud, K., Dorman, B. & Gordon, C. (2007), *An X-Ray Spectral Fitting Package - User's Guide for version 12.4.0* .

Auger, M. W., Fassnacht, C. D., Wong, K. C., Thompson, D., Matthews, K. & Soifer, B. T. (2008), 'Lens Galaxy Properties of SBS 1520+530: Insights from Keck Spectroscopy and AO Imaging', ApJ **673**, 778–786.

Bade, N., Siebert, J., Lopez, S., Voges, W. & Reimers, D. (1997), 'RX J0911.4+0551: A new multiple QSO selected from the ROSAT All-Sky Survey.', A&A **317**, L13–L16.

Bak, J. & Statler, T. S. (2000), 'The Intrinsic Shape Distribution of a Sample of Elliptical Galaxies', AJ **120**, 110–122.

Barkana, R. (1997), 'Analysis of Time Delays in the Gravitational Lens PG 1115+080', ApJ **489**, 21–+.

Barnabè, M., Czoske, O., Koopmans, L. V. E., Treu, T., Bolton, A. S. & Gavazzi, R. (2009), 'Two-dimensional kinematics of SLACS lenses - II. Combined lensing and dynamics analysis of early-type galaxies at z = 0.08-0.33', MNRAS pp. 1239–+.

Barnes, J. E. (1988), 'Encounters of disk/halo galaxies', ApJ **331**, 699–717.

Bernstein, G. & Fischer, P. (1999), 'Values of H_0 from Models of the Gravitational Lens 0957+561', AJ **118**, 14–34.

Branch, D., Fisher, A., Baron, E. & Nugent, P. (1996), 'On van den Bergh's Method for Measuring the Hubble Constant from Type IA Supernovae', ApJ **470**, L7+.

Broadhurst, T., Benítez, N., Coe, D., Sharon, K., Zekser, K., White, R., Ford, H., Bouwens, R., Blakeslee, J., Clampin, M., Cross, N., Franx, M., Frye, B., Hartig, G., Illingworth, G., Infante, L., Menanteau, F., Meurer, G., Postman, M., Ardila, D. R., Bartko, F., Brown, R. A., Burrows, C. J., Cheng, E. S., Feldman, P. D., Golimowski, D. A., Goto, T., Gronwall, C., Herranz, D., Holden, B., Homeier, N., Krist, J. E., Lesser, M. P., Martel, A. R., Miley, G. K., Rosati, P., Sirianni, M., Sparks, W. B., Steindling, S., Tran, H. D., Tsvetanov, Z. I. & Zheng, W. (2005), 'Strong-Lensing Analysis of A1689 from Deep Advanced Camera Images', ApJ **621**, 53–88.

Broadhurst, T., Takada, M., Umetsu, K., Kong, X., Arimoto, N., Chiba, M. & Futamase, T. (2005), 'The Surprisingly Steep Mass Profile of A1689, from a Lensing Analysis of Subaru Images', ApJ **619**, L143–L146.

Browne, I. W. A., Patnaik, A. R., Walsh, D. & Wilkinson, P. N. (1993), 'The Redshift of the Lensing Galaxy in the Gravitationally Lensed System B:0218+35.7', MNRAS **263**, L32+.

Burud, I., Courbin, F., Lidman, C., Jaunsen, A. O., Hjorth, J., Ostensen, R., Andersen, M. I., Clasen, J. W., Wucknitz, O., Meylan, G., Magain, P., Stabell, R. & Refsdal, S. (1998), 'High-Resolution Optical and Near-Infrared Imaging of the Quadruple Quasar RX J0911.4+0551', ApJ **501**, L5+.

Burud, I., Courbin, F., Magain, P., Lidman, C., Hutsemékers, D., Kneib, J.-P., Hjorth, J., Brewer, J., Pompei, E., Germany, L., Pritchard, J., Jaunsen, A. O., Letawe, G. & Meylan, G. (2002), 'An optical time-delay for the lensed BAL quasar HE 2149-2745', A&A **383**, 71–81.

Burud, I., Hjorth, J., Courbin, F., Cohen, J. G., Magain, P., Jaunsen, A. O., Kaas, A. A., Faure, C. & Letawe, G. (2002*a*), 'Time delay and lens redshift for the doubly imaged BAL quasar SBS 1520+530', A&A **391**, 481–486.

Burud, I., Hjorth, J., Courbin, F., Cohen, J. G., Magain, P., Jaunsen, A. O., Kaas, A. A., Faure, C. & Letawe, G. (2002*b*), 'Time delay and lens redshift for the doubly imaged BAL quasar SBS 1520+530', A&A **391**, 481–486.

Burud, I., Hjorth, J., Jaunsen, A. O., Andersen, M. I., Korhonen, H., Clasen, J. W., Pelt, J., Pijpers, F. P., Magain, P. & Østensen, R. (2000), 'An Optical Time Delay Estimate for the Double Gravitational Lens System B1600+434', ApJ **544**, 117–122.

Carilli, C. L. & Rawlings, S. (2004), 'Motivation, key science projects, standards and assumptions', *New Astronomy Review* **48**, 979–984.

Carilli, C. L., Rupen, M. P. & Yanny, B. (1993), 'Neutral hydrogen 21 centimeter absorption at Z = 0.6847 toward the 'smallest Einstein ring'', ApJ **412**, L59–L62.

Chandra X-ray Centre Proposers' Observatory Guide, chapter 9 (2007), *http://cxc.harvard.edu/proposers/POG/html* .

Chang, K. & Refsdal, S. (1979), 'Flux variations of QSO 0957+561 A, B and image splitting by stars near the light path', Nature **282**, 561–564.

Chavushyan, V. H., Vlasyuk, V. V., Stepanian, J. A. & Erastova, L. K. (1997), 'SBS 1520+530: a new gravitationally lensed system at z=1.855.', A&A **318**, L67–L70.

Chengalur, J. N., de Bruyn, A. G. & Narasimha, D. (1999), 'HI and OH absorption at z=0.89', A&A **343**, L79–L82.

Claeskens, J.-F., Sluse, D., Riaud, P. & Surdej, J. (2006), 'Multi wavelength study of the gravitational lens system RXS J1131-1231. II. Lens model and source reconstruction', A&A **451**, 865–879.

Clowe, D., Luppino, G. A., Kaiser, N. & Gioia, I. M. (2000), 'Weak Lensing by High-Redshift Clusters of Galaxies. I. Cluster Mass Reconstruction', ApJ **539**, 540–560.

Coe, D. & Moustakas, L. (2009), 'Cosmological Constraints from Gravitational Lens Time Delays', *ArXiv e-prints* .

Cohen, A. S., Hewitt, J. N., Moore, C. B. & Haarsma, D. B. (2000), 'Further Investigation of the Time Delay, Magnification Ratios, and Variability in the Gravitational Lens 0218+357', ApJ **545**, 578–590.

Cohen, J. G., Lawrence, C. R. & Blandford, R. D. (2003), 'The Redshift of the Lensed Object in the Einstein Ring B0218+357', ApJ **583**, 67–69.

Coles, J. (2008), 'A New Estimate of the Hubble Time with Improved Modeling of Gravitational Lenses', ApJ **679**, 17–24.

Courbin, F. (2003), 'Quasar Lensing: the Observer's Point of View', *ArXiv Astrophysics e-prints* .

Czoske, O. (2002), Wide-field observations of clusters of galaxies, PhD thesis, Université Paul Sabatier, Toulouse III, France.

Dahle, H. et al. (2008), *in preparation* .

Dalal, N. & Kochanek, C. S. (2002), 'Direct Detection of Cold Dark Matter Substructure', ApJ **572**, 25–33.

Davies, R. L., Efstathiou, G., Fall, S. M., Illingworth, G. & Schechter, P. L. (1983), 'The kinematic properties of faint elliptical galaxies', ApJ **266**, 41–57.

de Vries, W. H., Becker, R. H. & White, R. L. (2003), 'Long-Term Variability of Sloan Digital Sky Survey Quasars', AJ **126**, 1217–1226.

de Vries, W. H., Becker, R. H. & White, R. L. (2006), Long-Term Optical Quasar Variability, *in* C. M. Gaskell, I. M. McHardy, B. M. Peterson & S. G. Sergeev, eds, 'Astronomical Society of the Pacific Conference Series', Vol. 360 of *Astronomical Society of the Pacific Conference Series*, pp. 29–+.

Djorgovski, S. & Davis, M. (1987), 'Fundamental properties of elliptical galaxies', ApJ **313**, 59–68.

Dobke, B. M., King, L. J., Fassnacht, C. D. & Auger, M. W. (2009), 'Estimating cosmological parameters from future gravitational lens surveys', MNRAS **397**, 311–319.

Dressler, A. (1980), 'Galaxy morphology in rich clusters - Implications for the formation and evolution of galaxies', ApJ **236**, 351–365.

Dressler, A., Lynden-Bell, D., Burstein, D., Davies, R. L., Faber, S. M., Terlevich, R. & Wegner, G. (1987), 'Spectroscopy and photometry of elliptical galaxies. I - A new distance estimator', ApJ **313**, 42–58.

Dubinski, J. (1998), 'The Origin of the Brightest Cluster Galaxies', ApJ **502**, 141–+.

Duc, P.-A., Poggianti, B. M., Fadda, D., Elbaz, D., Flores, H., Chanial, P., Franceschini, A., Moorwood, A. & Cesarsky, C. (2002), 'BVR photometry in Abell 1689 (Duc+, 2002)', *VizieR Online Data Catalog* **338**, 20060–+.

Eigenbrod, A., Courbin, F., Meylan, G., Vuissoz, C. & Magain, P. (2006*a*), 'COSMOGRAIL: the COSmological MOnitoring of GRAvItational Lenses. III. Redshift of the lensing galaxy in eight gravitationally lensed quasars', A&A **451**, 759–766.

Eigenbrod, A., Courbin, F., Meylan, G., Vuissoz, C. & Magain, P. (2006*b*), 'COSMOGRAIL: the COSmological MOnitoring of GRAvItational Lenses. III. Redshift of the lensing galaxy in eight gravitationally lensed quasars', A&A **451**, 759–766.

Eisenstein, D. J., Zehavi, I., Hogg, D. W., Scoccimarro, R., Blanton, M. R., Nichol, R. C., Scranton, R., Seo, H.-J., Tegmark, M., Zheng, Z., Anderson, S. F., Annis, J., Bahcall, N., Brinkmann, J., Burles, S., Castander, F. J., Connolly, A., Csabai, I., Doi, M., Fukugita, M., Frieman, J. A., Glazebrook, K., Gunn, J. E., Hendry, J. S., Hennessy, G., Ivezić, Z., Kent, S., Knapp, G. R., Lin, H., Loh, Y.-S., Lupton, R. H., Margon, B., McKay, T. A., Meiksin, A., Munn, J. A., Pope, A., Richmond, M. W., Schlegel, D., Schneider, D. P., Shimasaku, K., Stoughton, C., Strauss, M. A., SubbaRao, M., Szalay, A. S., Szapudi, I., Tucker, D. L., Yanny, B. & York, D. G. (2005), 'Detection of the Baryon Acoustic Peak in the Large-Scale Correlation Function of SDSS Luminous Red Galaxies', ApJ **633**, 560–574.

Elíasdóttir, Á., Hjorth, J., Toft, S., Burud, I. & Paraficz, D. (2006), 'Extinction Curves of Lensing Galaxies out to z = 1', ApJS **166**, 443–469.

Fabbiano, G., Gioia, I. M. & Trinchieri, G. (1989), 'Radio emission and the hot interstellar medium of early-type galaxies', ApJ **347**, 127–143.

Fabian, A. C., Sanders, J. S., Ettori, S., Taylor, G. B., Allen, S. W., Crawford, C. S., Iwasawa, K., Johnstone, R. M. & Ogle, P. M. (2000), 'Chandra imaging of the complex X-ray core of the Perseus cluster', MNRAS **318**, L65–L68.

Fahlman, G., Kaiser, N., Squires, G. & Woods, D. (1994), 'Dark matter in MS 1224 from distortion of background galaxies', ApJ **437**, 56–62.

Falco, E. E., Gorenstein, M. V. & Shapiro, I. I. (1985), 'On model-dependent bounds on H(0) from gravitational images Application of Q0957 + 561A,B', ApJ **289**, L1–L4.

Falco, E. E., Shapiro, I. I., Moustakas, L. A. & Davis, M. (1997), 'An Estimate of H 0 from Keck Spectroscopy of the Gravitational Lens System 0957+561', ApJ **484**, 70–+.

Fassnacht, C. D., Womble, D. S., Neugebauer, G., Browne, I. W. A., Readhead, A. C. S., Matthews, K. & Pearson, T. J. (1996), '1608+656: A Gravitationally Lensed Poststarburst Radio Galaxy', ApJ **460**, L103+.

Fassnacht, C. D., Xanthopoulos, E., Koopmans, L. V. E. & Rusin, D. (2002), 'A Determination of H_0 with the CLASS Gravitational Lens B1608+656. III. A Significant Improvement in the Precision of the Time Delay Measurements', ApJ **581**, 823–835.

Faure, C., Courbin, F., Kneib, J. P., Alloin, D., Bolzonella, M. & Burud, I. (2002), 'The lensing system towards the doubly imaged quasar SBS 1520+530', A&A **386**, 69–76.

Fohlmeister, J., Kochanek, C. S., Falco, E. E., Morgan, C. W. & Wambsganss, J. (2008), 'The Rewards of Patience: An 822 Day Time Delay in the Gravitational Lens SDSS J1004+4112', ApJ **676**, 761–766.

Freedman, W. L., Madore, B. F., Gibson, B. K., Ferrarese, L., Kelson, D. D., Sakai, S., Mould, J. R., Kennicutt, Jr., R. C., Ford, H. C., Graham, J. A., Huchra, J. P., Hughes, S. M. G., Illingworth, G. D., Macri, L. M. & Stetson, P. B. (2001), 'Final Results from the Hubble Space Telescope Key Project to Measure the Hubble Constant', ApJ **553**, 47–72.

Fruscione, A., McDowell, J. C., Allen, G. E., Brickhouse, N. S., Burke, D. J., Davis, J. E., Durham, N., Elvis, M., Galle, E. C., Harris, D. E., Huenemoerder, D. P., Houck, J. C., Ishibashi, B., Karovska, M., Nicastro, F., Noble, M. S., Nowak, M. A., Primini, F. A., Siemiginowska, A., Smith, R. K. & Wise, M. (2006), CIAO: Chandra's data analysis system, *in* 'Society of Photo-Optical Instrumentation Engineers (SPIE) Conference Series', Vol. 6270 of *Presented at the Society of Photo-Optical Instrumentation Engineers (SPIE) Conference*.

Fukugita, M., Futamase, T. & Kasai, M. (1990), 'A Possible Test for the Cosmological Constant with Gravitational Lenses', MNRAS **246**, 24P–+.

Gerhard, O., Kronawitter, A., Saglia, R. P. & Bender, R. (2001), 'Dynamical Family Properties and Dark Halo Scaling Relations of Giant Elliptical Galaxies', AJ **121**, 1936–1951.

Girardi, M., Fadda, D., Escalera, E., Giuricin, G., Mardirossian, F. & Mezzetti, M. (1997), 'New Optical Insights into the Mass Discrepancy of Galaxy Clusters: The Cases of A1689 and A2218', ApJ **490**, 56–+.

Golse, G. & Kneib, J.-P. (2002), 'Pseudo elliptical lensing mass model: Application to the NFW mass distribution', A&A **390**, 821–827.

Gorenstein, M. V., Shapiro, I. I. & Falco, E. E. (1988), 'Degeneracies in parameter estimates for models of gravitational lens systems', ApJ **327**, 693–711.

Grillo, C., Lombardi, M. & Bertin, G. (2008), 'Cosmological parameters from strong gravitational lensing and stellar dynamics in elliptical galaxies', A&A **477**, 397–406.

Guimarães, A. C. C. & Sodré, L. J. (2009), 'Density profile and line-of-sight mass contamination of SLACS gravitational lenses', *ArXiv e-prints* .

Halkola, A., Seitz, S. & Pannella, M. (2006), 'Parametric strong gravitational lensing analysis of Abell 1689', MNRAS **372**, 1425–1462.

Halkola, A., Seitz, S. & Pannella, M. (2007), 'The Sizes of Galaxy Halos in Galaxy Cluster Abell 1689', ApJ **656**, 739–745.

Hansen, S. H. & Moore, B. (2006), 'A universal density slope Velocity anisotropy relation for relaxed structures', *New Astronomy* **11**, 333–338.

HeaSoft (2007), *http://heasarc.gsfc.nasa.gov* .

Hinshaw, G. et al. (2008), 'Five-Year Wilkinson Microwave Anisotropy Probe (WMAP) Observations: Data Processing, Sky Maps, and Basic Results', *preprint, arXiv:0803.0732 [astro-ph]* .

Hjorth, J., Burud, I., Jaunsen, A. O., Schechter, P. L., Kneib, J.-P., Andersen, M. I., Korhonen, H., Clasen, J. W., Kaas, A. A., Østensen, R., Pelt, J. & Pijpers, F. P. (2002), 'The Time Delay of the Quadruple Quasar RX J0911.4+0551', ApJ **572**, L11–L14.

Holden, B. P., Franx, M., Illingworth, G. D., Postman, M., van der Wel, A., Kelson, D. D., Blakeslee, J. P., Ford, H., Demarco, R. & Mei, S. (2009), 'The Ellipticities of Cluster Early-type Galaxies from z ˜ 1 to z ˜ 0: No Evolution in the Overall Distribution of Bulge-to-Disk Ratios', ApJ **693**, 617–633.

Holder, G. P. & Schechter, P. L. (2003), 'External Shear in Quadruply Imaged Lens Systems', ApJ **589**, 688–692.

Hulse, R. A. & Taylor, H. J. (1974), Discovery of a Pulsar in a Close Binary System., *in* 'Bulletin of the American Astronomical Society', Vol. 6 of *Bulletin of the American Astronomical Society*, pp. 453–+.

Humphrey, P. J. & Buote, D. A. (2009), 'The slope of the mass profile and the tilt of the fundamental plane in early-type galaxies', *ArXiv e-prints* .

Impey, C. D., Falco, E. E., Kochanek, C. S., Lehár, J., McLeod, B. A., Rix, H.-W., Peng, C. Y. & Keeton, C. R. (1998), 'An Infrared Einstein Ring in the Gravitational Lens PG 1115+080', ApJ **509**, 551–560.

Inada, N., Oguri, M., Becker, R. H., White, R. L., Gregg, M. D., Schechter, P. L., Kawano, Y., Kochanek, C. S., Richards, G. T., Schneider, D. P., Barentine, J. C., Brewington, H. J., Brinkmann, J., Harvanek, M., Kleinman, S. J., Krzesinski, J., Long, D., Neilsen, Jr., E. H., Nitta, A., Snedden, S. A. & York, D. G. (2006), 'SDSS J0806+2006 and SDSS J1353+1138: Two New Gravitationally Lensed Quasars from the Sloan Digital Sky Survey', AJ **131**, 1934–1941.

Inada, N., Oguri, M., Pindor, B., Hennawi, J. F., Chiu, K., Zheng, W., Ichikawa, S.-I., Gregg, M. D., Becker, R. H., Suto, Y., Strauss, M. A., Turner, E. L., Keeton, C. R., Annis, J., Castander, F. J., Eisenstein, D. J., Frieman, J. A., Fukugita, M., Gunn, J. E., Johnston, D. E., Kent, S. M., Nichol, R. C., Richards, G. T., Rix, H.-W., Sheldon, E. S., Bahcall, N. A., Brinkmann, J., Ivezić, Ž., Lamb, D. Q., McKay, T. A., Schneider, D. P. & York, D. G. (2003), 'A gravitationally lensed quasar with quadruple images separated by 14.62arcseconds', Nature **426**, 810–812.

Ivezic, Z., Tyson, J. A., Allsman, R., Andrew, J., Angel, R., Axelrod, T., Barr, J. D., Becker, A. C., Becla, J., Beldica, C., Blandford, R. D., Brandt, W. N., Bullock, J. S., Burke, D. L., Chandrasekharan, S., Chesley, S., Claver, C. F., Connolly, A., Cook, K. H., Cooray, A., Cribbs, C., Cutri, R., Daues, G., Delgado, F., Ferguson, H., Geary, J. C., Gee, P., Gilmore, D. K., Gressler, W. J., Hogan, C., Huffer, M. E., Jacoby,

S. H., Jain, B., Jernigan, J. G., Jones, R. L., Juric, M., Kahn, S. M., Kalirai, J. S., Kantor, J. P., Kirkby, D., Knox, L., Krabbendam, V. L., Krughoff, S., Kulkarni, S., Lambert, R., Levine, D., Liang, M., Lim, K.-T., Lupton, R. H., Marshall, P., Marshall, S., May, M., Miller, M., Mills, D. J., Monet, D. G., Neill, D. R., Nordby, M., O'Connor, P., Oliver, J., Olivier, S. S., Owen, R. E., Peterson, J. R., Petry, C. E., Pierfederici, F., Pietrowicz, S., Pike, R., Pinto, P. A., Plante, R., Radeka, V., Rasmussen, A., Rosing, W., Saha, A., Schalk, T. L., Schindler, R. H., Schneider, D. P., Schumacher, G., Sebag, J., Seppala, L. G., Shipsey, I., Silvestri, N., Smith, J. A., Smith, R. C., Strauss, M. A., Stubbs, C. W., Sweeney, D., Szalay, A., Thaler, J. J., VandenBerk, D., Warner, M., Willman, B., Wittman, D., Wolff, S. C., Wood-Vasey, W. M. & Zhan, H. (2008), 'LSST: from Science Drivers to Reference Design and Anticipated Data Products', *ArXiv e-prints* .

Jackson, N., de Bruyn, A. G., Myers, S., Bremer, M. N., Miley, G. K., Schilizzi, R. T., Browne, I. W. A., Nair, S., Wilkinson, P. N., Blandford, R. D., Pearson, T. J. & Readhead, A. C. S. (1995), '1600+434: a new gravitational lens system', MNRAS **274**, L25–L29.

Jakobsson, P., Hjorth, J., Burud, I., Letawe, G., Lidman, C. & Courbin, F. (2005*a*), 'An optical time delay for the double gravitational lens system FBQ 0951+2635', A&A **431**, 103–109.

Jakobsson, P., Hjorth, J., Burud, I., Letawe, G., Lidman, C. & Courbin, F. (2005*b*), 'An optical time delay for the double gravitational lens system FBQ 0951+2635', A&A **431**, 103–109.

Jaunsen, A. O. & Hjorth, J. (1997), 'Detection of a spiral lens galaxy and optical variability in the gravitational lens system B1600+434.', A&A **317**, L39–L42.

Johnston, D. E., Richards, G. T., Frieman, J. A., Keeton, C. R., Strauss, M. A., Knapp, G. R., Becker, R. H., White, R. L., Johnson, E. T., Ma, Z., SubbaRao, M., Bahcall, N. A., Bernardi, M., Brinkmann, J., Eisenstein, D. J., Fukugita, M., Hall, P. B., Inada, N., Pindor, B., Schlegel, D. J., Scranton, R., Sheldon, E. S., Schneider, D. P., Szalay, A. S. & York, D. G. (2003), 'SDSS J090334.92+502819.2: A New Gravitational Lens', AJ **126**, 2281–2290.

Jones, M. E., Edge, A. C., Grainge, K., Grainger, W. F., Kneissl, R., Pooley, G. G., Saunders, R., Miyoshi, S. J., Tsuruta, T., Yamashita, K., Tawara, Y., Furuzawa, A., Harada, A. & Hatsukade, I. (2005), 'H_0 from an orientation-unbiased sample of Sunyaev-Zel'dovich and X-ray clusters', MNRAS **357**, 518–526.

Jullo, E., Kneib, J.-P., Limousin, M., Elíasdóttir, Á., Marshall, P. J. & Verdugo, T. (2007), 'A Bayesian approach to strong lensing modelling of galaxy clusters', *New Journal of Physics* **9**, 447–+.

Kaiser, N. (1995), 'Nonlinear cluster lens reconstruction', ApJ **439**, L1–L3.

Kaiser, N. (2004), Pan-STARRS: a wide-field optical survey telescope array, *in* J. M. Oschmann Jr., ed., 'Society of Photo-Optical Instrumentation Engineers (SPIE) Conference Series', Vol. 5489 of *Society of Photo-Optical Instrumentation Engineers (SPIE) Conference Series*, pp. 11–22.

Kaiser, N., Squires, G. & Broadhurst, T. (1995), 'A Method for Weak Lensing Observations', ApJ **449**, 460–+.

Keeton, C. R. (2001), 'Computational Methods for Gravitational Lensing', *ArXiv Astrophysics e-prints* .

Keeton, C. R., Kochanek, C. S. & Falco, E. E. (1998), 'The Optical Properties of Gravitational Lens Galaxies as a Probe of Galaxy Structure and Evolution', ApJ **509**, 561–578.

Keeton, C. R., Mao, S. & Witt, H. J. (2000), 'Gravitational Lenses with more than Four Images. I. Classification of Caustics', ApJ **537**, 697–707.

Kneib, J.-P., Cohen, J. G. & Hjorth, J. (2000), 'RX J0911+05: A Massive Cluster Lens at z=0.769', ApJ **544**, L35–L39.

Kochanek, C. S. (1993), 'The Analysis of Gravitational Lens Surveys. II. Maximum Likelihood Models and Singular Potentials', ApJ **419**, 12–+.

Kochanek, C. S., Morgan, N. D., Falco, E. E., McLeod, B. A., Winn, J. N., Dembicky, J. & Ketzeback, B. (2006), 'The Time Delays of Gravitational Lens HE 0435-1223: An Early-Type Galaxy with a Rising Rotation Curve', ApJ **640**, 47–61.

Kochanek, C. S. & Schechter, P. L. (2004), The Hubble Constant from Gravitational Lens Time Delays, *in* W. L. Freedman, ed., 'Measuring and Modeling the Universe', pp. 117–+.

Komatsu, E., Dunkley, J., Nolta, M. R., Bennett, C. L., Gold, B., Hinshaw, G., Jarosik, N., Larson, D., Limon, M., Page, L., Spergel, D. N., Halpern, M., Hill, R. S., Kogut, A., Meyer, S. S., Tucker, G. S., Weiland, J. L., Wollack, E. & Wright, E. L. (2009), 'Five-Year Wilkinson Microwave Anisotropy Probe Observations: Cosmological Interpretation', ApJS **180**, 330–376.

Koopmans, L. V. E., Barnabe, M., Bolton, A., Bradac, M., Ciotti, L., Congdon, A., Czoske, O., Dye, S., Dutton, A., Elliasdottir, A., Evans, E., Fassnacht, C. D., Jackson, N., Keeton, C., Lasio, J., Moustakas, L., Meneghetti, M., Myers, S., Nipoti, C., Suyu, S., van de Ven, G., Vegetti, S., Wucknitz, O. & Zhao, H.-S. (2009), 'Strong Gravitational Lensing as a Probe of Gravity, Dark-Matter and Super-Massive Black Holes', *Astronomy* **2010**, 159–+.

Koopmans, L. V. E., de Bruyn, A. G., Xanthopoulos, E. & Fassnacht, C. D. (2000), 'A time-delay determination from VLA light curves of the CLASS gravitational lens B1600+434', A&A **356**, 391–402.

Koopmans, L. V. E. & the CLASS collaboration (2001), 'The Hubble Constant from (CLASS) Gravitational Lenses', *Publications of the Astronomical Society of Australia* **18**, 179–181.

Koopmans, L. V. E., Treu, T., Bolton, A. S., Burles, S. & Moustakas, L. A. (2006*a*), 'The Sloan Lens ACS Survey. III. The Structure and Formation of Early-Type Galaxies and Their Evolution since z ˜ 1', ApJ **649**, 599–615.

Koopmans, L. V. E., Treu, T., Bolton, A. S., Burles, S. & Moustakas, L. A. (2006*b*), 'The Sloan Lens ACS Survey. III. The Structure and Formation of Early-Type Galaxies and Their Evolution since z ˜ 1', ApJ **649**, 599–615.

Koopmans, L. V. E., Treu, T., Fassnacht, C. D., Blandford, R. D. & Surpi, G. (2003), 'The Hubble Constant from the Gravitational Lens B1608+656', ApJ **599**, 70–85.

Kormann, R., Schneider, P. & Bartelmann, M. (1994), 'Isothermal elliptical gravitational lens models', A&A **284**, 285–299.

Lawrence, C. R., Schneider, D. P., Schmidt, M., Bennett, C. L., Hewitt, J. N., Burke, B. F., Turner, E. L. & Gunn, J. E. (1984), 'Discovery of a New Gravitational Lens System', *Science* **223**, 46–49.

Lehár, J., Falco, E. E., Kochanek, C. S., McLeod, B. A., Muñoz, J. A., Impey, C. D., Rix, H.-W., Keeton, C. R. & Peng, C. Y. (2000), 'Hubble Space Telescope Observations of 10 Two-Image Gravitational Lenses', ApJ **536**, 584–605.

Lemze, D., Barkana, R., Broadhurst, T. J. & Rephaeli, Y. (2007), 'Mass and Gas Profiles in A1689: Joint X-ray and Lensing Analysis'.

Lemze, D., Broadhurst, T., Rephaeli, Y., Barkana, R. & Umetsu, K. (2008), 'Dynamical Study of A1689 from Wide-Field VLT/VIMOS Spectroscopy: Mass Profile, Concentration Parameter, and Velocity Anisotropy'.

Lidman, C., Courbin, F., Kneib, J.-P., Golse, G., Castander, F. & Soucail, G. (2000), 'Exploring the gravitationally lensed system HE 1104-1805: VLT spectroscopy of the lens at z=0.729', A&A **364**, L62–L65.

Lidman, C., Courbin, F., Meylan, G., Broadhurst, T., Frye, B. & Welch, W. J. W. (1999), 'The Redshift of the Gravitationally Lensed Radio Source PKS 1830-211', ApJ **514**, L57–L60.

Lieu, R. (2008), 'Strong-Lensing Time Delay: A New Way of Measuring Cosmic Shear', ApJ **674**, 75–79.

Limousin, M., Richard, J., Jullo, E., Kneib, J.-P., Fort, B., Soucail, G., Elíasdóttir, Á., Natarajan, P., Ellis, R. S., Smail, I., Czoske, O., Smith, G. P., Hudelot, P., Bardeau, S., Ebeling, H., Egami, E. & Knudsen, K. K. (2007), 'Combining Strong and Weak Gravitational Lensing in Abell 1689', ApJ **668**, 643–666.

Linder, E. V. (2004), 'Strong gravitational lensing and dark energy complementarity', Phys. Rev. D **70**(4), 043534–+.

Loeb, A. & Mao, S. (1994), 'Evidence from gravitational lensing for a nonthermal pressure support in the cluster of galaxies Abell 2218', ApJ **435**, L109–L112.

Łokas, E. L., Prada, F., Wojtak, R., Moles, M. & Gottlöber, S. (2006), 'The complex velocity distribution of galaxies in Abell 1689: implications for mass modelling', MNRAS **366**, L26–L30.

Lopez, S., Wucknitz, O. & Wisotzki, L. (1998), 'Detection of the lensing galaxy in HE 2149-2745', A&A **339**, L13–L16.

Lovell, J. E. J., Jauncey, D. L., Reynolds, J. E., Wieringa, M. H., King, E. A., Tzioumis, A. K., McCulloch, P. M. & Edwards, P. G. (1998), 'The Time Delay in the Gravitational Lens PKS 1830-211', ApJ **508**, L51–L54.

Lubin, L. M., Fassnacht, C. D., Readhead, A. C. S., Blandford, R. D. & Kundić, T. (2000), 'A Keck Survey of Gravitational Lens Systems. I. Spectroscopy of SBS 0909+532, HST 1411+5211, and CLASS B2319+051', AJ **119**, 451–459.

Macciò, A. V. & Miranda, M. (2006), 'The effect of low-mass substructures on the cusp lensing relation', MNRAS **368**, 599–608.

Macciò, A. V., Moore, B., Stadel, J. & Diemand, J. (2006), 'Radial distribution and strong lensing statistics of satellite galaxies and substructure using high-resolution ΛCDM hydrodynamical simulations', MNRAS **366**, 1529–1538.

Magain, P. (2005), Time Delay in Gravitational Lenses: an Alternative Route to the Hubble Constant, *in* C. Sterken, ed., 'The Light-Time Effect in Astrophysics: Causes and cures of the O-C diagram', Vol. 335 of *Astronomical Society of the Pacific Conference Series*, pp. 207–+.

Magain, P., Courbin, F. & Sohy, S. (1998), 'Deconvolution with Correct Sampling', ApJ **494**, 472–+.

Mahdavi, A., Hoekstra, H., Babul, A. & Henry, J. P. (2007), 'Evidence for Non-Hydrostatic Gas from the Cluster X-ray to Lensing Mass Ratio', *preprint, arXiv:0710.4132 [astro-ph]* .

Maoz, D. & Rix, H.-W. (1993), 'Early-Type Galaxies, Dark Halos, and Gravitational Lensing Statistics', ApJ **416**, 425–+.

Markevitch, M., Bautz, M. W., Biller, B., Butt, Y., Edgar, R., Gaetz, T., Garmire, G., Grant, C. E., Green, P., Juda, M., Plucinsky, P. P., Schwartz, D., Smith, R., Vikhlinin, A., Virani, S., Wargelin, B. J. & Wolk, S. (2003), 'Chandra Spectra of the Soft X-Ray Diffuse Background', ApJ **583**, 70–84.

Marshall, P., Blandford, R. & Sako, M. (2005), 'The SNAP strong lens survey [review article]', *New Astronomy Review* **49**, 387–391.

Mazzotta, P., Rasia, E., Moscardini, L. & Tormen, G. (2004), 'Comparing the temperatures of galaxy clusters from hydrodynamical N-body simulations to Chandra and XMM-Newton observations', MNRAS **354**, 10–24.

Metcalf, R. B. (2005), 'The Importance of Intergalactic Structure to Gravitationally Lensed Quasars', ApJ **629**, 673–679.

Mewe, R., Gronenschild, E. H. B. M. & van den Oord, G. H. J. (1985), 'Calculated X-radiation from optically thin plasmas. V', A&AS **62**, 197–254.

Meylan, G., Courbin, F., Lidman, C., Kneib, J.-P. & Tacconi-Garman, L. E. (2005), 'Confirmation of two extended objects along the line of sight to PKS 1830-211 with ESO-VLT adaptive optics imaging', A&A **438**, L37–L40.

Meylan, G., Jetzer, P., North, P., Schneider, P., Kochanek, C. S. & Wambsganss, J., eds (2006), *Gravitational Lensing: Strong, Weak and Micro*.

Miralda-Escude, J. & Babul, A. (1995), 'Gravitational Lensing in Clusters of Galaxies: New Clues Regarding the Dynamics of Intracluster Gas', ApJ **449**, 18–+.

Morgan, C. W., Kochanek, C. S., Dai, X., Morgan, N. D. & Falco, E. E. (2008), 'X-Ray and Optical Microlensing in the Lensed Quasar PG 1115+080', ApJ **689**, 755–761.

Morgan, N. D., Caldwell, J. A. R., Schechter, P. L., Dressler, A., Egami, E. & Rix, H.-W. (2004), 'WFI J2026-4536 and WFI J2033-4723: Two New Quadruple Gravitational Lenses', AJ **127**, 2617–2630.

Morgan, N. D., Kochanek, C. S., Pevunova, O. & Schechter, P. L. (2005), 'The Lens Redshift and Galaxy Environment for HE 0435-1223', AJ **129**, 2531–2541.

Morgan, N. D., Snyder, J. A. & Reens, L. H. (2003), 'SDSS J1650+4251: A New Gravitational Lens', AJ **126**, 2145–2151.

Motta, V., Mediavilla, E., Muñoz, J. A., Falco, E., Kochanek, C. S., Arribas, S., García-Lorenzo, B., Oscoz, A. & Serra-Ricart, M. (2002), 'Detection of the 2175 Å Extinction Feature at z = 0.83', ApJ **574**, 719–725.

Moustakas, L. A., Bolton, A. J., Booth, J. T., Bullock, J. S., Cheng, E., Coe, D., Fassnacht, C. D., Gorjian, V., Heneghan, C., Keeton, C. R., Kochanek, C. S., Lawrence, C. R., Marshall, P. J., Metcalf, R. B., Natarajan, P., Nikzad, S., Peterson, B. M. & Wambsganss, J. (2008), The Observatory for Multi-Epoch Gravitational Lens Astrophysics (OMEGA), *in* 'Society of Photo-Optical Instrumentation Engineers (SPIE) Conference Series', Vol. 7010 of *Presented at the Society of Photo-Optical Instrumentation Engineers (SPIE) Conference*.

Myers, S. T., Fassnacht, C. D., Djorgovski, S. G., Blandford, R. D., Matthews, K., Neugebauer, G., Pearson, T. J., Readhead, A. C. S., Smith, J. D., Thompson, D. J., Womble, D. S., Browne, I. W. A., Wilkinson, P. N., Nair, S., Jackson, N., Snellen, I. A. G., Miley, G. K., de Bruyn, A. G. & Schilizzi, R. T. (1995), '1608+656: A Quadruple-Lens System Found in the CLASS Gravitational Lens Survey', ApJ **447**, L5+.

Navarro, J. F., Frenk, C. S. & White, S. D. M. (1996), 'The Structure of Cold Dark Matter Halos', ApJ **462**, 563–+.

Neto, A. F., Gao, L., Bett, P., Cole, S., Navarro, J. F., Frenk, C. S., White, S. D. M., Springel, V. & Jenkins, A. (2007), 'The statistics of Λ CDM halo concentrations', MNRAS **381**, 1450–1462.

Oguri, M. (2007), 'Gravitational Lens Time Delays: A Statistical Assessment of Lens Model Dependences and Implications for the Global Hubble Constant', ApJ **660**, 1–15.

Oguri, M., Inada, N., Castander, F. J., Gregg, M. D., Becker, R. H., Ichikawa, S.-I., Pindor, B., Brinkmann, J., Eisenstein, D. J., Frieman, J. A., Hall, P. B., Johnston, D. E., Richards, G. T., Schechter, P. L., Schneider, D. P. & Szalay, A. S. (2004), 'SDSS J1335+0118: A New Two-Image Gravitational Lens', PASJ **56**, 399–405.

Oguri, M., Inada, N., Hennawi, J. F., Richards, G. T., Johnston, D. E., Frieman, J. A., Pindor, B., Strauss, M. A., Brunner, R. J., Becker, R. H., Castander, F. J., Gregg, M. D., Hall, P. B., Rix, H.-W., Schneider, D. P., Bahcall, N. A., Brinkmann, J. & York, D. G. (2005), 'Discovery of Two Gravitationally Lensed Quasars with Image Separations of 3" from the Sloan Digital Sky Survey', ApJ **622**, 106–115.

Okura, Y., Umetsu, K. & Futamase, T. (2008), 'A Method for Weak-Lensing Flexion Analysis by the HOLICs Moment Approach', ApJ **680**, 1–16.

Olesen, P. & Ambjørn, J. (2003), *Lecture Notes: General Relativity, Cosmology and Classical Gauge Theories*, University of Copenhagen, The Niels Bohr Institute.

Oscoz, A., Alcalde, D., Serra-Ricart, M., Mediavilla, E., Abajas, C., Barrena, R., Licandro, J., Motta, V. & Muñoz, J. A. (2001), 'Time Delay in QSO 0957+561 From 1984-1999 Optical Data', ApJ **552**, 81–90.

Oscoz, A., Mediavilla, E., Goicoechea, L. J., Serra-Ricart, M. & Buitrago, J. (1997), 'Time Delay of QSO 0957+561 and Cosmological Implications', ApJ **479**, L89+.

Paczynski, B. (1986), 'Gravitational microlensing at large optical depth', ApJ **301**, 503–516.

Paraficz, D. & Hjorth, J. (2009*a*), 'Gravitational lenses as cosmic rulers: $\Omega_{\rm m}$, Ω_Λ from time delays and velocity dispersions', A&A .

Paraficz, D. & Hjorth, J. (2009*b*), 'The Hubble Constant inferred from 18 time delay lenses', ApJ .

Paraficz, D., Hjorth, J., Burud, I., Jakobsson, P. & Elíasdóttir, Á. (2006), 'Microlensing variability in time-delay quasars', A&A **455**, L1–L4.

Paraficz, D., Hjorth, J. & Elíasdóttir, Á. (2009), 'Results of optical monitoring of 5 SDSS double QSOs with the Nordic Optical Telescope', A&A **499**, 395–408.

Patnaik, A. R. & Narasimha, D. (2001), 'Determination of time delay from the gravitational lens B1422+231', MNRAS **326**, 1403–1411.

Peacock, J. A., Cole, S., Norberg, P., Baugh, C. M., Bland-Hawthorn, J., Bridges, T., Cannon, R. D., Colless, M., Collins, C., Couch, W., Dalton, G., Deeley, K., De Propris, R., Driver, S. P., Efstathiou, G., Ellis, R. S., Frenk, C. S., Glazebrook, K., Jackson, C., Lahav, O., Lewis, I., Lumsden, S., Maddox, S., Percival, W. J., Peterson, B. A., Price, I., Sutherland, W. & Taylor, K. (2001), 'A measurement of the cosmological mass density from clustering in the 2dF Galaxy Redshift Survey', Nature **410**, 169–173.

Peng, C. Y., Impey, C. D., Rix, H.-W., Kochanek, C. S., Keeton, C. R., Falco, E. E., Lehár, J. & McLeod, B. A. (2006), 'Probing the Coevolution of Supermassive Black Holes and Galaxies Using Gravitationally Lensed Quasar Hosts', ApJ **649**, 616–634.

Perlmutter, S., Aldering, G., Goldhaber, G., Knop, R. A., Nugent, P., Castro, P. G., Deustua, S., Fabbro, S., Goobar, A., Groom, D. E., Hook, I. M., Kim, A. G., Kim, M. Y., Lee, J. C., Nunes, N. J., Pain, R., Pennypacker, C. R., Quimby, R., Lidman, C., Ellis, R. S., Irwin, M., McMahon, R. G., Ruiz-Lapuente, P., Walton, N., Schaefer, B., Boyle, B. J., Filippenko, A. V., Matheson, T., Fruchter, A. S., Panagia, N., Newberg, H. J. M., Couch, W. J. & The Supernova Cosmology Project (1999), 'Measurements of Omega and Lambda from 42 High-Redshift Supernovae', ApJ **517**, 565–586.

Poindexter, S., Morgan, N., Kochanek, C. S. & Falco, E. E. (2007), 'Mid-IR Observations and a Revised Time Delay for the Gravitational Lens System Quasar HE 1104-1805', ApJ **660**, 146–151.

Raychaudhury, S., Saha, P. & Williams, L. L. R. (2003), 'Is B1422+231 a "Golden Lens"?', AJ **126**, 29–36.

Refsdal, S. (1964), 'On the possibility of determining Hubble's parameter and the masses of galaxies from the gravitational lens effect', MNRAS **128**, 307–+.

Riess, A. G., Filippenko, A. V., Challis, P., Clocchiatti, A., Diercks, A., Garnavich, P. M., Gilliland, R. L., Hogan, C. J., Jha, S., Kirshner, R. P., Leibundgut, B., Phillips, M. M., Reiss, D., Schmidt, B. P., Schommer, R. A., Smith, R. C., Spyromilio, J., Stubbs, C., Suntzeff, N. B. & Tonry, J. (1998), 'Observational Evidence from Supernovae for an Accelerating Universe and a Cosmological Constant', AJ **116**, 1009–1038.

Riess, A. G., Macri, L., Casertano, S., Sosey, M., Lampeitl, H., Ferguson, H. C., Filippenko, A. V., Jha, S. W., Li, W., Chornock, R. & Sarkar, D. (2009), 'A Redetermination of the Hubble Constant with the Hubble Space Telescope from a Differential Distance Ladder', ApJ **699**, 539–563.

Romanowsky, A. J. & Kochanek, C. S. (1999), 'Constraints on H_0 from the Central Velocity Dispersions of Lens Galaxies', ApJ **516**, 18–26.

Rusin, D., Kochanek, C. S. & Keeton, C. R. (2003), 'Self-similar Models for the Mass Profiles of Early-Type Lens Galaxies', ApJ **595**, 29–42.

Saha, P. (2000), 'Lensing Degeneracies Revisited', AJ **120**, 1654–1659.

Saha, P., Coles, J., Macciò, A. V. & Williams, L. L. R. (2006), 'The Hubble Time Inferred from 10 Time Delay Lenses', ApJ **650**, L17–L20.

Saha, P. & Williams, L. L. R. (1997), 'Non-parametric reconstruction of the galaxy lens in PG 1115+080', MNRAS **292**, 148–+.

Saha, P. & Williams, L. L. R. (2004), 'A Portable Modeler of Lensed Quasars', AJ **127**, 2604–2616.

Saha, P. & Williams, L. L. R. (2006), 'Gravitational Lensing Model Degeneracies: Is Steepness All-Important?', ApJ **653**, 936–941.

Saha, P. & Williams, T. B. (1994), 'Unfolding kinematics from galaxy spectra: A Bayesian method', AJ **107**, 1295–1302.

Sandage, A., Tammann, G. A., Saha, A., Reindl, B., Macchetto, F. D. & Panagia, N. (2006), 'The Hubble Constant: A Summary of the Hubble Space Telescope Program for the Luminosity Calibration of Type Ia Supernovae by Means of Cepheids', ApJ **653**, 843–860.

Sarazin, C. L. (1988), *X-ray Emission from Clusters of Galaxies*, Cambridge University Press.

Schechter, P. L. (2005), The Hubble Constant from Gravitational Lens Time Delays, *in* Y. Mellier & G. Meylan, ed., 'Gravitational Lensing Impact on Cosmology', Vol. 225 of *IAU Symposium*, pp. 281–296.

Schechter, P. L. & Wambsganss, J. (2004), The dark matter content of lensing galaxies at 1.5 R_e, *in* S. Ryder, D. Pisano, M. Walker & K. Freeman, eds, 'Dark Matter in Galaxies', Vol. 220 of *IAU Symposium*, pp. 103–+.

Schild, R. (1996), Rapid Microlensing in Q0957+561, *in* 'Bulletin of the American Astronomical Society', Vol. 28 of *Bulletin of the American Astronomical Society*, pp. 1307–+.

Schneider, P. (2003), 'Gravitational lensing as a probe of structure', *ArXiv Astrophysics e-prints* .

Schwab, J., Bolton, A. S. & Rappaport, S. A. (2009), 'Galaxy-Scale Strong Lensing Tests of Gravity and Geometric Cosmology: Constraints and Systematic Limitations', *ArXiv e-prints* .

Sharon, K., Ofek, E. O., Smith, G. P., Broadhurst, T., Maoz, D., Kochanek, C. S., Oguri, M., Suto, Y., Inada, N. & Falco, E. E. (2005), 'Discovery of Multiply Imaged Galaxies behind the Cluster and Lensed Quasar SDSS J1004+4112', ApJ **629**, L73–L76.

Spergel, D. N., Bean, R., Doré, O., Nolta, M. R., Bennett, C. L., Dunkley, J., Hinshaw, G., Jarosik, N., Komatsu, E., Page, L., Peiris, H. V., Verde, L., Halpern, M., Hill, R. S., Kogut, A., Limon, M., Meyer, S. S., Odegard, N., Tucker, G. S., Weiland, J. L., Wollack, E. & Wright, E. L. (2007), 'Three-Year Wilkinson Microwave Anisotropy Probe (WMAP) Observations: Implications for Cosmology', ApJS **170**, 377–408.

Spergel, D. N., Verde, L., Peiris, H. V., Komatsu, E., Nolta, M. R., Bennett, C. L., Halpern, M., Hinshaw, G., Jarosik, N., Kogut, A., Limon, M., Meyer, S. S., Page, L., Tucker, G. S., Weiland, J. L., Wollack, E. & Wright, E. L. (2003), 'First-Year Wilkinson Microwave Anisotropy Probe (WMAP) Observations: Determination of Cosmological Parameters', ApJS **148**, 175–194.

Suyu, S. H., Marshall, P. J., Auger, M. W., Hilbert, S., Blandford, R. D., Koopmans, L. V. E., Fassnacht, C. D. & Treu, T. (2009), 'Dissecting the Gravitational Lens B1608+656. II. Precision Measurements of the Hubble Constant, Spatial Curvature, and the Dark Energy Equation of State', *ArXiv e-prints* .

Teague, P. F., Carter, D. & Gray, P. M. (1990), 'The dynamics and structure of rich clusters of galaxies. I - Velocity data', ApJS **72**, 715–753.

Tonry, J. L. (1983), 'Anisotropic velocity dispersions in spherical galaxies', ApJ **266**, 58–68.

Tonry, J. L. (1998), 'Redshifts of the gravitational lenses B1422+231 and PG 1115+080', AJ **115**, 1–+.

Toomre, A. (1977), Mergers and Some Consequences, *in* B. M. Tinsley & R. B. Larson, ed., 'Evolution of Galaxies and Stellar Populations', pp. 401–+.

Treu, T. & Koopmans, L. V. E. (2004), 'Massive Dark Matter Halos and Evolution of Early-Type Galaxies to z ˜ 1', ApJ **611**, 739–760.

Trotter, C. S., Winn, J. N. & Hewitt, J. N. (2000), 'A Multipole-Taylor Expansion for the Potential of the Gravitational Lens MG J0414+0534', ApJ **535**, 671–691.

Tu, H. et al. (2007), 'Probing the Slope of Cluster Mass Profile with Gravitational Rings: Application to Abell 1689', *preprint, arXiv:0710.2246 [astro-ph]* .

Ullán, A., Goicoechea, L. J., Gil-Merino, R., Serra-Ricart, M., Muñoz, J. A., Mediavilla, E., González-Cadelo, J. & Oscoz, A. (2005), The Possible Origins of the VR Magnification Ratios of Q0957+561AB, *in* Y. Mellier & G. Meylan, eds, 'Gravitational Lensing Impact on Cosmology', Vol. 225 of *IAU Symposium*, pp. 305–310.

Umetsu, K. & Broadhurst, T. (2007), 'Combining Lens Distortion and Depletion to Map the Mass Distribution of A1689', *preprint, arXiv:0712.3441 [astro-ph]* .

van de Ven, G., van Dokkum, P. G. & Franx, M. (2003), 'The Fundamental Plane and the evolution of the M/L ratio of early-type field galaxies up to z˜ 1', MNRAS **344**, 924–934.

Voigt, L. M. & Fabian, A. C. (2006), 'Galaxy cluster mass profiles', MNRAS **368**, 518–533.

Vuissoz, C., Courbin, F., Sluse, D., Meylan, G., Chantry, V., Eulaers, E., Morgan, C., Eyler, M. E., Kochanek, C. S., Coles, J., Saha, P., Magain, P. & Falco, E. E. (2008), 'COSMOGRAIL: the COSmological MOnitoring of GRAvItational Lenses. VII. Time delays and the Hubble constant from WFI J2033-4723', A&A **488**, 481–490.

Vuissoz, C., Courbin, F., Sluse, D., Meylan, G., Ibrahimov, M., Asfandiyarov, I., Stoops, E., Eigenbrod, A., Le Guillou, L., van Winckel, H. & Magain, P. (2007), 'COSMOGRAIL: the COSmological MOnitoring of GRAvItational Lenses. V. The time delay in SDSS J1650+4251', A&A **464**, 845–851.

Walsh, D., Carswell, R. F. & Weymann, R. J. (1979), '0957 + 561 A, B - Twin quasistellar objects or gravitational lens', Nature **279**, 381–384.

Wambsganss, J. (1998), 'Gravitational Lensing in Astronomy', *Living Reviews in Relativity* **1**, 12–+.

Wambsganss, J., Bode, P. & Ostriker, J. P. (2004), 'Giant Arc Statistics in Concord with a Concordance Lambda Cold Dark Matter Universe', ApJ **606**, L93–L96.

Webb, W. & Malkan, M. (2000), 'Rapid Optical Variability in Active Galactic Nuclei and Quasars', ApJ **540**, 652–677.

Weinberg, N. N. & Kamionkowski, M. (2003), 'Constraining dark energy from the abundance of weak gravitational lenses', MNRAS **341**, 251–262.

Weymann, R. J., Latham, D., Roger, J., Angel, P., Green, R. F., Liebert, J. W., Turnshek, D. A., Turnshek, D. E. & Tyson, J. A. (1980), 'The triple QSO PG1115+08 - Another probable gravitational lens', Nature **285**, 641–643.

White, R. L., Becker, R. H., Gregg, M. D., Laurent-Muehleisen, S. A., Brotherton, M. S., Impey, C. D., Petry, C. E., Foltz, C. B., Chaffee, F. H., Richards, G. T., Oegerle, W. R., Helfand, D. J., McMahon, R. G. & Cabanela, J. E. (2000), 'The FIRST Bright Quasar Survey. II. 60 Nights and 1200 Spectra Later', ApJS **126**, 133–207.

White, S. D. M., Navarro, J. F., Evrard, A. E. & Frenk, C. S. (1993), 'The baryon content of galaxy clusters: a challenge to cosmological orthodoxy', Nature **366**, 429–433.

Williams, L. L. R. & Saha, P. (2000), 'Pixelated Lenses and H_0 from Time-Delay Quasars', AJ **119**, 439–450.

Williams, L. L. R. & Saha, P. (2004), 'Models of the Giant Quadruple Quasar SDSS J1004+4112', AJ **128**, 2631–2641.

Winn, J. N., Kochanek, C. S., McLeod, B. A., Falco, E. E., Impey, C. D. & Rix, H.-W. (2002), 'PKS 1830-211: A Face-on Spiral Galaxy Lens', ApJ **575**, 103–110.

Wisotzki, L., Koehler, T., Kayser, R. & Reimers, D. (1993), 'The new double QSO HE 1104-1805: Gravitational lens with microlensing or binary quasar?', A&A **278**, L15–L18.

Wisotzki, L., Koehler, T., Lopez, S. & Reimers, D. (1996), 'Discovery of a new gravitationally lensed QSO with broad absorption lines.', A&A **315**, L405+.

Wold, M., Brotherton, M. S. & Shang, Z. (2007), 'The dependence of quasar variability on black hole mass', MNRAS **375**, 989–999.

Wucknitz, O. (2002), 'Degeneracies and scaling relations in general power-law models for gravitational lenses', MNRAS **332**, 951–961.

Wucknitz, O., Biggs, A. D. & Browne, I. W. A. (2004), 'Models for the lens and source of B0218+357: a LENSCLEAN approach to determine H_0', MNRAS **349**, 14–30.

Wucknitz, O. & Refsdal, S. (2001), Degeneracies of the Radial Mass Profile in Lens Models, *in* T. G. Brainerd & C. S. Kochanek, eds, 'Gravitational Lensing: Recent Progress and Future Go', Vol. 237 of *Astronomical Society of the Pacific Conference Series*, pp. 157–+.

Xu, D. D., Mao, S., Wang, J., Springel, V., Gao, L., White, S. D. M., Frenk, C. S., Jenkins, A., Li, G. & Navarro, J. F. (2009), 'Effects of dark matter substructures on gravitational lensing: results from the Aquarius simulations', MNRAS **398**, 1235–1253.

Xue, S.-J. & Wu, X.-P. (2002), 'Chandra X-Ray Observatory Observation of A1689: New Determination of Mass Distribution and Comparison to Lensing Measurements', ApJ **576**, 152–158.

Zhang, Y. Y. et al. (2008), 'LoCuSS: Comparison of Observed X-ray and Lensing Galaxy Cluster Scaling Relations with Simulations', *preprint, arXiv:0802.0770 [astro-ph]* .

Zwicky, F. (1937), 'On the Masses of Nebulae and of Clusters of Nebulae', ApJ **86**, 217–+.

LIST OF FIGURES

1.1 Light deflection diagram . . . 13
1.2 The positions of stars examined in the historic test of Einstein's theory of gravity . . . 15

2.1 Schematic view of a lensed quasar . . . 20
2.2 Schematic view of a lensed quasar magnification . . . 22
2.3 Constraints on Ω_M, Ω_Λ from other major cosmological surveys . . . 27
2.4 MCMC simulations showing constraints on Ω_M, Ω_Λ set by time delays of multiply lensed quasars . . . 29
2.5 MCMC simulations showing how combination of time delay and velocity dispersion constrain Ω_M, Ω_Λ and H_0 . . . 30
2.6 Snapshots of the evolution of the cluster and bright central galaxy . . . 34
2.7 The density slopes of 58 SLACS early-type galaxies . . . 35

3.1 Lens model of SDSS J1001+5027 . . . 40
3.2 Mass sheet degeneracy . . . 42
3.3 Lens galaxies in clusters . . . 43
3.4 Pixelated mass models of 3 complicated lensing systems . . . 45
3.5 The modeling results of the three lensed quasars . . . 46

4.1 Deconvolution process . . . 53

5.1 Finding chart of the system SDSS J0903+5028 . . . 60
5.2 Finding chart of the system SDSS J1001+5027 . . . 61
5.3 Finding chart of the system SDSS J1206+4332 . . . 62
5.4 Finding chart of the system: SDSS J1335+0118 a . . . 65
5.5 Finding chart of the two system SDSS J1353+1138 . . . 66
5.6 Results of the deconvolution of the 5 systems . . . 68
5.7 R-band light curves of SDSS J0903+5028 . . . 70
5.8 R-band light curves of SDSS J1335+0118 . . . 71
5.9 R-band light curves of SDSS J1353+1138 . . . 72
5.10 R-band light curves of SDSS J1001+5027 . . . 74
5.11 R-band light curves of SDSS J1206+4332 . . . 75
5.12 R-band light curves of SDSS J1206+4332 with the A light curve is shifted in time by 116 days 77
5.13 Time delay of SDSS J1206+4332 . . . 78
5.14 Microlensing of the SDSS J1206+4332 . . . 80
5.15 Microlensing of the SDSS J1001+5027 . . . 81
5.16 Microlensing of the SDSS J1335+0118 . . . 82
5.17 Microlensing of the SDSS J1353+1138 . . . 83
5.18 Microlensing of the SDSS J0903+5028 . . . 84
5.19 Lens model of SDSS J0903+5028 . . . 86
5.20 Lens model of SDSS J1001+5027 . . . 88

5.21 Lens model of SDSS J1206+4332 90
5.22 Mass model of SDSS J1335+0118 91
5.23 Mass model of SDSS J1353+1138 92
5.24 The modeling results of the five lensed quasars 94
5.25 The result of the simultaneous modeling 96

6.1 Ensemble of 18 average mass maps of the lenses 104
6.2 Histograms of the ensembles of H_0 values estimated from 18 lensing systems for flat and closed Universe 108
6.3 Histograms of the 10, 16 and 18 ensembles of H_0 value 109
6.4 The distribution of H_0 values for the selected sample of 5 elliptical galaxies having constrained steepness of mass profiles 111

7.1 Dependence of the three quantities, $\Delta\tau$, σ^2 and $\Delta\tau/\sigma^2$ on the lens redshift 117
7.2 MCMC simulations showing the constraints on $\Omega_{\rm m}, \Omega_\Lambda$ from $\Delta\tau$, σ^2 and $\Delta\tau/\sigma^2$ 119
7.3 MCMC simulations for $\Delta\tau/\sigma^2$ 121

A.1 Exposure corrected X-ray image of Abell1689 133
A.2 The ratio between the surface brightness profiles of the NE and SW halves of Abell1689 . . 134
A.3 The obtained hardness ratio maps of Abell1689 136
A.4 The temperature profile reconstructed from the SW symmetric part of Abell 1689 138
A.5 The 3D X-ray mass profile of Abell1689 140
A.6 Comparison of the temperature profile of Abell1689 143
A.7 Optical images (HST/ACS) with gravitational lensing contours of Abell1689 145
A.8 The hardness ratio maps of Abell1689 147
A.9 The 2D projected mass profile of Abell 1689, reconstructed from X-ray, strong gravitational lensing and weak gravitational lensing 149
A.10 Comparison of the weak and strong gravitational mass profiles of Abell1689 151

LIST OF TABLES

3.1 Lens model of SDSS J1001+5027 39

4.1 Targets properties 49

5.1 Astrometric properties and redshifts of the observed systems 63
5.2 Lens model of SDSS J0903+5028 87
5.3 Lens model of SDSS J1001+5027 87
5.4 Lens model of SDSS J1206+4332 89
5.5 Lens model of SDSS J1335+0118 89
5.6 Lens model of SDSS J1353+1138 93
5.7 Modeled time delays of the five lensed quasars 95

6.1 H_0 comparison 101
6.2 Properties of time-delay lenses 106

A.1 The analysed *Chandra* observations of Abell 1689 132

ACRONYMS

ALFOSC	Andalucia Faint Object Spectrograph and Camera
ALMA	The Atacama Large Millimeter/Submillimeter Array
AOD	Apparent Optical Depth
CLASS	The Cosmic Lens All-Sky Survey
CMB	Cosmic Microwave Background
COSMOGRAIL	the COSmological MOnitoring of GRAvItational Lenses
DSS	Digital Sky Survey
E-ELT	European Extremely Large Telescope
EFEs	Einstein's Field Equations
FOV	Field of View
FP	Fundamental Plane
GAIA	Graphical Astronomy and Image Analysis (reduction and analysis software)
GL	Gravitational Lensing
GR	General Relativity
HIRES	High-resolution Echelle Spectrograph (at Keck)
HST	Hubble Space Telescope
IDL	Interactive Data Language (programming language)
IRAF	Image Reduction and Analysis Facility (reduction and analysis software)
JDEM	Joint Dark Energy Mission
LSS	Large Scale Structures
LSST	Large Synoptic Survey Telescope
JWST	James Webb Space Telescope
ΛCDM	Λ-Cold Dark Matter
MIDAS	Munich Image Data Analysis System (reduction and analysis software)
NOT	Nordic Optical Telescope
OPC	Observing Programmes Committee
Pan-Starrs	Panoramic Survey Telescope & Rapid Response System
PI	Principal Investigator
PSF	Point Spread Function
QSO	Quasi-stellar Object
SED	Spectral Energy Distribution
SFR	Star formation rate
SKA	Square Kilometre Array
SLACS	The Sloan Lens ACS Survey
SN	Supernova
StanCam	the Stand-by CCD Camera
TMT	Thirty Meter Telescope
ToO	Target-of-Opportunity (proposal type/fast observation mode)
VLT	Very Large Telescope (Paranal/Chile)